

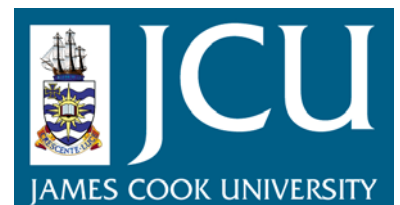
# JCU ePrints

This file is part of the following reference:

**McLellan, John George (2004) *Numerical modelling of deformation and fluid flow in hydrothermal systems.* PhD thesis, James Cook University.**

Access to this file is available from:

<http://eprints.jcu.edu.au/2131>



# **Section A**

## **Body Text and Figures**

# Chapter 1

## General Introduction

## 1.1 General Introduction

This study is primarily concerned with understanding the effects of deformation on fluid flow within hydrothermal systems, and its consequent role in ore genesis. Different types of numerical modelling are applied to several scenarios in an attempt to examine both conceptual and realistic problems. Continuous modelling techniques are applied to explore the geomechanical aspects of proposed genetic models of ore deposits, such as the large microplaty hematite deposits in the Hamersley Province in Western Australia, and the Pb-Zn-Ag Century deposit of Northwest Queensland. This modelling technique is also applied to more generic problems such as the effects of extension, permeability and topography on fluid flow. Discontinuous or discrete modelling techniques are applied to examine deformation and stress distribution around faults and intrusions in the Cloncurry-Selwyn Region, as a predictive tool for future exploration.

This author's involvement in this project commenced in 2001 and was sponsored by an Australian Post Graduate Award, a pmd\*<sup>2</sup>CRC top-up scholarship and project support from an ARC Large Grant to Oliver & Dickens. As a student researcher of the pmd\*<sup>2</sup>CRC, the authors involvement consisted of the following groups;

- M2** Earth Process Software Development
- F1** Fluid chemical paths in ore forming processes
- F2** Conceptual multiphase reactive transport models
- I2/I3** Total Systems Analysis of the Eastern Succession

Soon after commencement of this project the author became a Student Researcher as part of the Predictive Mineral Discovery Co-operative Research Centre (pmd\**CRC*) and was supported by a pmd\**CRC* top up scholarship. The main pmd\**CRC* projects supporting this research were:

## **1.2 Numerical Modelling Applications**

Due to the complexity of each identified problem within this study, no single software application can be applied to address all of the identified conceptual models. Therefore, two main modelling packages were utilised to enable a tailored problem-solving approach to each scenario. The finite difference software package FLAC v.4.0 (Fast Lagrangian Analysis of Continua – Itasca Consulting Group Inc.) is used to model the effects of deformation on fluid flow, and is applied to the Hamersley Region and the Century deposit. UDEC v.3.10 (Universal Distinct Element Code - Itasca Consulting Group Inc.) is used to examine the distribution of stress and fluid flow in the Cloncurry Region.

## **1.3 Aims and Objectives**

The main objectives of this study were:

- a) To simulate the effects of deformation on fluid flow using numerical modelling techniques for several examples of hydrothermal systems.*
- b) To explore the sensitivity of varying the physical properties and input parameters as an ongoing process throughout the modelling procedure.*
- c) To relate the modelling outcomes to current genetic models and what influence these outcomes may have on ore genesis where applicable.*

- d) *To utilise numerical modelling as a predictive tool as part of the overall pmd\*CRC strategies and objectives.*

## **1.4 Thesis Outline**

This thesis is presented in one volume, consisting of two sections (**A** and **B**). Section **A** contains the main body text and figures, and section **B** contains all appendices related to this study. Due to the nature of this thesis, and the most striking commonality between all chapters being ‘numerical modelling’, it is structured containing six (6) chapters as outlined below. Chapters **3** through **6** are delivered in manuscript style, and are intended as journal articles (Chapter **3** is currently published- McLellan *et al.*, 2004). As a consequence of this format, there is some repetition of information between chapters, mainly with respect to modelling theory and geological background (e.g. Chapters **4** and **5**). A single reference list is presented following the final chapter in section **A**, and all computer code is listed in appendices in section **B**. The complete thesis is also in digital format on the accompanying CD-ROM.

### **1.4.1 Section A**

#### **Chapter 1: Introduction**

Chapter **1** introduces the study and presents the thesis outline aims and objectives. It also introduces the author’s involvement in this project and gives a brief overview of software applications used.

**Chapter 2: Numerical modelling; a theoretical overview**

Chapter 2 introduces Numerical Modelling by examining the theoretical aspects and modelling processes for the study of coupled deformation and fluid flow. The general mechanical relationships are examined with an overview of elastic-plastic behaviour, discrete and porous media flow. A software background section is also presented in this chapter.

**Chapter 3: Fluid flow in extensional environments; numerical modelling with an application to Hamersley iron ores**

Chapter 3 introduces the conceptual models on the effects of topography and extension on fluid flow patterns, and further examines this in the context of the genesis of large microplaty hematite ore deposits of the Hamersley Province, Western Australia.

**Chapter 4: Testing geomechanical processes in the formation of the Century Pb-Zn-Ag deposit**

Chapter 4 presents two conceptual models to test the genetic models of the giant Mesoproterozoic Zn-Pb-Ag Century Zinc Deposit. It examines the effects of extensional deformation in semi-lithified sediments on fluid flow and compares this to contractional deformation in lithified sediments, and the effect of overpressurisation.

### **Chapter 5: Discrete element modelling of stress partitioning and fluid flow in the Eastern Succession of the Mount Isa Block**

Chapter 5 introduces new modelling software (UDEC) and applies this software to deformation and stress distribution around faults and intrusions in the Eastern Succession of the Mt. Isa Block. The concept of this section is to utilise the results as a predictive tool as a companion to prospectivity analysis by CRC researchers in this economically significant area.

### **Chapter 6: Numerical models of deformation and fluid flow across basement-cover interfaces during extension-related mineralisation**

Chapter 6 examines the geomechanical relationships to fluid flow during extensional deformation of mineralised sedimentary (basinal) sequences.

#### **1.4.2 Section B**

##### **Appendices:**

This section presents appendices containing data files for numerical models within the body text.

## **Chapter 2**

### **Numerical modelling; a theoretical outline**

## 2.1 Introduction

In the geosciences field our understanding and theories of earth processes have become increasingly more complex over the last decade. In an attempt to understand the relationships between deformation, fluid flow, temperature, pressure and chemistry in subsurface rock systems, we have begun to utilise computer technology and numerical modelling software to answer questions that are otherwise difficult to answer due to the difficulty of in-situ monitoring or tests which are readily used in other science disciplines. However, the 'stockpiling' of geological data does not necessarily enhance our understanding of the physical processes involved in such systems. Numerical simulations provide the geoscientist with a powerful tool in determining the response of the system to any given parameters e.g. deformation, fluid flow, or heat transfer, and provides quantitative results that can then be used in a predictive capacity. Identifying critical geological processes enables the geologist to test scenarios and gain a better understanding of physically sensitive parameters, allowing a better insight into the processes involved. Examples of critical geological processes covered in this study are 1) the effects of extensional deformation and topography, and its effect on fluid flow in porous media, 2) the partitioning of stress and the response of fault architecture to deformation and fluids, and 3) dilatancy, failure and permeability issues controlling fluid flow.

This chapter aims to introduce the theoretical components of the geological system and provide a mathematical description of the governing equations involved in the processes previously mentioned. Finally, a comprehensive background and description of software applicability is given followed by a

description of the relationships between the modelling procedures used here and geological problem solving.

## 2.2 Theoretical Background

This section introduces a comprehensive review of the mechanical concepts, and the relationship of these concepts to deformation in a geological sense. This is followed by the constitutive models that govern the solving equations of the numerical modelling procedure. The theory of rock/fluid interaction within deforming porous media will then be investigated. The last section will then examine the mechanical relationships of discrete-element modelling, and in particular the theory of fractures and associated fluid flow.

### 2.2.1 General Mechanical Relationships

The simplest form of mechanics that concerns us in geology is the concepts of stress and strain. Stress is a force per unit area which can be transmitted through a material. Stress perpendicular to a surface is known as *normal stress* ( $\sigma_n$ ), and stress that is parallel to a surface is known as *shear stress* ( $\sigma_s$ ) (Fig. 2.1a). In 2-dimensional stress space the normal stresses are considered as  $\sigma_{xx}$  and  $\sigma_{yy}$ , and shear stress as  $\sigma_{xy}$  and  $\sigma_{yx}$  (Fig. 2.1b). To prescribe a 2-dimensional state of stress three independent components  $\sigma_{xx}$ ,  $\sigma_{yy}$  and  $\sigma_{xy}$  must be specified. Stress applied to a solid results in deformation (strain), and in its simplest form may be seen as a decrease in the volume of the solid under an applied stress. As with stress, strain can be simplified to *normal strain* ( $\epsilon_n$ ), which is defined as the ratio of change in length of a solid to its original length ( $\Delta L/L_0$ ) (Fig. 2.1c), and *shear strain* ( $\epsilon_s$ ), which can be defined as ( $\tan \phi =$

$\Delta s/d_0$ (Fig. 2.1d). Again these can be described as  $\epsilon_{xx}$ ,  $\epsilon_{yy}$  and  $\epsilon_{xy}$  as in the example of stress shown above.

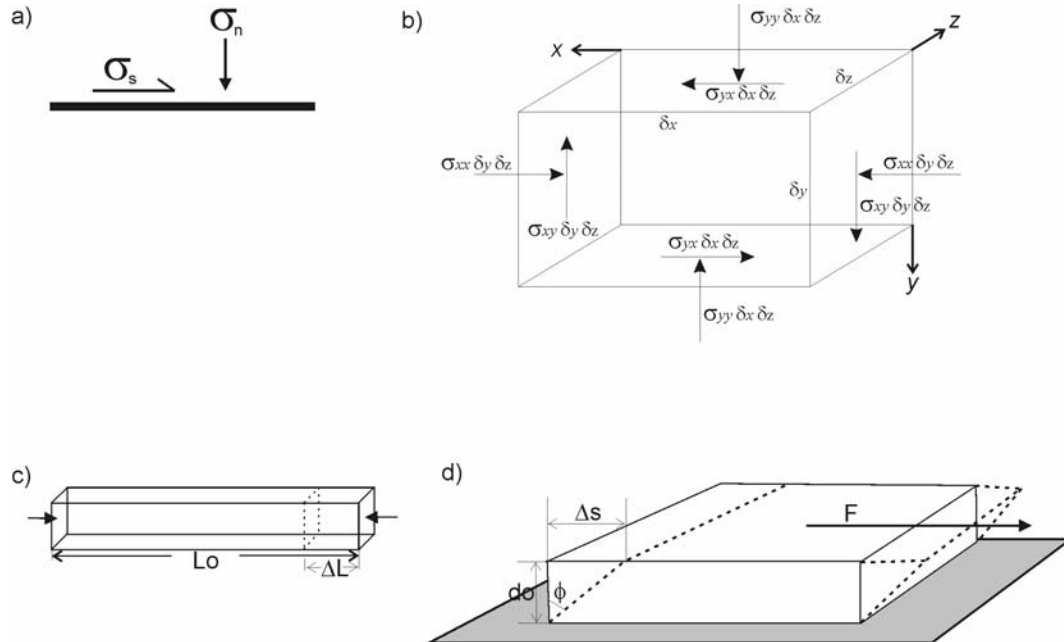


**Figure 2.1** Schematic diagrams showing a) simplified stress components acting on a plane as normal and shear stress; b) Block diagram depicting 2-dimensional stress space; c) simple block in uniaxial compression showing normal strain as the ratio of  $L_0/\Delta L$ ; d) material block undergoing shear on the top surface.

For 3-dimensional stress we require nine additional stress components, i.e.  $\sigma_{xx}$ ,  $\sigma_{yy}$ ,  $\sigma_{zz}$  (normal stresses), and  $\sigma_{xy}$ ,  $\sigma_{yx}$ ,  $\sigma_{xz}$ ,  $\sigma_{zx}$ ,  $\sigma_{yz}$  and  $\sigma_{zy}$  (shear stresses), to specify a state of stress (Fig. 2.2a). Stress at any point may also be resolved by rules of a Cartesian co-ordinate scheme, clearly described for geologists by Jaeger (1969) and Hobbs *et al.* (1976). Principal stresses may be defined as  $\sigma_1$ ,  $\sigma_2$ ,  $\sigma_3$  (Fig. 2.2b) as described by Nye (1964).

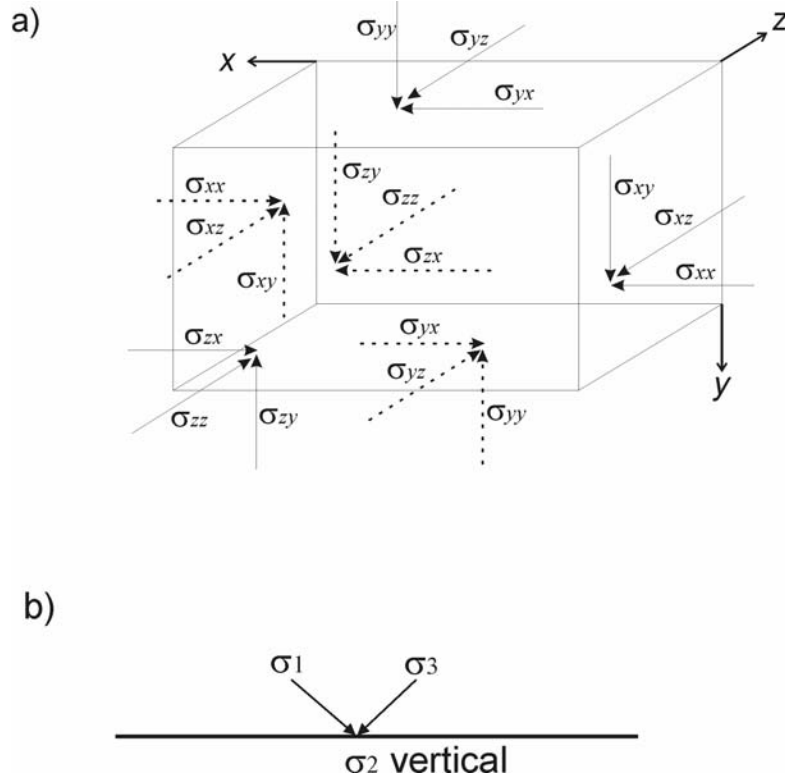


**Figure 2.2** Stress components a) block diagram depicting 3-dimensional components of stress; b) stress upon a plane resolved into cartesian co-ordinates.

In a body of rock when the three principal stresses are not equal the mean stress is defined as the pressure:

$$P = \frac{1}{3} (\sigma_{xx} + \sigma_{yy} + \sigma_{zz}) \text{ or } \frac{1}{3} (\sigma_1 + \sigma_2 + \sigma_3) \quad (2.1)$$

We can then define the deviatoric normal stresses by subtracting the pressure or mean stress as follows:

$$\begin{aligned} \sigma_{dxx} &= \sigma_{xx} - P & \sigma_{d1} &= \sigma_1 - P \\ \sigma_{dyy} &= \sigma_{yy} - P & \text{or } \sigma_{d2} &= \sigma_2 - P \\ \sigma_{dzz} &= \sigma_{zz} - P & \sigma_{d3} &= \sigma_3 - P \end{aligned} \quad (2.2)$$

In a column of rock the vertical stress or pressure acting upon it increases linearly with depth (Fig. 2.3a). Assuming density  $\rho$  is constant and that we know the depth or height of the rock overburden we can calculate the vertical stress acting upon this rock using:

$$\sigma_v = \rho gh \quad (2.3)$$

where  $\sigma_v$  is the vertical stress (MPa),  $\rho$  is the rock density ( $\text{kg m}^{-3}$ ),  $g$  is acceleration due to gravity ( $\text{ms}^{-1}$ ) and  $h$  is the depth or height of the rock overburden (m). When no fluids are present in the rock the vertical stress can be considered as the lithostatic stress acting upon the rock, where the mean value of stress in a simple column of rock can be considered the pressure. As there are normal forces acting on horizontal planes in the earth we also need to consider normal forces acting on the vertical planes (Fig. 2.3b). These horizontal normal stress components  $\sigma_{xx}$  and  $\sigma_{zz}$  are typically tectonic forces e.g. deviatoric stress, and this usually results in disequilibrium of forces where:

$$\sigma_{xx} \neq \sigma_{zz} \neq \sigma_{yy} \quad (2.4)$$

However, in the case of stress equilibrium where all three stresses are approximately equal (e.g. “stable” continental crust), the balance between this and the weight of the overburden is known as a lithostatic state of stress. When tectonic forces are apparent, the horizontal force  $F_c$  acting on a typical cross section of rock at depth is made up of both the lithostatic part and tectonic part:

$$\sigma_{xx} = \rho_c gy + \Delta\sigma_{xx} \quad (2.5)$$

The horizontal force  $F_c$  can be obtained by integrating the horizontal normal stress as follows (Turcotte & Schubert, 2002):

$$F_c = \int_0^h \sigma_{xx} dy = \int_0^h (\rho_c gy + \sigma_{xx}) dy = \frac{1}{2} \rho_c gh^2 + \sigma_{xx}h \quad (2.6)$$

where  $h$  is the height,  $\rho_c$  the rock density and  $g$  the gravitational force.

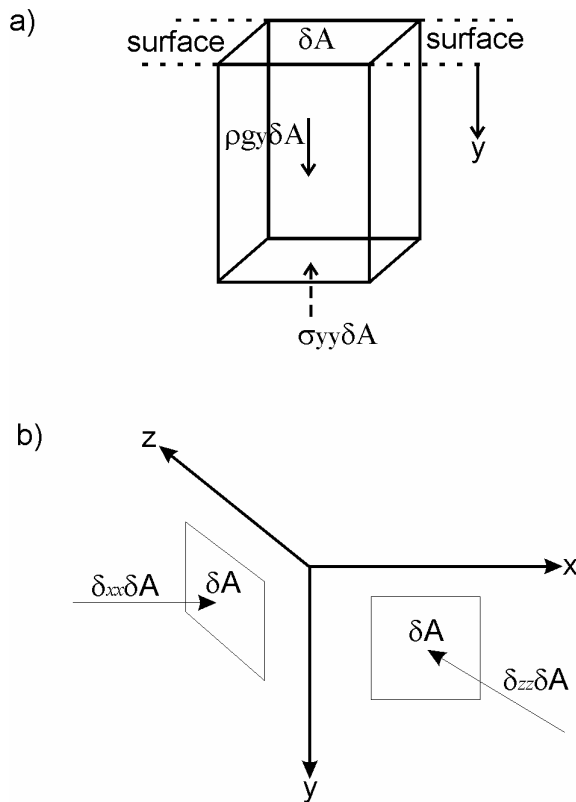


**Figure 2.3** Schematic diagrams a) displaying vertical stress in a column of rock, and b) horizontal surfaces forces acting on vertical planes.

In the case of the continental crust, which is buoyed up with a force equal to the weight displacement of the mantle (Archimedes principle)(Fig. 2.4), we can see a hydrostatic equilibrium is present with equal stresses;

$$\rho_c h = \rho_m b \quad (2.7)$$

where  $\rho_c$  is the density of the crust,  $h$  is the thickness of the crust,  $\rho_m$  is the density of the mantle and  $b$  is the depth in the mantle to which the crust sinks.

To maintain the integrity of the crust, a horizontal tensile stress is required

(Turcotte & Schubert, 2001). From Eqs. 2.6 and 2.7 we can extrapolate the horizontal stress as follows:

$$\Delta\sigma_{xx} = \frac{1}{2} \frac{\rho_m g b^2}{h} - \frac{1}{2} \rho_c g h = -\frac{1}{2} \rho_c g h \left(1 - \frac{\rho_c}{\rho_m}\right) \quad (2.8)$$

For example, the deviatoric stress,  $\Delta\sigma_{xx}$ , at a depth or height of 40km, density of the mantle ( $\rho_m$ ) = 3200kg m<sup>-3</sup> and density of the crust ( $\rho_c$ ) = 2700kg m<sup>-3</sup>, is -82.7 MPa. Typical values of horizontal tensile stresses in the earth's crust are on the order of 10 to 100 MPa (Turcotte & Schubert, 2002).

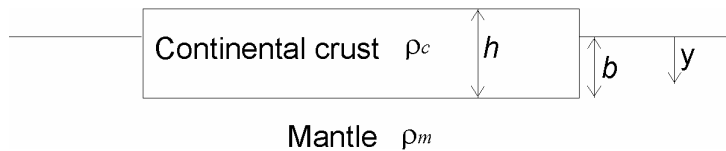


**Figure 2.4** Schematic diagram (from Turcotte & Schubert 2002) representing a block of continental crust 'floating' on a fluid mantle.

### 2.2.2 Elastic-Plastic Behaviour

In the geosciences we are interested in how rocks respond to stress and strain, and whether they deform in an elastic or plastic manner or both. It is generally accepted that it is appropriate to relate stress and strain of many solids using the laws of elasticity. Elastic materials deform when a force is applied and return to their starting condition when this force is removed, and the elastic strain of many rocks is linearly proportional to the applied stress. However, materials that display large elastic strains or strongly non-linear elastic behaviour are often modelled using more complex elastic relationships, which will vary as some function of the strain in the material. At low temperatures and

low confining pressures (e.g. near surface) rocks behave as brittle solids, where large deviatoric stresses cause fracture. At high stress levels and/or high temperatures, deviations from elastic behaviour occur.

Rocks buried deep in the earth are subjected to increasing confining pressures, principally due to overburden, and high temperatures, which may result in plastic deformation (irreversible deformation without fracture). Unlike the elastic model, when the applied force is removed some fraction of the deformation remains. The stress- strain relationships of elastic and elastic-perfectly plastic can be shown diagrammatically (Fig. 2.5a-e).

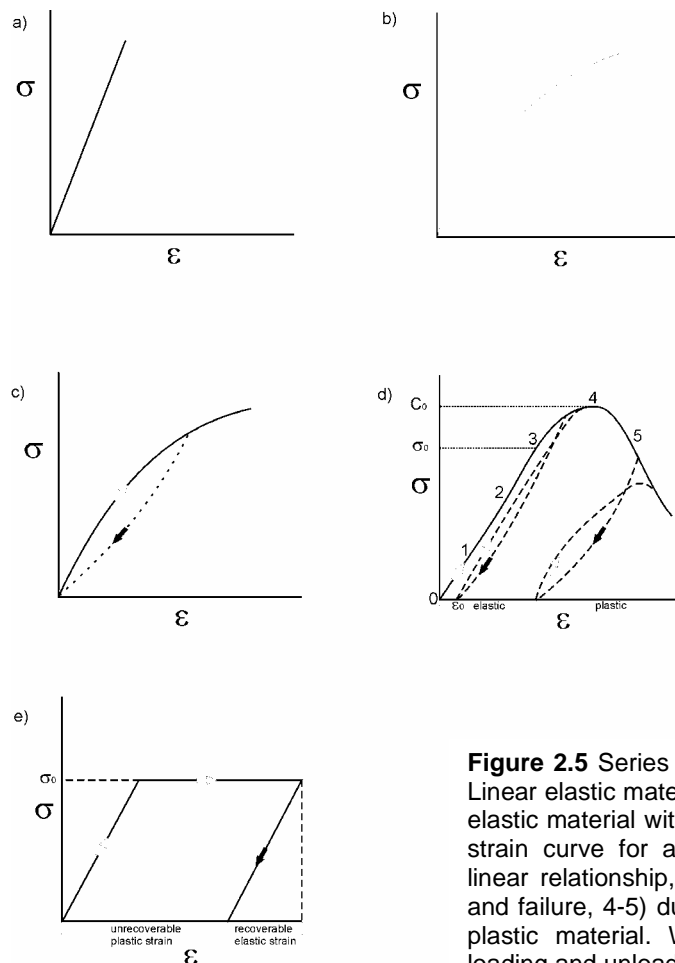


**Figure 2.5** Series of stress-strain curves showing a) Linear elastic material, b) perfectly elastic material, c) elastic material with hysteresis, d) a complete stress-strain curve for a rock 1-3) representing a nearly linear relationship, 3-4) reaching a maximum stress and failure, 4-5) during failure, e) an elastic-perfectly plastic material. White and black arrows indicate loading and unloading cycles respectively.

### 2.2.2.1 Elasticity

At low stress levels rocks generally behave elastically, and this can be considered as the result of the relationship between force and extension otherwise known as ‘Hooke’s Law’. This relationship can be expressed in terms of stress and strain using the elastic or Young’s modulus ( $E$ ), for the one dimensional case (Fig. 2.5a):

$$E = \frac{\sigma}{\varepsilon} \quad (2.9)$$

During deformation materials will deform in the direction of the applied force (Fig. 2.6), however, they have a tendency to either contract or expand in a transverse direction to the applied force (when subjected to either compressive or tensile forces).

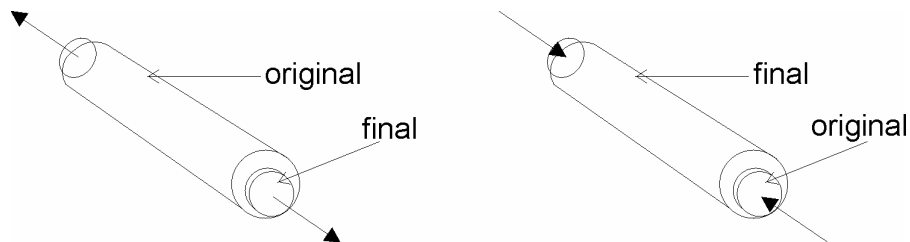


**Figure 2.6** Schematic diagram indicating the Poisson effect for uniaxial applied force, showing the changes from initial to final conditions for compression and extension.

This behaviour in elastic materials can be described in terms of Poisson’s ratio, and defined as:

$$\nu = \frac{\varepsilon_r}{\varepsilon_a} \quad (2.10)$$

where  $\varepsilon_r$  and  $\varepsilon_a$  are the radial and axial strains respectively. In the three dimensional case, Young's modulus and Poisson's ratio may be used to generalise Hooke's law:

$$\begin{aligned}\varepsilon_x &= \frac{\sigma_x}{E} - \nu \frac{\sigma_y}{E} - \nu \frac{\sigma_z}{E} \\ \varepsilon_y &= \frac{\sigma_y}{E} - \nu \frac{\sigma_x}{E} - \nu \frac{\sigma_z}{E} \\ \varepsilon_z &= \frac{\sigma_z}{E} - \nu \frac{\sigma_x}{E} - \nu \frac{\sigma_y}{E}\end{aligned}\tag{2.11}$$

If a linear relationship holds between shearing stress and shearing strain, then the shear modulus may be expressed as:

$$G = \frac{\tau}{\gamma}\tag{2.12}$$

where  $\tau$  and  $\gamma$  are the shear stress and strain respectively. Only two independent constants are required for the case of isotropic linear elasticity, and the shear modulus may be expressed as a function of Young's modulus and Poisson's ratio:

$$G = \frac{E}{2(1+\nu)}\tag{2.13}$$

The elastic bulk modulus can be defined in a similar manner to the Young's modulus and shear modulus:

$$K = \frac{P}{\varepsilon_v}\tag{2.14}$$

and also in terms of Young's modulus and Poisson's ratio:

$$K = \frac{E}{3(1-2\nu)}\tag{2.15}$$

The general assumption of a linear isotropic elastic material is that components of stress are linearly proportional to strains and material properties (Jaeger & Cook, 1976; Turcotte & Schubert, 2002). This relationship between stress and strain can be conveniently defined as:

$$\begin{aligned}\sigma_1 &= (\lambda+2G) \varepsilon_1 + \lambda\varepsilon_2 + \lambda\varepsilon_3 \\ \sigma_2 &= \lambda\varepsilon_1 + (\lambda+2G) \varepsilon_2 + \lambda\varepsilon_3 \\ \sigma_3 &= \lambda\varepsilon_1 + \lambda\varepsilon_2 + (\lambda+2G) \varepsilon_3\end{aligned}\tag{2.16}$$

where  $\lambda$  and  $G$  are the material properties known as Lamé parameters.

### 2.2.2.2 Plasticity

Plastic material behaviour, or plasticity, is defined by Zienkiewicz & Taylor (1989) as the presence of irrecoverable strains upon load removal. When the confining pressure of a rock reaches its brittle strength, a transition from elastic to plastic behaviour occurs (Fig. 2.5bc). This transition takes place when the stress exceeds a critical stress value, the yield stress ( $\sigma_0$ ), and involves some degree of permanent path-dependent deformation as a consequence of the non-linearity of the stress-strain relationship (Fig. 2.5d). This elastic-plastic transition is dependent on the loading history, and the temperature of the material has an important role to play, e.g. increasing temperature may decrease yield stress. The stress-strain curves are generally assumed to be independent of the rate of application of the load, hence there is a time-independent stress-strain relationship. The idealistic representation would be an elastic-perfectly plastic material (Fig. 2.5e), where the material behaves elastically at stresses below that of the yield stress ( $\sigma_0$ ), and deforms without sustaining any stress greater than this so that it will flow indefinitely at this

stress unless restricted. The yield criterion is a relationship between the principal stresses, and in the one-dimensional case the condition for plastic yield is when:

$$\sigma = \sigma_0 \quad (2.17)$$

In three dimensions however, the relationship is more complicated and there are two criteria in general use, 1) the Tresca or maximum shear stress criterion (Tresca, 1868), and 2) the von Mises criterion (von Mises, 1913). The Tresca criterion states that a solid will yield when the maximum shear stress reaches a critical value  $\sigma_c$  or attains one half of the yield stress of the material (the maximum shear stress in a three dimensional state of stress is one half the difference between the maximum and minimum principal stresses). Thus the Tresca yield condition is:

$$\sigma_c = \frac{1}{2} (\sigma_1 - \sigma_3) \quad (2.18)$$

when reduced to the yield condition for uniaxial stress ( $\sigma_2 = \sigma_3 = 0$ ) we have:

$$\sigma_c = \frac{1}{2} \sigma_1 = \frac{1}{2} \sigma_0 \quad (2.19)$$

which results in the final form of the Tresca condition:

$$\sigma_0 = \sigma_1 - \sigma_3 \quad (2.20)$$

The von Mises criterion states that plastic yielding will occur when:

$$\sigma_c^2 = (\sigma_1 - \sigma_2)^2 + (\sigma_1 - \sigma_3)^2 + (\sigma_2 - \sigma_3)^2 \quad (2.21)$$

when reduced to the yield condition  $\sigma_0 = \sigma_1$  when  $\sigma_2 = \sigma_3 = 0$  so that:

$$\sigma_c^2 = 2\sigma_1^2 = 2\sigma_0^2 \quad (2.22)$$

thus the von Mises criterion is:

$$2\sigma_0^2 = (\sigma_1 - \sigma_2)^2 + (\sigma_1 - \sigma_3)^2 + (\sigma_2 - \sigma_3)^2 \quad (2.23)$$

Deviations from the Tresca and von Mises criterion in principal stress space is best described by two common criterion used in modelling clays, soils or rock a) Drucker-Prager and b) Mohr-Coulomb, which show a change in yield surface and allow degeneration towards the von Mises or Tresca criterion (Fig. 2.7)(for a more detailed description see Itasca (2000a)).

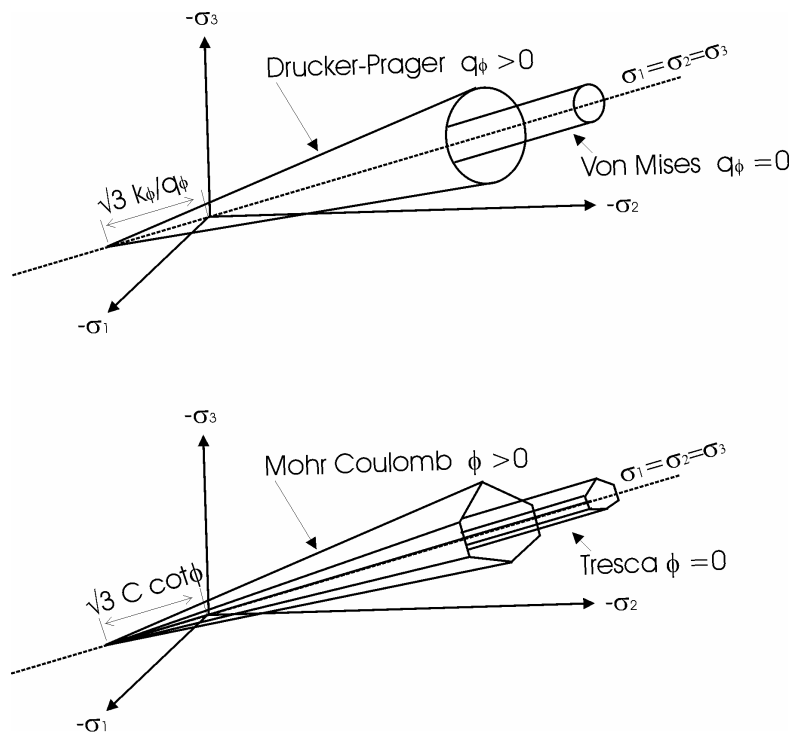


**Figure 2.7** Schematic diagrams indicating the relationship of failure envelopes in principal stress space.

Plasticity models are widely used to describe plastic material behaviour, and four main points must be specified in any such model (Britto & Gunn, 1987):

1. A yield function which describes the combination of stresses required to induce yield.
2. A relationship between the direction of principal plastic strain increments and principal stresses.
3. A flow rule, which specifies the relative magnitudes of incremental plastic strains when the material is yielding.
4. A hardening relation, which describes the expansion or contraction of the yield surface with plastic strain (or energy dissipation).

The yield function provides a boundary up to which only elastic behaviour occurs. As stress states never lie outside the yield surface by definition (for rate independent plasticity), increasing plastic strains either occur at constant stress (perfect plasticity) or cause the yield surface to harden (strain hardening) or soften (strain softening). The general yield criterion (Zienkiewicz & Taylor, 1989) may be expressed as:

$$F(\underline{\sigma}, \Psi) = 0 \quad (2.24)$$

where  $\Psi$  is some hardening parameter (e.g. plastic volumetric strain for critical state models). Plastic strain increments are related to plastic stress increments based on the assumption of potential flow, thus:

$$d\underline{\epsilon}^{pl} = d\lambda \frac{\partial Q}{\partial \underline{\sigma}} \quad (2.25)$$

where  $d\lambda$  is a constant of proportionality describing the magnitude of plastic strain increments,  $Q$  is the flow potential or plastic potential, and  $\partial Q / \partial \underline{\sigma}$  the direction of plastic strain increments. When used in the associated plasticity

case (if the potential and yield functions coincide), the flow potential  $Q$  is coincident to the yield surface (Fig. 2.8c):

$$Q = F \quad (2.26)$$

In the non-associated plasticity case  $Q$  and  $F$  are not coincident and may be defined by a flow potential, such as (Fig. 2.8d):

$$Q = Q(\underline{\sigma}, \Psi) \neq F \quad (2.27)$$

The normality principle, where incremental plastic strain is normal to the yield surface, may not hold for materials in which frictional mechanisms dominate the deformation i.e. where frictional sliding is interpreted as plastic strain, in which case non-associated plasticity should be used (Rudnicki & Rice, 1975; Chen, 1982; Vermeer & de Borst, 1984; Ord, 1991a). The differences between associated and non-associated plasticity can be shown schematically in two-dimensional stress space (Fig. 2.8a-d).

In the case of isotropic plasticity models, the yield surface may be expressed in terms of the principal stresses, or stress invariants. Yield surfaces for common plasticity models can be expressed as:

Huber-von Mises: 
$$F = q - \sigma_y (\dot{\epsilon}^{pl}) = 0 \quad (2.28)$$

Mohr-Coulomb: 
$$F = \tau^* + \sigma^* \sin \phi - c \cos \phi = 0 \quad (2.29)$$

Drucker Prager: 
$$F = t - p \tan \phi - c = 0 \quad (2.30)$$

Modified Cam-clay: 
$$F = \frac{1}{\beta^2} \left( \frac{p}{p_c} - 1 \right)^2 + \left( \frac{t}{Mp_c} \right)^2 - 1 = 0 \quad (2.31)$$

where  $\sigma_y$  is the yield stress in a uniaxial test,  $\beta$  is a material parameter which modifies the curvature of the Cam-clay yield surface,  $p_c$  is the intercept of the yield surface which changes strain hardening/softening,  $M$  is the slope of the critical state line,  $\phi$  is the friction angle of the material,  $c$  is the cohesion of the material,  $t$  is a deviatoric stress measure,  $\tau^*$  is the maximum shear stress and  $\sigma^*$  is the mean stress.

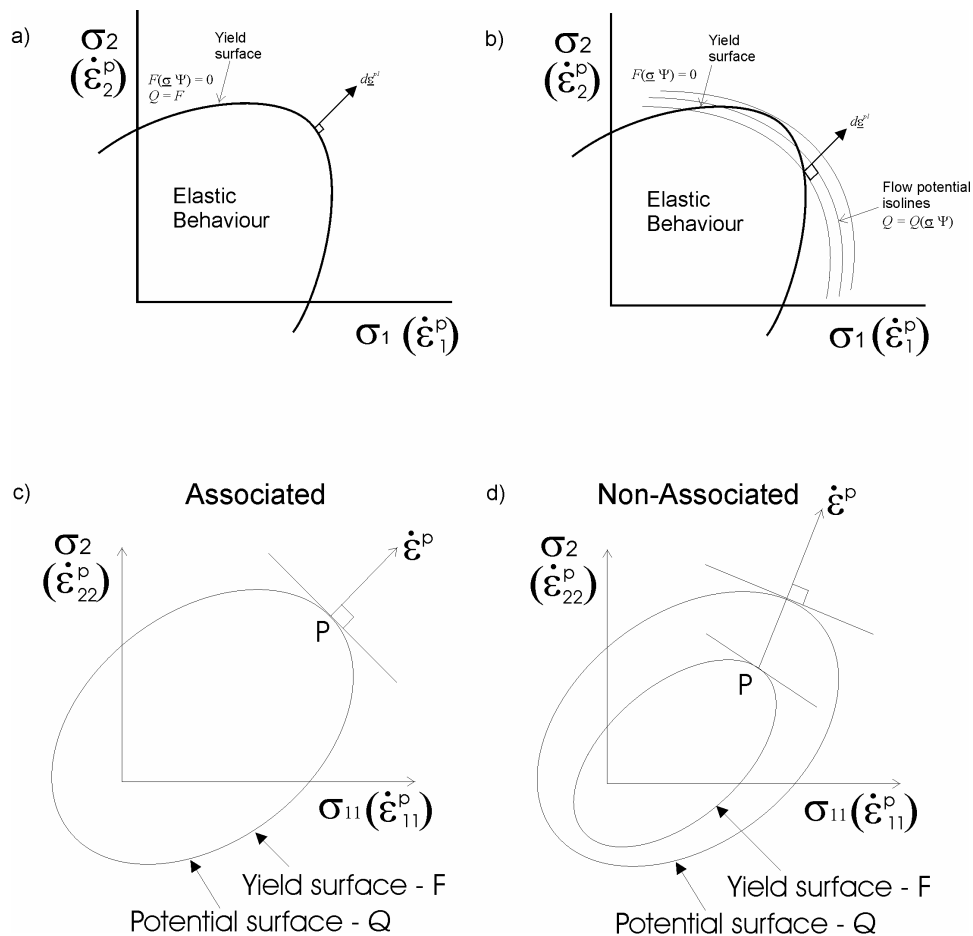


**Figure 2.8** Schematic 2-dimensional representation of yield surface and plastic strain increments for a) associated, b) non-associated plasticity. Representation of coincidence of the yield surface and potential surface in c) associated and d) non-associated cases.

Several plasticity models have been developed for porous materials e.g. soil mechanics, rocks mechanics and fibrous solids, and these models usually allow for plastic volume change observed during deformation. As this study is primarily concerned with the effects of deformation on porous media, the Mohr-Coulomb constitutive model is best suited to this application. The yield in Mohr's space is defined by the relationship of shear stress ( $\tau_s$ ) and normal stress ( $\sigma_n$ ) acting on a plane, orientated at  $(\frac{\pi}{4} \pm \frac{\phi}{2})$  to the maximum principal stress ( $\sigma_1$ )(Jaeger & Cook, 1976; Ord, 1991a) where:

$$|\tau_s| = c - \sigma_n \tan \phi \quad (2.32)$$

Negative values of the yield function  $F$  (Eqn.2.29) are assumed to represent elastic deformation as this lies within the yield surface, and positive values are not allowed as plastic deformation takes place to keep stress on the yield function. The flow rule is used to describe the relationship of strain rates and the orientation of stress as seen in Eqn.2.25, the plastic potential function  $Q$  can be defined in a similar fashion to the yield function  $F$  (Vermeer & de Borst, 1984; Ord, 1991) as:

$$Q = \tau^* + \sigma^* \sin \psi - \text{constant} \quad (2.33)$$

so that the dilation angle ( $\psi$ ) meets the same requirements in the plastic potential function as the friction angle ( $\phi$ ) does in the yield function (c.f. Eqn 2.29). The flow rule states that the plastic strain rate is normalised to the potential surface described by  $Q$  and the relative magnitudes of the dilation (see below) and friction angles determine whether or not the yield and potential surfaces are parallel. When  $\phi = \psi$  this leads to normality of the plastic strain rate vector to the yield surface and an associated flow rule (Fig. 2.8c). In geological

materials that are dilatant, and have zero cohesion, associated behaviour appears unrealistic as equivalence of the dilation and friction angles would lead to no plastic work being done during plastic deformation. In non-equivalence,  $\phi \neq \psi$ , the plastic strain rate vector is normal only to the plastic potential surface, which leads to a non-associated flow rule (Fig. 2.8d). This relationship, which has been described by Vermeer & de Borst (1984) and Ord (1991a) in some detail, is arguably the best model for describing both elastic and plastic deformation in mid to upper-crustal rocks. Purely viscous flow, perhaps applicable to the lower crust or mantle, is not considered here.

### 2.2.3 Constitutive Models

Constitutive models and laws allow a mathematical description of how material e.g. rock, will respond to an applied force. The choice of constitutive models and relationships used for modelling a material is dependent on the material in question (e.g. soft clays, soils or lithified rock) and the problem posed (e.g. deformation of a dilatant material and associated fluid flow). A broad distinction can be drawn between the many traditional constitutive models used in numerical modelling, and these models fall into two main groups: 1) elastic models and 2) plastic models. Elastic models provide the simplest representation of material behaviour and are valid for linear stress-strain behaviour of homogenous isotropic continuous material. However, these models can be modified to represent transverse isotropic material in which there are differences in elastic moduli for different orientations within the material. The plastic model group allows realistic modelling of geological materials such as clay, soils, sand and rock and can model non-linear

relationships in such materials. Widely used constitutive models include 1) The Cam-clay model (used to represent soft materials such as clay when the influence of volume change on bulk property and the resistance to shear need to be considered) 2) the Drucker-Prager model (to model soft materials such as clay or soil with low friction angles) and 3) the Mohr-Coulomb model, which is the most conventional model used to represent shear failure in consolidated soils and rock. The classical Mohr-Coulomb material with non-associated plasticity (see below) is regarded as a reasonable representation of the rheology of mid to upper crustal rocks (Vermeer & de Borst, 1984; Hobbs *et al.*, 1990; Ord & Oliver, 1997) and this is the constitutive model used in the elastic-plastic coupled deformation and fluid flow models in this study.

As with all constitutive models the Mohr-Coulomb model can be modified to incorporate strain hardening/softening behaviour by varying model properties such as cohesion, friction, dilation or tensile strength, as a function of the deviatoric plastic strain. These material properties are allowed to increase (hardening) or decrease (softening) following the onset of plastic yield, in contrast to the standard Mohr-Coulomb model in which the material properties are assumed to remain constant (Fig. 2.9).

#### 2.2.4 Porous Media and Fluid Flow

A porous media can be simply described as “a solid with holes in it” (Greenkorn, 1983). At broad scales, the earth is comprised of material that can be considered porous (whether due to pore space or fractures), and this pore space has a large potential to store fluids. The effects of this fluid, its movement

and resultant fluid pressures have great importance on the deformation of porous material and ultimately the transport of metals and consequent mineralisation. The problems involved in the analysis of fluid flow through rock masses are complex, and there are two different scales to be considered. In rock mechanics and soil mechanics the medium involved can be separated into microscopic and macroscopic parts, which involve discrete particle boundaries e.g. soils, through to fractures e.g. rocks. However, both can be simplified by treating all rock masses as a continuum in which small scale fractures can be considered as interconnected pore space in continuum mechanics.

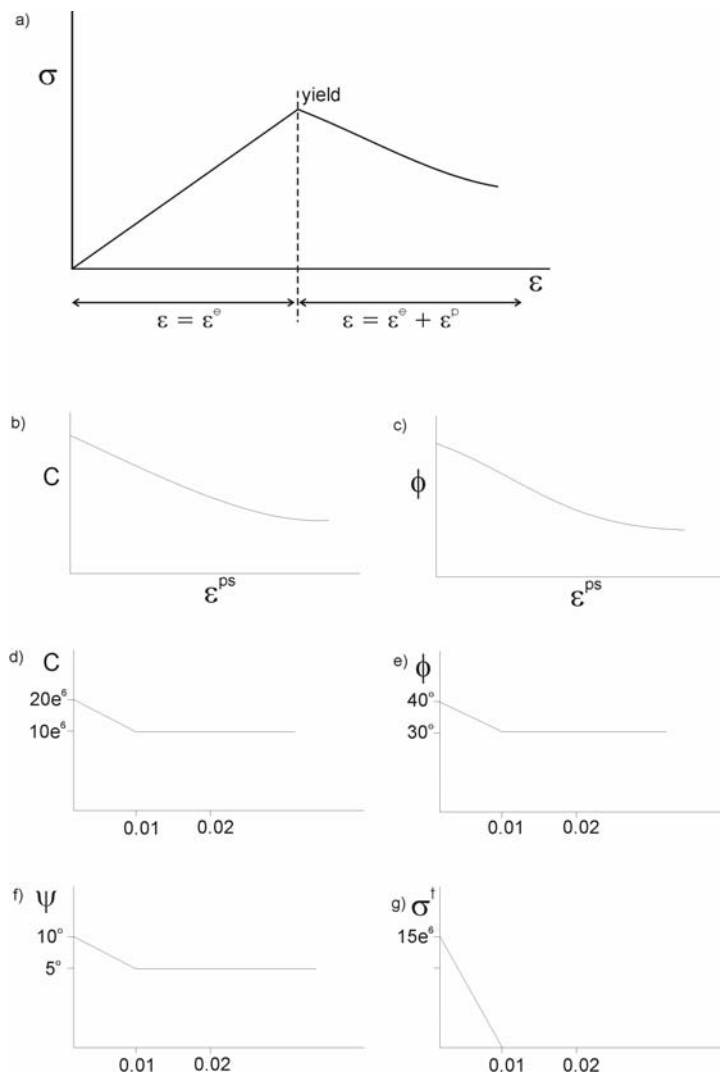


**Figure 2.9** One dimensional stress-strain curves displaying strain softening behaviour; a) Example of the stress-strain curve showing softening on yield of the material, b) variations of cohesion ( $C$ ) and c) friction angle ( $\phi$ ) as a function of plastic strain; d-g) examples of softening behaviour in cohesion ( $C$ ), friction angle ( $\phi$ ), dilation angle ( $\psi$ ) and tensile strength ( $\sigma^t$ ) variance as a function of the plastic portion of total strain. (Adapted from Itasca, 2000a).

Another approach to modelling discrete fractures is the discontinuum approach, which treats fractures as discrete surfaces or volumes. Due to the complexity of numerically combining continuous and discrete elements the theoretical component of this section will initially treat rock masses as a continuum. Fluid flow in discrete fractures at a macroscopic scale is covered in the following section. The two end members (porous flow and fracture flow) in geological materials require a convergence of both and as yet no numerical code can adequately simulate both types of fluid flow, although proxy attempts have been made in continuum, discrete element and particle codes.

Darcy's law is a macroscopic relation, therefore, we need to consider the use of representative elementary volumes (Bear, 1972). This volume must be large enough to represent a meaningful statistical average of the continuum under consideration (Freeze and Cherry, 1979). There has been much discussion on the volume of material e.g. fractured rock, to represent the whole rock in a continuum sense, and this approach has been used in many geomechanical modelling studies (Ord and Oliver, 1997; Domenico and Schwartz, 1998; Oliver *et al.*, 1999, 2001). At this point it seems pertinent to note that this study uses an approach, whereby two numerical codes FLAC (continuum modelling) and UDEC (discontinuum modelling) are utilised to analyse both ends of the spectrum.

In order to describe the state of a porous medium, we need to incorporate some parameter that describes the composition of the medium in terms of pores or void space and solid material, as the fundamental properties of a porous

medium are the amount of pore space which is described as a void (not filled by solid material) and the rate of movement of water or other fluid through the medium (Jaeger & Cook, 1976). Three such measures to describe the fundamentals of porous media can be described by the porosity ( $n$ ), void ratio ( $e$ ) and specific volume ( $v$ ), defined as:

$$n = \frac{V_v}{V_t} \quad (2.34)$$

$$e = \frac{V_v}{V_s} \quad (2.35)$$

$$v = \frac{V_t}{V_s} = 1 + e \quad (2.36)$$

where  $V_v$  is the void volume,  $V_t$  is the total volume, and  $V_s$  is the volume of the solid. The study of porous medium mechanics began with Darcy (1856), who investigated the flow of viscous fluids through porous media (Fig. 2.10). Darcy's law is expressed in terms of the experimentally measured quantities as:

$$Q = \frac{KA(h_1 - h_2)}{L} \quad (2.37)$$

where  $Q$  is the fluid volume flow rate through a porous medium ( $\text{m}^3 \text{s}^{-1}$ ),  $K$  is the hydraulic conductivity of the porous medium ( $\text{m s}^{-1}$ ),  $A$  is the cross-sectional area ( $\text{m}^2$ ) of flow,  $h_1 - h_2$  is the difference in piezometric head (m) across the porous medium, and  $L$  is the length (m) of the porous medium. The hydraulic conductivity ( $K$ ) is a coefficient of proportionality, which depends on the properties of both the solid matrix and the fluid, and given as:

$$K = \rho g \frac{k}{\eta} \quad (2.38)$$

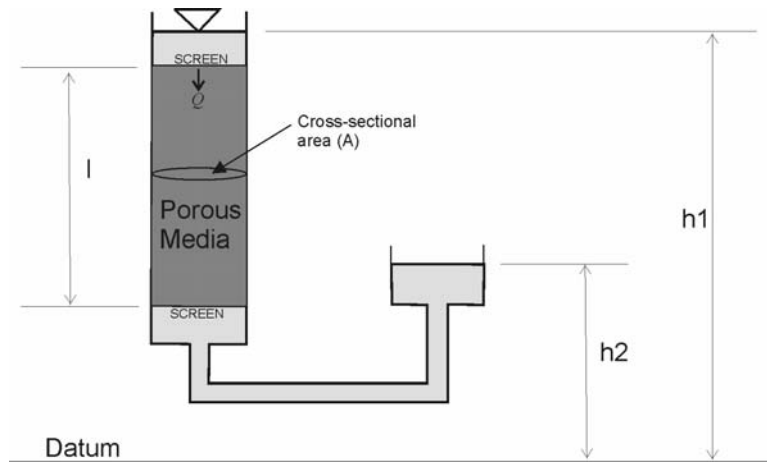


**Figure 2.10** Representation of Darcy's experiment for porous media flow.

Bear (1972) describes the relevant fluid properties as density and dynamic viscosity and separation of these from the hydraulic conductivity allows the definition of the intrinsic permeability ( $k$ ) which is dependent only on the solid matrix, and can be expressed as:

$$k = \frac{\eta K}{\rho g} \quad (2.39)$$

where  $\rho$  is the fluid density ( $\text{kg/m}^3$ ),  $g$  the gravitational acceleration ( $\text{m/s}^2$ ) and  $\eta$  the dynamic viscosity of the fluid ( $\text{Pa}\cdot\text{s}$ ). The specific discharge or macroscopic velocity ( $q$ ) within the cross sectional area can be defined as:

$$q = \frac{Q}{A} \quad (2.40)$$

and assuming constant fluid density, Darcy's law may be expressed in the one dimensional form:

$$q = -\frac{k}{\eta} \frac{\partial P}{\partial x} \quad (2.41)$$

where  $\partial P / \partial x$  is the fluid pressure gradient in the direction of flow.

Darcy's law has been validated using experimental and theoretical investigations, however deviations from the linear relationship often occur at high flow rates (Fig. 2.11).

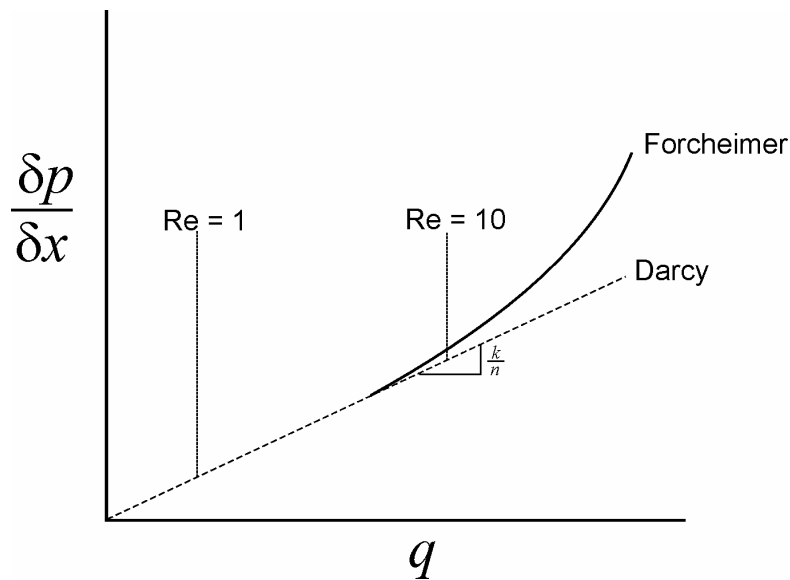


**Figure 2.11** Schematic representation of Darcy's and Forcheimer's equations for one dimensional flow, showing deviation from Darcy's law at high flow rates.  $\delta p / \delta x$  represents the fluid pressure gradient, and  $q$  represents the specific discharge.

Some derivations from Darcy's law have been defined and validated by examining the linearity of flow or Reynolds number for porous media (Bear, 1972). This can be expressed as:

$$\text{Re} = \frac{qd}{\eta / \rho} \quad (2.42)$$

where  $d$  is some length dimension of the porous media or matrix, usually taken as the average solid grain diameter in porous granular material. Bear (1972) states that Darcy's law is valid provided the Reynolds number lies between 1

and 10. The derivations from Darcy's Law lead to other theoretical forms of the permeability relationships of non-linear flows e.g. Forchheimer and Kozeny-Carman. Oliver and Bons (2001) also suggest that non-Darcian fluid flow may occur in "mobile hydrofractures" in which the fluid and fracture move at the same rate and the permeability of any rock is only transitionally high. However, these relationships are considered outside the scope of this study, due to limitations of the software available for this project.

The movement of crustal fluids occurs as a response to pressure gradients and topographic influence or additional height modifies the stress regime resulting in an invariant relationship and constitutive relationship. Hydraulic head ( $H$ ) is a measure of mechanical energy per unit weight of fluid, equivalent to the height above an arbitrary datum e.g. sea level, to which fluid will rise in a well. The simplest form of equation describing hydraulic head contains an elevation and pressure term:

$$H = z + P/\rho g \quad (2.43)$$

where  $H$  is the hydraulic head,  $z$  is the elevation above a datum,  $P$  is the pore fluid pressure,  $\rho$  is the density of the fluid, and  $g$  is the acceleration due to gravity. Darcy's Law shows that differences in hydraulic head are required for flow to occur and the governing equation determining fluid flow in a porous media can be expressed as a simplified form of Darcy's Law:

$$V_i = k_{ij} \frac{\gamma^f}{\eta^f} \left( \frac{\partial H}{\partial x_j} \right) \quad (2.44)$$

where  $V_i$  is the Darcy fluid velocity ( $\text{ms}^{-1}$ ),  $k_{ij}$  is the permeability tensor ( $\text{m}^2$ ),  $\gamma^f$  is the specific weight ( $\text{kg m}^{-2} \text{s}^{-2}$ ),  $\eta^f$  is the viscosity of the fluid ( $\text{kg m}^{-1} \text{s}^{-1}$ ),  $H$  is the

hydraulic head ( $P/\rho g+z$ ) (m) and  $x_j$  is the position of a material point. Darcy fluid flow vectors are by definition orthogonal to contours of hydraulic head in an isotropic medium with a constant density.

Terzaghi (1925) first introduced the principle of effective stress on experimental grounds, and this concept was instrumental in understanding the relationship of stress and pore fluid pressure in solid-liquid systems. The principle demonstrates the relationship or sharing of an applied force within the porous media and pore fluid, and effective stress can be defined by:

$$\sigma' = \sigma - p_f \quad (2.45)$$

where  $\sigma$  is the total stress and  $p_f$  is the pore fluid pressure. Terzaghi (1943) stated that:

- 1) If the external hydrostatic stress ( $\sigma_1 = \sigma_2 = \sigma_3$ ) and pore pressure ( $p_f$ ) are increased by the same amount, there is a negligible change in volume in comparison to the case where only the stress alone is increased.
- 2) During shear failure there is no increase in the shear strength if both the normal stress ( $\sigma_n$ ) and the pore pressure ( $p_f$ ) are increased by the same amount. However, if the normal stress alone is increased there is a considerable increase in shear strength.

Terzaghi (1943) concludes that neutral stress has no influence on deformation of porous media and that the deformation is controlled by the effective stress ( $\sigma'$ ). The neutral stress has been regarded as a basic hydrostatic stress that is present in both the solid and liquid parts, and the effective stress arises exclusively from the solid (e.g. Terzaghi, 1945; Hubbert & Ruby, 1959). The

role of pore pressure ( $p_f$ ) on failure of rocks can be seen by its relationship to effective stress. As a result of increasing pore pressure and lowering of the effective stress, rock materials become more susceptible to failure during deformation (e.g. Cox, 1995; Sibson, 1992, 1998). Oliver *et al.* (1990) and Oliver (1995) have modelled this relationship, highlighting areas of low mean effective stress, correlated with the distribution of intense alteration, and veining in the Mary Kathleen fold belt, North West Queensland. This relationship may also be displayed diagrammatically in a Mohr circle sense, whereby lowering of effective stress may be driven by a pore pressure increase (Fig. 2.12). Handin *et al.* (1963) amongst others have shown that the concept of effective stress causing failure is true for rocks (e.g. siltstones, sandstones and limestones) provided the rock mass can be considered as a material with an interconnected system of pores. We can therefore assume that the controlling factor of failure in a porous material, such as rock, is the effective stress.

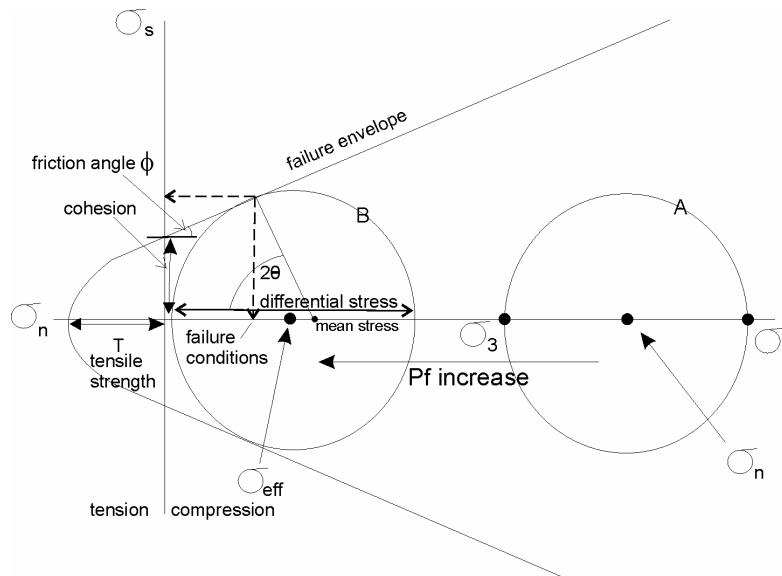


**Figure 2.12** Mohr Circle analysis diagram showing aspects of stress, fluid pressure and failure. Mohr Circle A might represent a starting condition, B an increase in fluid pressure lowering the effective stress and leading to non-recoverable failure i.e. shear.

Fluid flow in porous media is primarily driven by changes in hydraulic head and differences in pore pressure, and as already stated, can be expressed by Darcy's law. However, deformation-induced fluid flow in a porous media is primarily driven by volume changes in the material. In a homogenous material, plastic deformation can lead to localisation of strain and subsequent fluid flow (Ord, 1991a). Geological materials can be considered as a pressure-sensitive dilatant material (Edmond and Paterson, 1972; Ord, 1991a) in which dilatancy is associated with changes in both porosity and permeability. Experimental work has shown the influence of confining pressure on dilatancy of geological materials (Fig. 2.13) and these materials can show dilatancy in both the elastic and plastic parts of deformation.

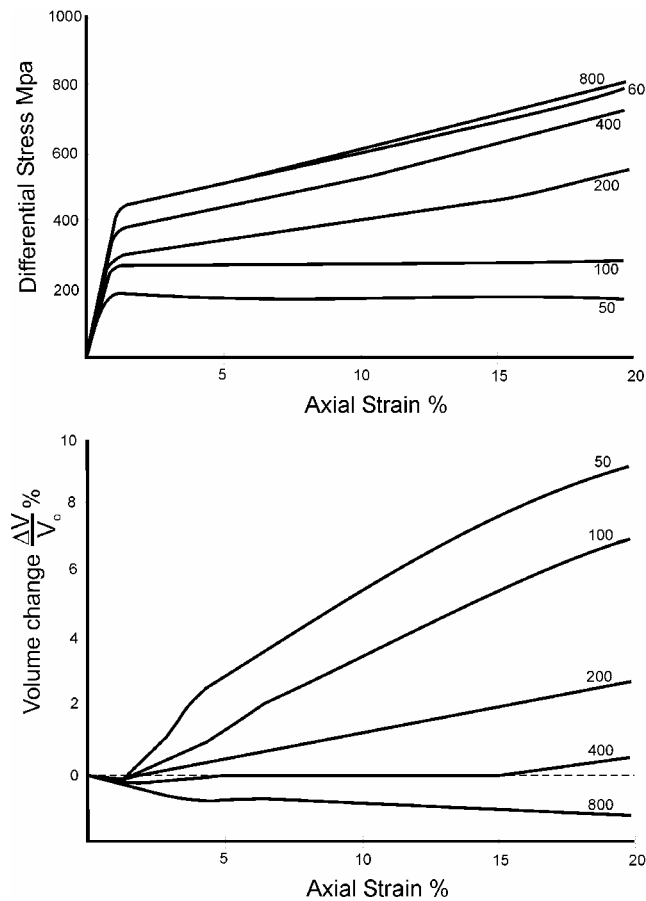


**Figure 2.13** Results from deformation experiments on Carrara marble by Edmond & Paterson (1972); a) differential stress-axial strain curves at different confining pressures (MPa), materials are strongly dependent on confining pressure and b) Volume change-axial strain curves, show dilatancy in both elastic and plastic parts of the stress strain curve.

Dilatant behaviour can be conveniently described in terms of the dilation angle ( $\psi$ ) as introduced in the previous section. This concept can be simplified as the result of frictional sliding of microfractures or grain boundaries during deformation (Fig. 2.14), and this behaviour may be repeated within volumes of rock at much larger scales, which can be interpreted as sliding on joints, bedding planes and faults (Ord and Oliver, 1997).

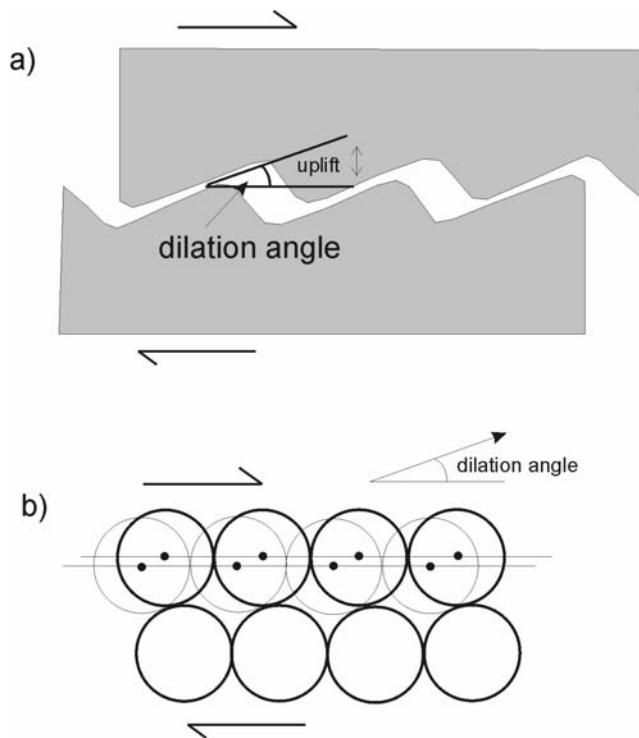


**Figure 2.14** Microstructural interpretations of the dilation angle in geo-materials during shear stress, where an increase in volume may be noted due to a) surface irregularities, or b) the sliding of grains over one another (after Vermeer & de Borst, 1984).

The fractional change in porosity or pore space can be defined by:

$$\frac{\Delta V}{V} = \tan \alpha \tan \psi \quad (2.46)$$

where  $\alpha$  is the angle of shear in a material and  $\psi$  is the dilatancy angle of the material. As a dilatant Coulomb material deforms, the angle of dilatancy can be related to strain:

$$\sin \psi = \frac{\varepsilon_v^p}{\gamma^p} \quad (2.47)$$

where  $\varepsilon_v^p$  is the rate of plastic volumetric strain and  $\gamma^p$  is the rate of plastic shear strain. Although a positive dilation angle represents a microstructural uplift, negative dilation angles are also possible, hence, a volume decrease in rocks undergoing compaction may be represented as negative dilation. As this study does not rely on the 'poro-elastic' effect (e.g. Ge and Garven, 1992) and is based on a 'poro-plasticity' approach, the effect of deformation induced dilatancy is an important mechanism responsible for driving fluid flow in the coupled deformation and fluid flow models discussed in later chapters.

### 2.2.5 Fluid Behaviour and Discrete Fractures

Any material that flows in response to an applied stress can be considered a fluid, and fluids deform continuously under applied forces (Turcotte and Schubert, 2002). Strain rates in fluids are a consequence of velocity gradients or rates of displacement of fluid elements and the rheological law for a fluid can determine this relationship. This behaviour can be either Newtonian or Non-Newtonian, with reference to Newtons laws of motion. In a Newtonian fluid, the strain rate or velocity gradient is linearly proportional to the applied stress. In the one dimensional case a fluid can move as a result of an applied pressure gradient or as a result of shear. For a fluid with a constant viscosity ( $\mu$ ) the shear stress can be expressed as:

$$\tau = \mu \frac{du}{dy} \quad (2.48)$$

The viscosity of a Newtonian fluid can be considered the constant of proportionality between the shear stress and strain rate, hence, a more viscous fluid would require a larger stress to produce a given shear. The viscosity of a fluid is commonly expressed in terms of the 'kinematic viscosity' ( $\nu$ )( $\text{m}^2 \text{s}^{-1}$ ), frequently used in fluid mechanics, and this is the ratio of viscosity  $\mu$  (Pa s) to the fluid density  $\rho$  ( $\text{kg m}^{-3}$ ), such that:

$$\nu = \frac{\mu}{\rho} \quad (2.49)$$

The concept of viscosity being independent of the velocity gradient in straight and parallel flow is met for most fluids, however, some fluids show non-linear characteristics where the viscosity is not independent of the rate of shear and these fluids can be described as Non-Newtonian. For the purpose of this study fluids are considered Newtonian due to the complexity of modelling Non-Newtonian behaviour. The influence of viscosity on flow is very complex and the shear stresses resulting from viscosity may be included in the equations of motion, however, the arising partial differential equations (Navier-Stokes equations) have no fully known general solutions.

If we consider flow through a fracture, pipe or channel, there are two basic types of fluid flow, 1) laminar flow and 2) turbulent flow. During laminar flow the fluid particles are generally considered to be moving in straight lines, even though velocities may vary between layers. The fluid can therefore be considered as moving in layers or laminae usually parallel to in-situ boundaries e.g. fracture walls. In non-laminar or turbulent flow, fluid particles have a

stochastic relationship and display particle velocities in many directions; however, the general or average motion of the fluid can be considered parallel to in-situ boundaries. For the purpose of this study fluid motion is considered laminar.

During the fracturing of rock materials the condition of tensile failure at high fluid pressures can be expressed as:

$$P_f > \sigma_3 + T \quad (2.50)$$

where  $\sigma_3$  is the minimum compressive stress (Pa) and  $T$  is the tensile strength (Pa) of the rock (e.g. Etheridge *et al.* 1983), with the geometry of the fracture being related to the applied stress field. In describing fluid flow in fractured rock materials, when the condition of a continuum does not exist, it must be described in relation to flow through an individual fracture or fracture set. The requirements for this are that we need information on fracture orientation, fracture density, connectivity, smoothness of fractures and aperture size. Snow (1968) developed equations to examine the permeability or equivalent hydraulic conductivity of a material with a set of planar fractures:

$$K = \frac{\rho_w g N b^3}{12\mu} \quad (2.51)$$

and

$$k = \frac{N b^3}{12} \quad (2.52)$$

where  $K$  is the hydraulic conductivity ( $\text{m s}^{-1}$ ),  $k$  is the permeability ( $\text{m}^2$ ),  $b$  is the aperture (m) and  $N$  is the number of joints per unit distance. For a given gradient in hydraulic head, fluid flow through a fracture is proportional to the cube of the fracture aperture, as in the 'Cubic Law' (Romm, 1966):

$$Q = \frac{\rho_w g b^2}{12\mu} (bw) \frac{\delta h}{\delta l} \quad (2.53)$$

where  $Q$  is the volumetric flow rate,  $\rho_w$  is the density of the fluid,  $g$  is the gravitational acceleration,  $\mu$  is the viscosity,  $b$  is the aperture opening,  $w$  is the fracture width perpendicular to flow direction, and  $\delta h/\delta l$  is the gradient in the flow direction. The roughness of fracture walls will have an influence not only on the degree of turbulent flow but also on the hydraulic conductivity due to variations in aperture openings. This relationship can be simulated by the addition of a variable related to the fracture's roughness, which thus reduces hydraulic conductivity as the fracture walls deviate from smooth parallel sides.

Orientation of existing fracture networks relative to an applied stress regime has a great influence on flow, and the most permeable or dilational fractures or faults are orientated at a low angle relative to the maximum compressive stress ( $\sigma_1$ ) and a high angle to the minimum compressive stress ( $\sigma_3$ ). The connectivity of such fracture networks has a strong bearing in the search for mineralised or barren faults, and this type of analysis can be used as a predictive tool in prospective terranes. In this study (Chapter 5) numerical modelling techniques are used to investigate the effect of varying stress distributions around a suite of intrusive rocks, and what influence they may have on fault networks, fluid flow and potential mineralisation in the Eastern succession.

### 2.3 Modelling Process

Experimental work and observations have traditionally been used to explain many natural processes; however, modern techniques in mathematics and

computer technology have allowed the implementation of numerical methods, which provide a soundly based alternative approach. This section examines the procedure and process for geomechanical modelling, in an attempt to clarify the concepts and purpose for this study.

### 2.3.1 Numerical Procedure

The theoretical approach involves a mathematical description of the system and processes involved and may attempt to provide analytical solutions to questions posed. However, physical processes in complex systems such as rock-fluid interactions coupled with deformation make it extremely difficult to find true analytical solutions but do provide an acceptable approximation of the system. Numerical models are always based on several assumptions about the system, and this has to be considered when a solution is reached. Before commencing any modelling procedure, questions must be addressed that will help define the main problems to be solved. Within the pmd\*<sup>2</sup>CRC a whole system analysis is a useful such approach and the main five questions addressed are:

- 1) What is the architecture and size of the total mineralising system?**
- 2) What is the geodynamic history?**
- 3) What were the physical and chemical characteristics of the fluids involved in the system?**
- 4) What were the mechanisms driving fluid flow?**
- 5) What were the mechanisms and processes involved in metal dissolution, metal transport and metal precipitation?**

In addressing these questions of the system many problems may be conceptualised and tested, and in general there are two types of modelling, 1) conceptual modelling and 2) numerical modelling. The conceptual or 'soft model' involves little quantitative description and aims to interpret the behaviour of the system or process involved. Konikow & Bredehoeft (1992) describe this in relation to a hydrogeological model as "a hypothesis for how a system or process operates". The conceptual model provides us with an initial understanding of the system and the potential processes involved, the numerical modelling provides us with the means to rigorously test and improve this understanding.

The general solution procedure of numerical modelling is shown on Fig. 2.15. Throughout the modelling process, evaluation of results and examination of the model response to inputs is required, as alterations are generally needed in the preliminary stages. As the models progress, inputs may be finely tuned to satisfy the original conceptual model, or may be modified to test new outcomes from the modelling. Sensitivity analysis is always performed throughout this procedure, which enables the user to define critical parameters and potential flaws in the modelling process. This process is an iterative one; testing, validation and identifying key critical parameters serves as a progressive learning tool that sometimes may far exceed the value and outcomes of individual models.

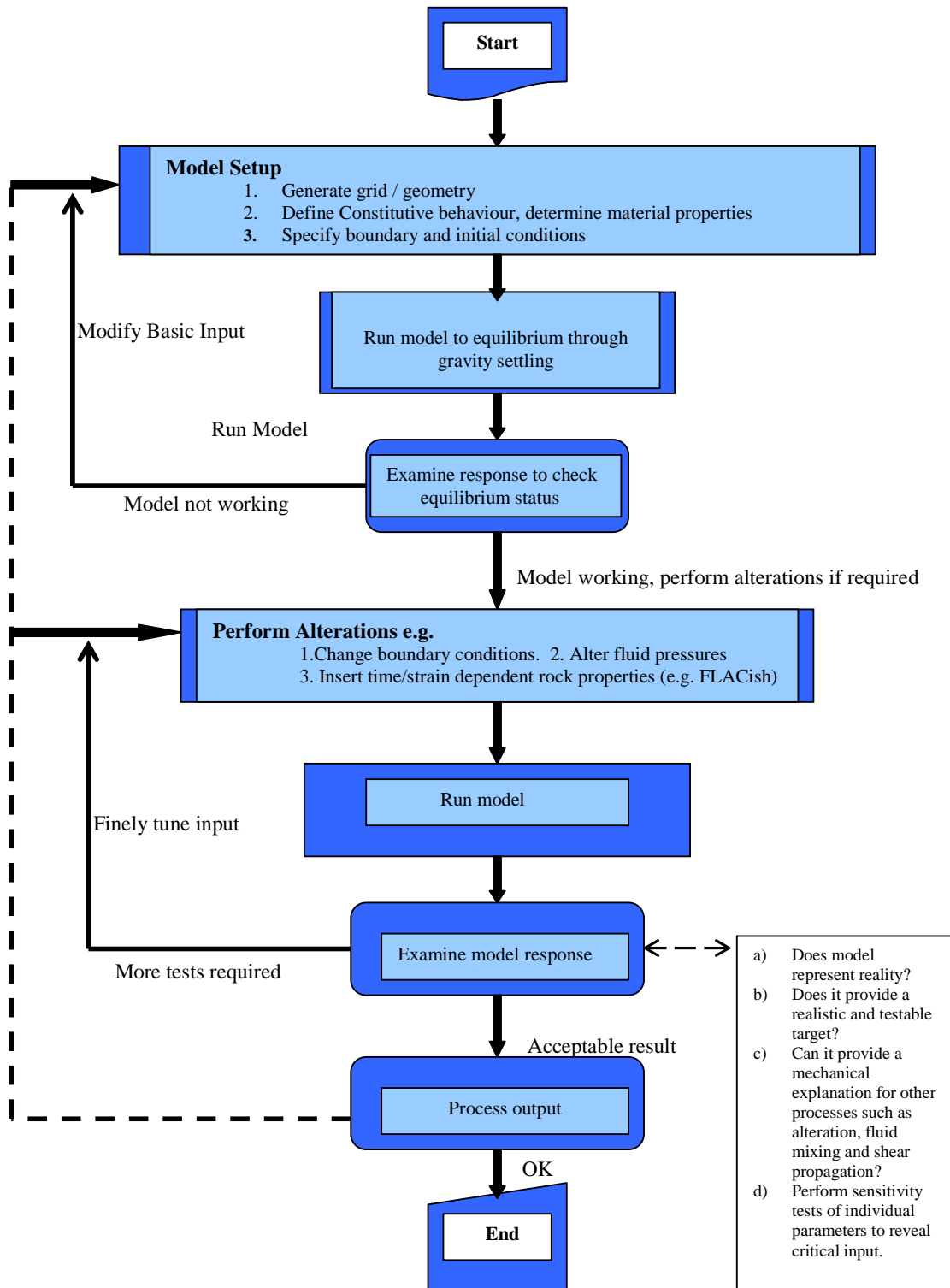


Figure 2.15. General solution procedure for the modelling process of FLAC (adapted from Itasca, 2000a).

## 2.4 Modelling Approaches and Software

This section will present the basic approaches to geomechanical modelling, and highlights differences between different types of software used here, and their applications to geological problems.

### 2.4.1 Continuum and Discontinuum Methods

In geomechanics we can separate the behaviour of deformation into two broad categories, continuous and discontinuous deformation. Continuum modelling methods are suitable for representing porous media flow (as described in section 2.2.4) where a smoothing of physical reality is based on continuum mechanics. There are two basic approaches to dealing with this problem, 1) the differential approach (finite difference) which is based on the analysis of the behaviour of an infinitesimally small element of the continuum, leading to a derivation of a system of governing differential equations, and 2) the integral approach (finite element) in which some physical principles e.g. the conservation of mass and energy, are applied directly to the whole domain through the formulation of governing integral equations (Zhang and Sanderson, 2002). The finite difference method uses an 'explicit' solution scheme, which relates to the nearest neighbour concept or a forward averaging method (Franklin and Dusseault, 1989). The finite element method however, is based on an 'implicit' solution scheme and performs a 'Eulerian' analysis. In the implicit scheme the time-step can be arbitrarily large, but needs to follow an unconditionally stable scheme, and the material deforms relative to a fixed grid. The finite element or implicit scheme is more computationally intensive in solving non-linear problems.

The discontinuous approach to modelling the interfaces or contacts between discrete bodies must take into account two types of mechanical behaviour; 1) behaviour of the discontinuities, and 2) behaviour of the solid material involved. Blocks of material within these models may be assigned rigidity or a deformable property, and the contacts between blocks may also be given a deformable property. The distinct element method (e.g. UDEC), can use a time-marching scheme to solve equations of motion (Zhang and Sanderson, 2002) and the rock mass may be represented as an assembly of discrete blocks that may be internally deformable, with fractures being treated as interfaces between these blocks (Chapter 5).

#### 2.4.2 FLAC (Fast Lagrangian Analysis of Continua)

FLAC is a two-dimensional explicit finite difference modelling program, developed by Dr. Peter Cundall in 1986, and primarily intended for geotechnical and engineering applications (Itasca, 2000a). This software program has been further developed and nurtured (particularly by the computational geoscience group of the CSIRO E&M, Perth, W.A.) to examine many different types of geological problems. The program simulates behaviours of geological materials that undergo plastic flow during yield, and has been applied to many geological problems in Australia (e.g. Ord, 1990,1991a,1991b; Ord & Oliver, 1997; Oliver *et al.*, 2001; Upton *et al.*, 1995, 1998; Upton, 1998; Zhang *et al.*, 1996a,b, 2003; McLellan, 2001; McLellan *et al.*, 2004; Schaub & Zhao, 2002). Materials are represented by zones that form a grid, which can be adjusted by the user to fit the geometry of the problem to be solved. Each zone within the grid can be prescribed properties (both elastic and plastic) and the zones behave according

to a prescribed linear or non-linear stress/strain law as a response to applied forces. The material is allowed to yield and flow and deform whilst run in large-strain mode, and when in a coupled scenario, fluid allows interaction and influence over this deformation. FLAC can be further enhanced by the use of an additional user compiled code called FLACish (FISH), which is designed to enhance the capability of the FLAC program and give greater precision over modelling details. A geological example of this code is described in Chapter 3 and given in Appendix 1.

In designing a geological model, several points must be addressed. The first point to consider is the choice of constitutive model required for representing the material within the model. A number of constitutive models are available in FLAC, however the Mohr-Coulomb model, which has no inherent time dependence, is favoured in this study. In the mechanical calculations the starting state of the model requires an initial in-situ state of stress (as described earlier in this chapter). Applying both vertical and horizontal stress to the model attempts to reproduce this initial state. The vertical stress is applied by the simple function of  $(\rho gh)$ , the horizontal stress however, is more complex and difficult to estimate as it relates to the tectonic history. The simplest approach is therefore to apply all stresses as equal, and check the model state and run to equilibrium until velocities are comparably small. During the modelling procedure we need to know if the model is in equilibrium. This involves examining the maximum unbalanced force, where the value of this force must be a very small percentage of the typical internal forces acting on the model within the grid. If the unbalanced force is considerably large then we have to

look at reducing boundary velocities to prevent the effects of inertia. Velocity boundary conditions are imposed as a length per time step e.g. each time step corresponds to a shortening or extension of the model length. During deformation of the model, plastic volume change, which is influenced by the dilation angle (see Eqn. 2.47), results in dilation and contraction as a result of strain, which influences fluid flow rate and direction. The volume change results in changes in pore pressure, which influences change in effective stress, which can lead to further plastic deformation that feeds back to more volume change. This relationship continues in a coupled manner throughout deformation.

Although there is no time dependence in the mechanical part of FLAC, the fluid flow and creep calculations are based on a time-dependent relationship. The flow time step is calculated to allow time for fluid to move during mechanical steps. Fluid flow time steps are derived from the areas dominated by the greatest permeability, and large variations of permeability within a model may reduce convergence speed. Pore pressure within the model can be initialised at a specific range or by allowing the model to reach equilibrium, i.e. the model can be set at a hydrostatic pore pressure and areas can be initialised at supra-hydrostatic to simulate an overpressured area. Pore pressure can also be fixed as a boundary condition, i.e. the top surface of the model representing the ground surface may be fixed at a pore pressure of zero. As stated earlier in this section the use of FLACish or FISH functions will enhance the setup and running of the model and this allows the user to define more realistic geological scenarios. Examples of FLAC and FISH code can be found in Appendix 1. Disadvantages of FLAC include the inability to deform materials with

complicated geometry to large strains, and this problem usually results in grid failure. Another common problem with this version of FLAC is the restriction of modelling geological materials in 2-dimensions. A 3-dimensional code has been developed, however, it was not available for this study. The user therefore has to make an informed decision on whether the geological problem to be tested would produce adequate results in 2-dimensions.

### 2.4.3 UDEC (Universal Distinct Element Code)

UDEC is a two dimensional numerical program based on the distinct element method for discontinuum modelling (Itasca, 2000b). The code was originally presented by Cundall (1971) and later adapted by Itasca Consulting Group, Inc. in 1985. UDEC enables a numerical simulation of the response of discontinuous media e.g. jointed or fractured rock mass, subjected to either static or dynamic loading. The models are represented by discrete blocks, and the discontinuities represented as boundary conditions between blocks. UDEC allows large displacements and rotation of blocks and discrete blocks can behave as either rigid or deformable material. The discrete blocks are subdivided into a finite difference mesh and each zone or element within the mesh behaves according to a prescribed linear or non-linear stress/strain law. The relative motion of the discontinuities is also governed by linear or non-linear force displacement relationship for movement, in both the normal and shear directions. As with FLAC, UDEC has several built-in material behaviour models for both the discrete blocks and the discontinuities. Again, the user defined code FISH is available to enhance the model setup and procedure.

UDEC calculates force and displacement according to Newton's law's of motion. As the force depends on displacement, the force/displacement calculation is done over one time instant. The central difference scheme is 'second order accurate' which is an important characteristic that prevents long-term drift in a distinct element model (Zhang & Sanderson, 2002). Fracture deformability or the response of fractures, in the normal direction, is based on the stress-displacement relationship which is assumed to be linear, and governed by the stiffness properties applied to the fractures. The fractures have a limiting tensile strength and when exceeded failure occurs, similarly in shear the response is controlled by the shear stiffness, and shear stress is limited by a combination of cohesive and frictional strength of the fracture. Dilation of fractures may occur at the onset of slip, and this dilation is governed by a specified dilation angle. Fluid flow is allowed through the fractures by a fully coupled mechanical-hydraulic analysis. Fracture conductivity is dependent on mechanical deformation and, conversely, fluid pressure affects the mechanical behaviour of the fractures. Fluid flow in joints, are modelled as flow between domains, and flow rates can be calculated in two different ways depending on the contact present. In the case of a point-to-edge contact, flow is primarily derived by a pressure gradient ( $p_1 - p_2$ ), however, when an edge-to-edge contact is present flow is calculated by the 'cubic law' (see section 2.2.5) for flow in a planar fracture, which accounts for contact edge lengths. UDEC has been proven as a useful numerical tool in simulating geological processes e.g. Oliver *et al.* (1990; 2001); Mair *et al.* (2000) and in particular for fault arrays and fluid flow (Oliver, 1995; Jiang *et al.*, 1997; Zhang and Sanderson, 2002). The main, and obvious, disadvantage of UDEC is the inability to model porous media flow through

deformable blocks in conjunction with discrete fracture flow. This version of UDEC is limited to modelling geological problems in 2-dimensions only. A 3-dimensional UDEC (3DEC) has been developed, however again this was not available for this study. A more detailed examination of UDEC and several models are presented in Chapter 5.

# **Chapter 3**

## **Fluid flow in extensional environments; numerical modelling with an application to Hamersley iron ores**

**This chapter has been published in 2004**

McLellan, J.G., Oliver, N.H.S. & Schaubs, P.M. (2004) Fluid flow in extensional environments; numerical modelling with an application to Hamersley iron ores. *Journal of Structural Geology*, 26, 6-7, 1157-1171.

Contributions to this published work consists of;

N.H.S. Oliver – normal supervisory contributions

and

P.M. Schaubs – assistance with developing FLAC codes

**Abstract**

*The mechanical feasibility of focusing both surface- and basinal-derived fluids towards sites of iron ore genesis during Proterozoic deformation in the Hamersley Province is tested here by computer simulation. Finite difference modelling of porous media flow during extensional deformation of a mountain range shows that surface fluids are drawn towards areas of failure and focus into the centre of the mountain. The addition of permeable structures such as a normal fault provides focused fluid pathways in which mechanical and geological conditions are particularly conducive to both upward and downward flow. Upward flow from the base of the fault within the model overall, is favoured by low permeability basement materials and supra-hydrostatic pore pressures. Downward migration of fluids becomes more prominent as extension progresses and upward fluid flow from the base diminishes. The introduction of sedimentary layering into the models allows lateral fluid flow, such that sites of potential fluid mixing may then occur within permeable iron formation units close to the fault zone. Allowing parts of the stratigraphy to become more permeable as a function of high fluid flux simulates permeability enhancement by silica dissolution as a mechanism for iron ore genesis. The involvement of both basinal and surficial fluids in the genesis of the ore deposits is supported by the mechanical models and in addition provides an explanation for a progression from relatively reduced to oxidised conditions at the Mt Tom Price deposit (and possibly other large deposits) with time.*

### 3.1 Introduction

Surface fluids have been implicated in subsurface ore forming processes in several geologic environments (e.g. Epithermal – Sillitoe, 1993; Mississippi Valley Type (MVT) – Garven, 1985). Surface fluids moving downwards during sedimentation may become overpressured or underpressured during the burial-compaction-inversion cycle of sedimentary basins and compacting basins can generate abnormal fluid pressures or overpressurised zones (Bethke, 1985; Bredehoeft & Hanshaw, 1968; Kissen, 1978; Neuzil, 1995). Strongly inverted basins with elevated mountain ranges may also be dominated by topographically driven fluid flow (Fig. 3.1). Regional groundwater flow studies with applications to hydrologic, petroleum and mineral systems have been examined previously (e.g. Tóth, 1962; 1963; Freeze & Witherspoon, 1966; Garven & Freeze, 1984a; 1984b; Oliver, 1986; Upton *et al.*, 1995), and these studies recognise the varying effects of topography and deformation in controlling hydraulic head gradients and hence the migration of fluids within the crust. Compaction driven or overpressurised upward flow is a common feature in the generation of hydrocarbon deposits (e.g. Upton *et al.*, 1998) and within sedimentary basins (Bethke, 1985), and has also been related to fault activity (Sibson, 1987; Sibson *et al.*, 1988). Lateral fluid flow is generally influenced by topography and the permeability of geological units, where topographic influences on hydraulic head have been shown to drive fluid in a downward and lateral direction. For example, Tóth (1962; 1963), Garven & Freeze (1984a) and Nesbitt & Muehlenbachs (1989) have interpreted that deep gravity-driven flow has significant implications for large-crustal hydrodynamic processes. For contractional deformation, Oliver (1986) has described the ‘squeegee’ effect of

thrusts enabling considerable lateral fluid flow and the potential for mixing of surficial and deep-seated fluids during this process. Downward migration of fluids has been attributed to underpressure, or as a result of extensional deformation, where vertical interconnectivity of fractures within rocks allows deep penetration of surface fluids (Nesbitt & Muehlenbachs, 1989).

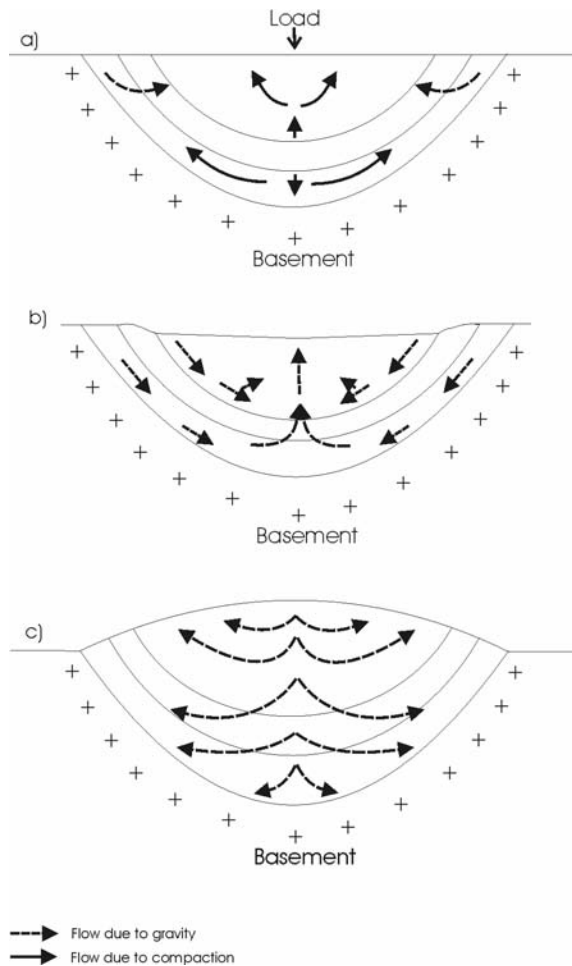


**Figure 3.1.** Hydrological cycle for a) compacting basin b) mature basin and c) topographical system (adapted from Domenico & Schwartz, 1997).

Deformation induced fluid flow has been discussed by several authors (e.g. Sibson, 1975; 1994; Etheridge *et al*, 1983; 1984; Oliver, 1996; 2001; Ord & Oliver, 1997) and this process undoubtedly has great influence over directions and rates of flow. Structurally controlled permeability variations and effective

fluid channeling has been discussed in depth (e.g. Etheridge *et al*, 1983; Cox, 1999) and linked to both small and large-scale deformation processes during regional metamorphism. At conditions  $P_f \approx \sigma_3 + T$  (where  $P_f$  is the fluid pressure,  $\sigma_3$  is the minimum principal stress, and  $T$  is the tensile strength of the rock), rocks are likely to undergo continuous micro-cracking leading to increased permeability, and such deformation can result in a significant interconnected porosity, enhanced permeability and fluid flow. When active faults and shear zones link to form percolation networks, this may provide large-scale flow systems conducive for mineralization. Dilatancy, or volume change, of geological materials due to plastic deformation has been widely discussed in the literature (e.g. Vermeer & de Borst, 1984; Ord, 1991a, Oliver, 1996; Ord & Oliver, 1997; Oliver *et al.*, 2001), where the important associated concept of deformation induced pore volume change influences pore pressure and effective stress, responsible for further deformation. Hence, deformation induced dilatancy facilitates deformation induced fluid flow. Rapid geological processes, such as earthquakes, have been linked to dilatancy and fluid flow around fault zones. Seismic-pumping, with pre-failure dilatancy drawing fluids towards faults and then focused during faulting (Sibson, 1975), and dilatancy pumping, irregularities on fault surfaces acting as valves and pumps during failure (Sibson, 1994), have been proposed as causes of rapid movement of fluids in fault zones.

Sedimentary basins are subjected to several processes known to cause large-scale fluid migration (Garven & Raffensperger, 1997), which include gravity, thermal and chemical buoyancy, compaction, loading, unloading, dilation, and

overpressurisation. Large-scale flow has been linked to many types of ore deposits e.g. Mississippi Valley Type (MVT) deposits, and fluid modelling has shown that flow can be as great as  $1 - 10 \text{ m yr}^{-1}$  when associated with topographic driven flow in a foreland basin (Garven & Raffensperger, 1997). Within these low temperature environments the process of fluid mixing has been proposed for many different types of ore deposits (e.g. Kendrick *et al.*, 2002a; Kendrick *et al.*, 2002b; Sharpe & Gemmell, 2002), and in some circumstances evidence of downward meteoric water incursion has been linked to later oxidising stages of ore formation. However, the nature of fluid flow that may allow localisation of ore deposits is thought to be primarily controlled by the permeability and porosity of the rocks, rather than by deformation driven permeability. Dissolution and cementation are two processes that can alter the permeability of any given rock, fracture or vein. The process of dissolution allows increased fluid flux and hence increasing fluid pathways and the potential to carry dissolved metals, which are of great concern in forming ore deposits, excellent examples being carbonate-hosted MVT deposits.

The basic theory of fluid flow has been realised since Hubbert (1940), although the patterns of flow within porous media can change dramatically as a result of hydraulic head, pressure, structure, heat and mineralogical variations. Numerical models of fluid flow at depth have been utilised for many geological scenarios (e.g. Upton *et al.*, 1998, 1995; Ord & Oliver, 1997; Koons *et al.*, 1998; Upton, 1998; Oliver *et al.*, 1999; 2001; Gow *et al.*, 2002; Ord *et al.*, 2002; Schaub & Zhao, 2002), and have become an important tool for simulating the response of geological materials and fluid flow to deformation. In this paper we

examine the effects of topography, structure, extension and permeability creation on fluid flow within a collapsing mountain range. These modelling scenarios are applied to the structural setting and ore genesis of the Hamersley Province, Western Australia, but in a generic form could be applied to many other extensional environments worldwide, particularly in the 2-8 km depth range of deep sedimentary basins and the shallow parts of orogenic belts. Specifically we attempt to consider the dual effects of both structurally and topographically driven flow, in conjunction with permeability enhancement produced by chemical reactions.

### 3.2 Hamersley Province

The Hamersley Province is located in the southern part of the Pilbara Craton, Western Australia (Fig. 3.2) and covers an area of approximately 40,000 km<sup>2</sup>. It consists of an Archaean granite-greenstone basement overlain by Archaean to Paleo-Proterozoic volcanoclastic-sedimentary packages (Mt. Bruce Supergroup), which are divided into three main groups; Fortescue Group, Hamersley Group and the Turee Creek Group. In the southern part of the province the Hamersley Group hosts some of the world's largest iron ore deposits, Mt Whaleback, Mt. Tom Price and Paraburdoo, which are all mineralogically distinctive in displaying abundant hematite of microplaty and martite varieties with minor goethite. These deposits are hosted mainly in the Dales Gorge Member, which away from ore consists of banded iron formation (BIF) with interbedded shale layers (Trendall & Blockley, 1970; Harmsworth *et al.*, 1990). These microplaty hematite deposits are characterised by extremely high grades (>60% Fe), high porosity (5-50%), and lack of silica. Mt.

Whaleback, the largest deposit in the region, is surrounded by low-medium temperature quartz veins (100 to 300°C fluid inclusion homogenisation temperatures), some of which may be relevant to ore genesis (Brown *et al.*, 2004).

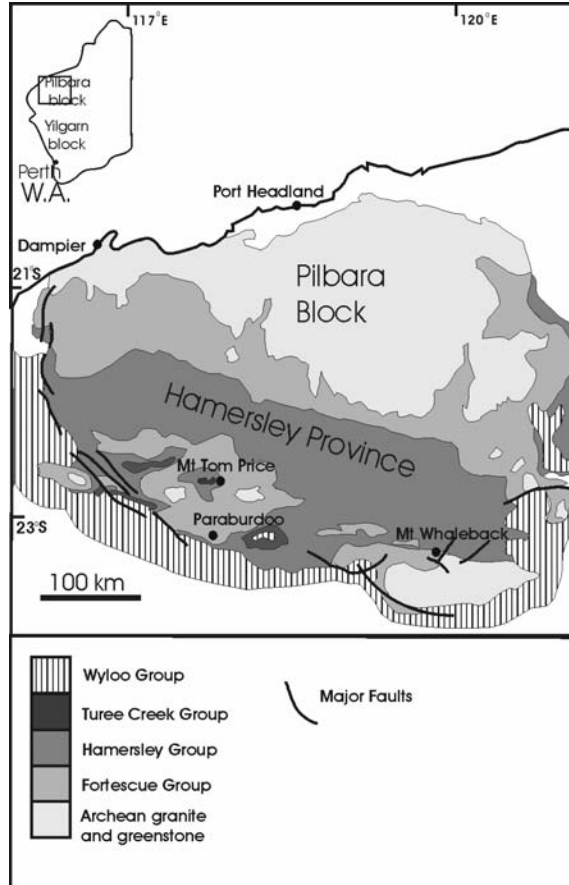


**Figure 3.2.** Simplified regional geological map and summary of stratigraphic groups (modified from Li *et al.* 1993).

### 3.2.1 Structural History

Major structural contrasts can be seen between the northern and southern regions of the Hamersley Province. The northern region is markedly less deformed than the southern region and is characterised by shallow open folds trending north to northwest. More intense deformation occurred in the southern region as a result of the collision between the Yilgarn and Pilbara blocks (Tyler

& Thorne, 1990; Martin et al., 1998), and this is characterised by open folds in the southwest and tighter east-west trending folds in the southeast. The Ophthalmian (ca. 2450 – 2200 Ma) and the Capricorn Orogenies (ca. 1820 – 1650 Ma) are the two main deformational events to have affected the province (Tyler & Thorne, 1990; Powell et al., 1998). The dominant folding event throughout the southern region ( $F_2$ ) is a result of the Ophthalmian Orogeny and this major event was associated with thrusting and shear zone development in the Sylvania Inlier (Tyler, 1991) and overall the region has been interpreted as a fold and thrust belt accompanying development of an inferred Ophthalia mountain range (Fig. 3.3)(Oliver & Dickens, 1999). Extensional collapse of the Ophthalia mountain range after the cessation of the Ophthalmian Orogeny at ca. 2200 Ma involved inversion of thrust faults (Powell et al., 1999), and development of new normal faults. Collectively these normal faults have been implicated as major fluid pathways resulting in ore genesis (Taylor et al., 2001; Oliver & Dickens, 1999; Powell et al., 1999) although absolute timing remains uncertain (2200 Ma versus c. 2000 Ma). Later stage folding ( $F_3$ ) informally known as 'Panhandle folding' along northwest trends is best evidenced in the western part of the Hamersley Province (Taylor et al., 2001), although is not apparent around Mt Whaleback. A fourth compression ( $F_4$ ) known as the Capricorn Orogeny was a significant c. 1800 Ma event that resulted in west to northwest trending, open to upright folds, with up to kilometre scale wavelengths. These are most prominent in the north, central and western areas, and do not significantly affect our model scenarios.

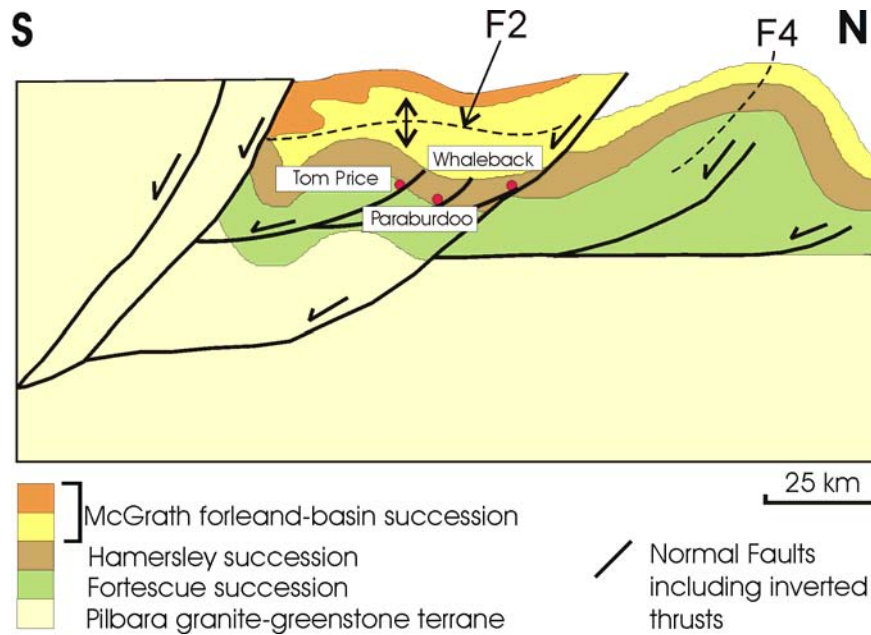


**Figure 3.3.** Simplified regional geological cross section and summary of stratigraphic groups (modified from Powell *et al.* 1999).

### 3.2.2 Ore Genesis Models and Fluid Flow History

Proposed geological models for formation of giant microplaty hematite ores have varied throughout the last two decades, with supergene enrichment followed by metamorphism being the most cited genetic model for high grade hematite ores (Morris, 1980; 1985). This early supergene model (Morris, 1980; 1985) proposed that primary BIF layers (magnetite and chert) were uplifted during the Ophthalmian Orogeny, subsequently exposed to subsurface weathering processes that oxidised magnetite to martite and replaced chert with goethite, and involved electrically conductive BIFs as the main ingredient in a near surface electrochemical cell. Following burial and metamorphism during the Capricorn Orogeny, goethite was then converted to high grade microplaty hematite. This model is now in question for the three microplaty hematite deposits in the Hamersley Province, as evidence of detrital microplaty hematite

clasts found in conglomerates of the lower Wyloo Group (> 2.2 Ga), suggests that ore genesis may have taken place prior to the Capricorn Orogeny (Martin *et al.*, 1998). Li *et al.* (1993) suggested a 'deep hypogene' model which may have involved fluids that equilibrated with underlying basalts. This model proposed the timing of ore enrichment postdates the Ophthalmian Orogeny and may have involved extensional faults as the main fluid pathways. Other recent models include a syntectonic model involving possible fluid mixing (Oliver & Dickens, 1999; Powell *et al.*, 1999; Hagemann *et al.*, 1999) where descending meteoric fluids were responsible for silica loss and oxidization of magnetite to hematite during the Ophthalmian Orogeny and subsequent extension. Most recently Taylor *et al.* (2001) have described a four stage process involving initial upward migration of deep seated basinal fluids followed by downward penetration of surficial fluids, resulting in multistage ore formation. The first hypogene stage involved upward migration of highly saline fluids through the Wittenoom Formation to the lower parts of the Brockman Iron Formation (Taylor *et al.*, 2001). This stage of ore formation removed silica from the BIF units but preserved magnetite. The second stage resulted from the interaction of a moderately warm (c. 100 – 200°C) low salinity oxidising fluid, which converted magnetite-siderite to hematite-ankerite and developed microplaty hematite and martite in the process. A third stage of gangue removal stripped carbonates and silicates from these zones, and finally supergene weathering destroyed minor components such as apatite to complete the ore process.

Within all models two aspects of ore formation are commonly accepted: 1) Ore genesis involved replacement of BIFs and 2) ore bodies are spatially related to

structural features e.g. fault and folds. In the more recent models a broad similarity is present in that isotopic, fluid inclusion, geochemical and structural data suggest both deep seated and surficial (meteoric) fluids were involved in ore genesis, and possible upward and downward penetration of fluids within an extensional environment were important. Thinning of BIF units, silica loss and porosity development accompanied geochemical transitions of BIF to ore (Webb et al., 2003). Ore formation proceeded primarily by silica loss (Taylor et al., 2001; Webb et al., 2003) with accompanying increase in porosity.

### **3.3 Theoretical Background / Mechanical Modelling**

#### **3.3.1 Finite Difference Code**

Models were developed by using the two-dimensional continuum code FLAC v.4.0 (Fast Lagrangian Analysis of Continua; Cundall & Board, 1988), which treats rock masses as continua represented by average values of mechanical and fluid flow properties. Materials are represented by a grid made up of elements or zones, which can be adjusted to fit the geometry to be modelled. Each element is assigned material properties such as bulk modulus, shear modulus and density, and elements deform according to a prescribed linear or non-linear stress/strain law in response to the applied forces or boundary conditions. FLAC uses an explicit time marching solution scheme and a form of dynamic relaxation. Because the solution is by numerical relaxation, and no matrices are formed, large two-dimensional calculations can be made with modest memory requirements. FLAC has the ability to model coupled deformation and fluid flow. Fluid flow obeys Darcy's Law and is considered to be compressible. FLAC-defined permeability and porosity represent initial

conditions, although explicit rules governing permeability can be added. However, most of the hydrodynamic action in the models is a consequence of the change of volume affecting the hydraulic head, induced as a consequence of the deformation of dilatant rock materials.

### 3.3.2 Mechanical Relationships

Applying a suitable constitutive model is the first step in any mechanical modelling study, and the classical Mohr-Coulomb material with non-associated plasticity is most suited to representing the rheology of the mid to upper crust (Veermer & de Borst, 1984; Hobbs *et al.*, 1990; Ord & Oliver, 1997). A Mohr-Coulomb material will deform elastically up to a yield point and then deform in a non-recoverable plastic manner (Ord & Oliver, 1997, Fig.3.). Failure will occur in a material if:

$$|\tau_s| = c - \sigma_n \tan \phi \quad (1)$$

where  $\tau_s$  and  $\sigma_n$  are the shear and normal stresses across arbitrary planes within a material, and  $c$  and  $\phi$  are material constants (cohesion and friction angle respectively). During plastic deformation a Mohr-Coulomb material will shear, and this can be associated with dilation or a volume change. The microstructural processes involved have been highlighted by Vermeer & de Borst (1984), Ord & Oliver (1997), and more recently by Gow *et al.* (2002). During deformation rocks can compact and dilate, therefore dilation can be represented by both positive and negative values of strain:

$$\sin \psi = \varepsilon^P_v / \gamma^P \quad (2)$$

where  $\psi$  is the dilation angle,  $\varepsilon_v^p$  is the rate of plastic volumetric strain, and  $\gamma^p$  is the rate of plastic shear strain. Local positive dilation is crucial in deforming porous media as it typically influences fluid flow direction more abruptly than the gentle gradients associated with topography or broadly distributed strains. For a more comprehensive explanation see Vermeer & de Borst (1984).

### 3.3.3 Fluid Flow Theory

The movement of crustal fluids occurs as a response to head gradients and buoyancy forces. Hydraulic head ( $H$ ) is a measure of mechanical energy per unit weight of fluid, equivalent to the height above an arbitrary datum e.g. sea level, to which fluid will rise in a well. The simplest form of equation describing hydraulic head is an elevation and pressure term:

$$H = z + P/\rho g \quad (3)$$

where  $H$  is the hydraulic head,  $z$  is the elevation above a datum,  $P$  is the pore fluid pressure,  $\rho$  is the density of the fluid, and  $g$  is the acceleration due to gravity. The governing equation determining fluid flow in a porous media can be expressed by Darcy's Law:

$$V_i = k_{ij} \frac{\gamma f}{\eta f} \left( \frac{\partial H}{\partial x_j} \right) \quad (4)$$

where  $V_i$  is the Darcy fluid velocity ( $\text{ms}^{-1}$ ),  $k_{ij}$  is the permeability tensor ( $\text{m}^2$ ),  $\gamma f$  is the specific weight ( $\text{kg m}^{-2} \text{s}^{-2}$ ),  $\eta f$  is the viscosity ( $\text{kg m}^{-1} \text{s}^{-1}$ ) of the fluid,  $H$  is the hydraulic head ( $P/\rho g + z$ ) (m) and  $x_j$  is the position of a material point. Darcy's Law shows that differences in hydraulic head are required for flow to occur, and a static homogenous rock package with topographic relief displays classical Darcian flow as a result of these head gradients. Darcy fluid flow vectors are by

definition orthogonal to contours of hydraulic head in an isotropic medium with a constant density.

#### 3.3.4 Deformation and Fluid Flow Coupling

In a fluid saturated porous media that is deforming, effective stress is generally changing. Instantaneous changes in pore pressure (and hence effective stress) will result from local changes in total stress, but fluid flow is not instantaneous as it is governed by Darcy's Law. The fluid accommodates these changes in total stress, and the system responds by outward flow from regions of high or increased total stress, with the material deforming elastically and plastically as the fluid migrates away. In elastic and Mohr-Coulomb materials the constitutive relationships have no intrinsic time-dependence during such deformation. Our structural analysis relies on a 'poro-plasticity' model, and hence fluid will focus in areas of failure (at yield in shear or tension) within the model. Our models do not explicitly calculate the variation of porosity and permeability at each step during the model cycle. Rather, the material properties (including dilation angle), when subjected to stress, influence an 'elasto-plastic' volume change. This is related to and influenced by pore pressure at that point, and the implicit link to flow is via the pore pressure and hydraulic head (gravitational) parts of Darcy's Law. Thus there is a 'pseudo'-porosity change at each step, which is manifest in the numerical calculations as a volume change (+ve or -ve dilation). This differs from models in which fluid pressure changes are purely a 'poro-elastic' response to applied stress. Effective stress is thus not an imposed variable, but one which is calculated for every step in every zone within the model during its cycle.

The emphasis of previous work (e.g. Ge & Garven, 1992) has been focused on the elastic part of stress-strain behaviour (the poro-elastic effect) and has concentrated on the generation of regions of high pore pressures due to elastic decrease in total volume by an imposed stress. This typically results in fluid being “squeezed” out of the stressed regions. In contrast, in poro-plastic models high strain typically causes positive dilation of rocks and pore pressure decrease, and hence fluid is drawn in. Changes in volume due to plastic deformation are governed by the dilation angle of the rocks ( $\psi$ ), and these changes in volume result in changes in pore pressure (Ord, 1991; Ord & Oliver, 1997). This effect on pore pressure is linked to changes in hydraulic head, which drives fluid flow, in accordance with Darcy’s Law. Therefore, volume change is related to changes in effective stress, which can lead to further plastic deformation, which feeds back to more volume change. This feedback between deformation and fluid flow continues in a coupled manner.

### **3.4. Boundary Conditions and Model Parameters**

#### **3.4.1 General Conditions**

Boundary conditions of the models are such that they represent upper-crustal conditions and are appropriate to deformation of an inverted sedimentary basin during inversion. Initial pore pressure gradients are equivalent to fully saturated hydrostatic conditions, with atmospheric pressure applied to the top of the model and 40 MPa at the base, consistent with the 4 km depth of the base of the mountain range and assuming homogeneous fluid density of 1000 kg/m<sup>3</sup>. Later models incorporating basement material have a supra-hydrostatic starting pore pressure within such material. While rocks may not be saturated at depth,

this assumption equates with the concept of fluid migration through networks of hydrofractures at scales finer than the grid zone dimensions (Ord & Oliver, 1997). Fluid pressure is specified in relation to depth and pressure at the base and sides of the model, at the start of the model runs; it subsequently wanes overall during extensional deformation. Each model is run and allowed to reach equilibrium under gravity before external deformation is applied. The models are subject to lateral extension and deformed to approx. 10% total strain. The base of the model is fixed vertically, but is free to extend in the horizontal direction. The sides of the model have a fixed horizontal velocity and remain planar, but are free to move in the vertical direction. The top surface is free to deform in any manner (Fig. 3.4).

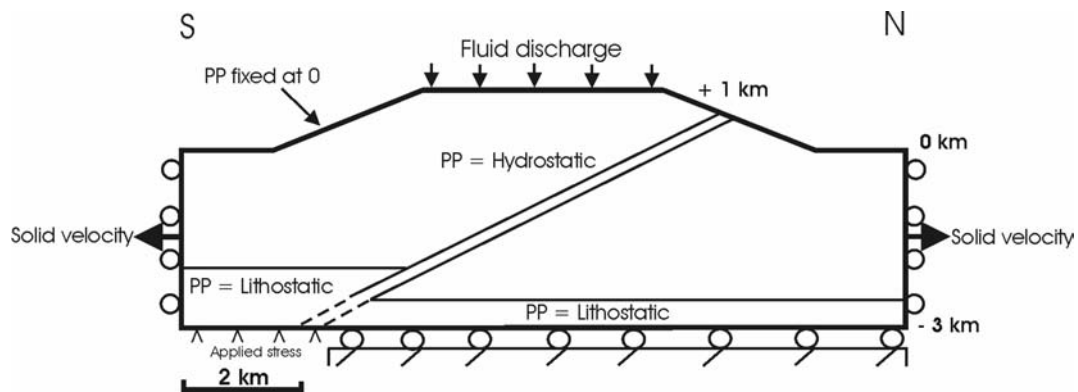


**Figure 3.4.** Mechanical boundary conditions for all models. The geometry is progressively altered throughout the models but basic conditions remains constant. Rolling boundaries allow extension or contraction but edges remain planar. Initial pore pressure conditions are hydrostatic but allowed to change on all boundaries during deformation. A stress equal to the overburden is applied at the base of the hangingwall, which allows normal sense movement on the fault during extension but prevents the base of the model from collapsing. Pore pressure is fixed at zero at the top of the model, hydrostatic initially in most of the models throughout the mountain range, and lithostatic initially at the base of some models. Fluid is applied to the top of the model at a rate of  $1e-10 \text{ ms}^{-1}$  simulating rainfall.

Material properties for all models discussed in this paper are listed in Table 3.1, which are representative of upper crustal materials and are in accordance with values proposed by previous authors (e.g. Ord & Oliver, 1997; Upton, 1998;

Gow *et al.*, 2002). Input parameters were varied during sensitivity testing, and variations included dilation angle (between 1-5°), permeability (2 orders of magnitude), cohesion, shear modulus, pore pressure (lithostatic-hydrostatic), bulk modulus and rates of deformation. Bulk modulus, dilation angle and deformation rates were the parameters least sensitive to change. In order to ensure that normal displacement occurred across the fault zone, cohesion and shear strength were specified at  $2.00 \times 10^2$  Pa and  $3.00 \times 10^7$  Pa respectively (Table 3.1) for the fault zone material, 2 to 4 orders of magnitude lower than the surrounding materials.

**Table 3.1.** Material properties for numerical models

Model	Density (kg/m <sup>3</sup> )	Bulk modulus (Pa)	Shear modulus (Pa)	Cohesion (Pa)	Friction angle (°)	Dilation angle (°)	Permeability (m <sup>2</sup> )
<b>Models 1-5</b>							
Upper crust	2700	2.33e10	6.4e9	1.0e7	30	3	1.0e-15
Fault	2400	2.33e8	3.0e7	2.0e2	30	4	1.0e-13
Granite	2650	4.95e10	2.9e10	4.0e6	30	3	2.0e-16
BIF	2800	3.2e10	4.0e9	3.0e6	30	4	1.0e-14
Shale	2500	2.81e10	6.69e9	3.0e6	30	4	1.0e-19
<b>Model 6</b>							
Upper crust	2700	2.33e10	6.4e9	1.0e7	30	3	1.0e-15
Fault	2400	2.33e8	3.0e7	2.0e2	30	4	1.0e-13
Granite	2650	4.95e10	2.9e10	4.0e6	30	3	2.0e-16
BIF	2800	3.2e10	4.0e9	3.0e6	30	4	* 1.0e-14 to 1.0e-12
Shale	2500	2.81e10	6.69e9	3.0e6	30	4	1.0e-19

\* Reaction enhanced permeability function applied

Simple conceptual models were devised to individually determine the effect of topography, extension and simple structures on fluid flow, and relate this to extensional collapse of mountain belts. The models are comprised of 120 x 60 grid zones and represent a section of upper crustal material initially 12 km wide and 3 km deep, with an additional topography 1 km high in the centre of the model (corresponding to a mountain range). Four basic variations (Models 1, 2, 3 and 4)(Fig. 3.5) are: 1) mountain range without deformation, 2) mountain range undergoing extension, 3) mountain range extension with a permeable

shear zone (inverted thrusts), and 4) effect of low permeability basement material.

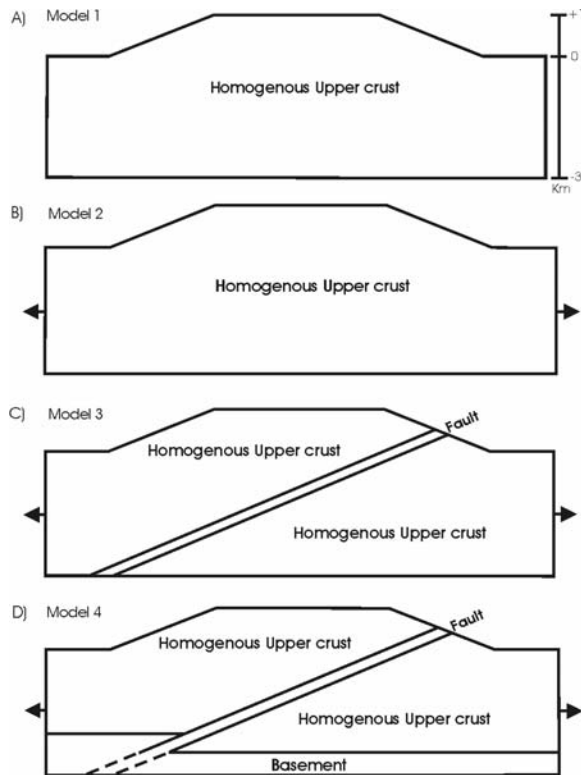


**Figure 3.5.** Starting conditions for four basic conceptual models 1) mountain range without deformation, 2) mountain range undergoing extension, 3) normal sense reactivation of former thrust faults, and 4) basement impermeable block and collapse of basement thrust. Note: vertical scale = horizontal scale.

### 3.4.2 Hamersley Specific Models

Based especially on the Hamersley Province, Model 5 consists of a 12 km x 3 km two dimensional block of upper crustal material with additional 1 km of topographic relief (as per Model 1), which represents simplified topographical and geological elements of an inferred mountain range. Additional structures were progressively added to the basic model, including a fault (Model 3), granite basement blocks (Model 4) and stratigraphy (Model 5) (Fig. 3.6). This staged process allowed verification of model parameters and sensitivity testing as the modelling progressed. The constitutive model and boundary conditions are as

for earlier models (1 – 4), with the basement pore pressure initially set as lithostatic.

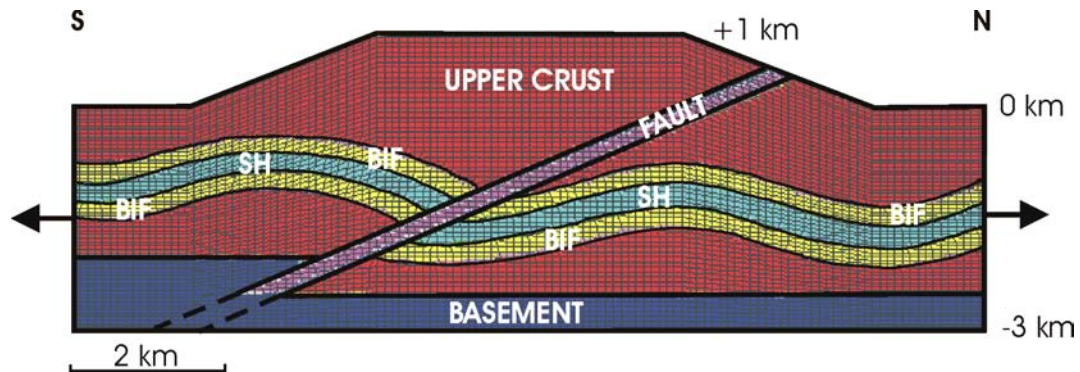


**Figure 3.6.** Conceptual Model 5 consists of a 12 km x 3 km two dimensional block of upper crustal material with additional 1 km of topographic relief, which represents simplified topographical and geological elements of an inferred Ophthalmian mountain range. Additional structures include a fault, a granite basement block, and folded stratigraphy (BIF- banded iron formation, SH- shale).

Model 6 examines the effect of increasing permeability of BIF units, as a proxy for silica dissolution, but could equally well be applied to carbonate dissolution in other environments. The conceptual model is that of Model 5 and model parameters include a variation of permeability considerations with a range from  $2.00 \times 10^{-16} \text{ m}^2$  to  $1.00 \times 10^{-13} \text{ m}^2$  (appropriate to porous and fractured rock), with permeabilities within layered BIF units being allowed to change as a function of fluid flux, through use of an internal macro language (FISH). Six variations of this additional function were applied to the model as a first step in attempting to simulate reaction-enhanced permeability in the BIF layering. As fluid flow within the BIF layers reaches a predefined threshold, permeability is allowed to change incrementally (Fig. 3.7). A limit on permeability increase was

introduced to represent the possibility of compaction, which would inhibit very high porosities (due to overburden load). The mineralogy of the BIF sequences consists of approximately 50% quartz and 50% iron oxide, so an upper porosity limit of the BIF's would therefore be around 50%, irrespective of compaction.

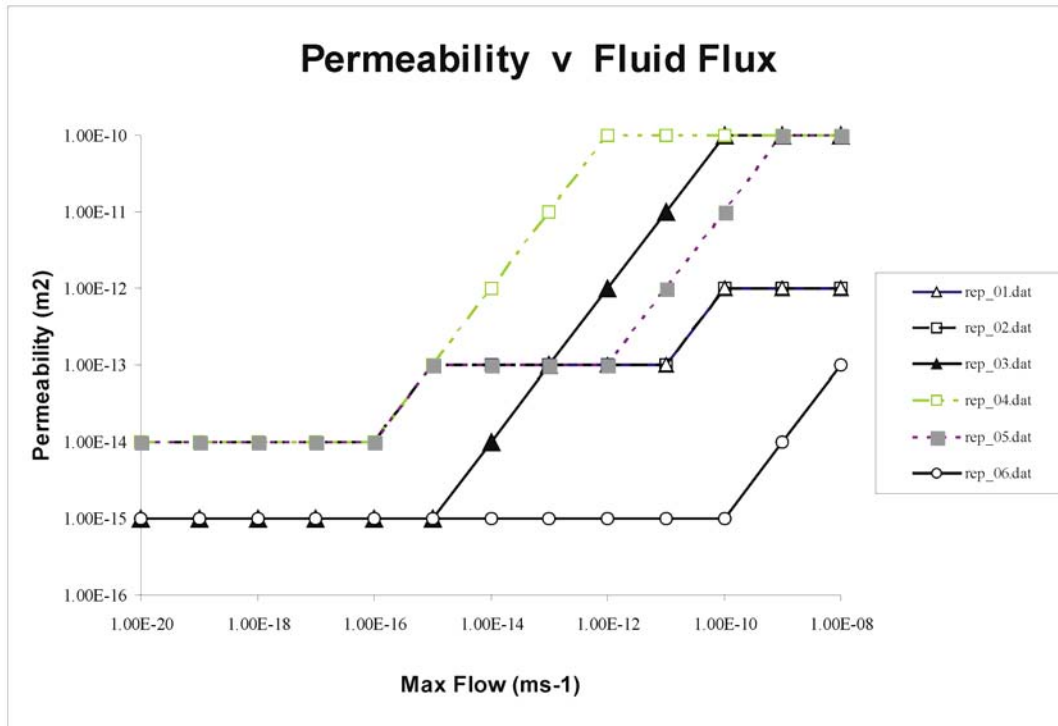


**Figure 3.7.** Six variations of the reaction enhanced permeability function applied using FISH code. This function is applied to BIF layering only. As fluid flow within the BIF layers reaches a certain criteria, permeability is allowed to change incrementally. The plateaux were introduced to represent the potential for compaction, hence a reduction or temporary stasis in permeability within the BIF's. This stasis also provides a limit on permeability creation  $\equiv$  total amount of silica in original BIF (c. 50%). Maximum variation in permeability is 1.00 e-15 to 1.00 e-10 m<sup>2</sup>.

Compaction of these units would decrease the overall porosity and actual ores show an average porosity of around 25% (Webb *et al.*, 2003). Sensitivity analysis of the permeability enhancement function was shown to increase the BIF permeability as a result of flux rates (Fig. 3.8a,b). As a result of the sensitivity analysis and the previous discussion on maximum porosity values of the BIF the reaction enhanced code 02 was used in Model 6, which allowed the BIF units to become one order of magnitude more permeable than the fault.

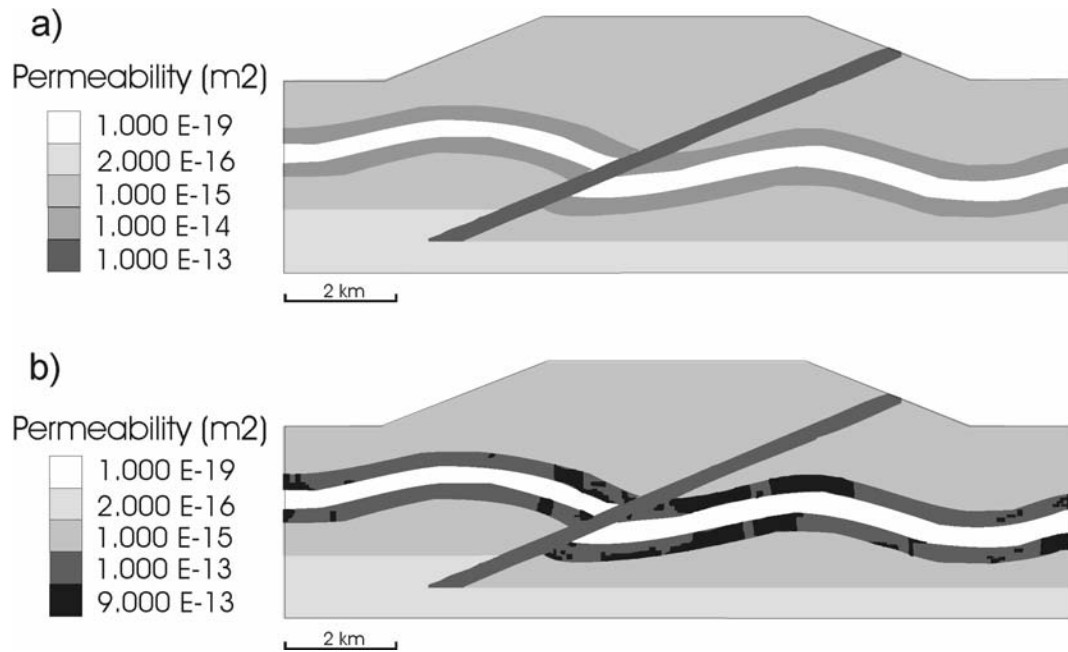


**Figure 3.8.** Two stages of the permeability change in BIF layers. Contours represent values of permeability (darkest colours represent highest permeability). A) starting conditions of permeability, B) permeability increasing along BIF layers to greater than that of the fault. Additional code (rep\_02) was used in this model (see Fig. 3.7).

### 3.5. Model results

#### 3.5.1 Static Mountain Range (Model 1)

The model of a non-deforming mountain range displays classic Darcian flow, where topographic flow is driven by hydraulic head gradients in a ‘fan-shaped’ pattern, with flow generally orthogonal to head gradients (Fig. 3.9). This is in accordance with the typical profile envisaged by hydrologists as previously shown by Hubbert (1940) and Tóth (1962; 1963), and is also consistent with the idea that topographic relief is responsible for much groundwater flow in continental landmasses (Hubbert, 1940; Garven & Ruffensperger, 1997).

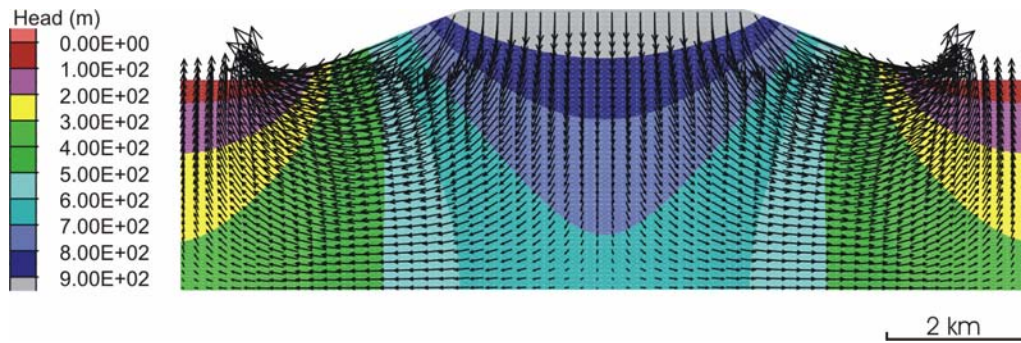


**Figure 3.9.** Model 1 with topography but no deformation. Displaying classic Darcian flow and hydraulic head contours, where topographic flow is driven by head gradients in a ‘fan-shaped’ pattern (e.g. Toth, 1962; 1963). Flow is generally orthogonal to hydraulic head gradients. Arrows indicate Darcy flow vectors, maximum vector is  $1.45 \times 10^{-3} \text{ myr}^{-1}$ . Constitutive Flow Time is  $2.06 \times 10^5 \text{ yrs}$ .

### 3.5.2 Mountain Range Extension (Model 2)

During extensional deformation fluid flow is focused towards areas of dilation and is concentrated towards the centre of the mountain range, although topographically driven gradients still have some influence over fluid flow. Pore pressure within the range decreases rapidly with time as a result of deformation, which drives fluid flow into the centre and base of the model where the decrease in pore pressure is most notable (Fig. 3.10). Variation in rates of deformation were tested and the major flow pattern within the models still displayed downward migration of fluids, albeit less prominent in slowly deforming systems. Collapse of strongly inverted basins or mountainous fold and thrust belts during extensional deformation has a major effect on fluid flow, relative to the ‘fan-shaped’ topographically driven flow as shown within a static mountain range.

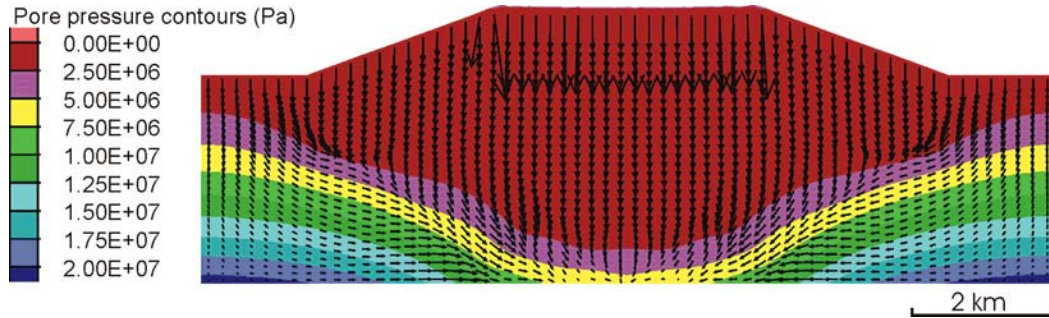


**Figure 3.10.** Model 2 at 3% deformation. Pore pressure decrease is noted in the centre and base of the model, which is driving fluid flow towards these areas. As a result of extension fluid is focused towards dilational areas and into the centre of the mountain range. Arrows indicate Darcy flow vectors, maximum vector is  $1.01 \times 10^{-2} \text{ myr}^{-1}$ .

### 3.5.3 Mountain Range Extension with Shear Zone (Model 3)

Addition of a structure such as a permeable fault or shear zone has a major influence on the fluid flow within a collapsing mountain range. In continuum codes such as FLAC, such zones must have a finite width, and have been set at 2 zones wide ( $\approx 200 \text{ m}$ ). Limitations on the geometry construction prevent using narrower fault zones for adequate display purposes. The addition of a permeable fault provides a primary fluid pathway and fluid is focused into and along the fault zone. High permeability and dilation within the fault allows the downward migration of surficial fluids, which is driven by topography and hydraulic head gradients. Pore pressure gradients and the evolution of pore pressure due to deformation (Fig. 3.11a) drives upward flow from the base of the fault, as local areas of contraction and high shear strain expel fluids. These areas of fluid expulsion are associated with low hydraulic head and negative volumetric strain (Fig. 3.11b). There is competition between upward and downward flow through time, so as the model progresses and extension

matures, downward flow becomes more prominent due to a decrease in hydraulic head and an overall decrease in pore pressure throughout the model with time. Topographic driven flow utilises the least restrictive pathway of the fault and this is in competition with pressure-driven flow from near the base of the model.

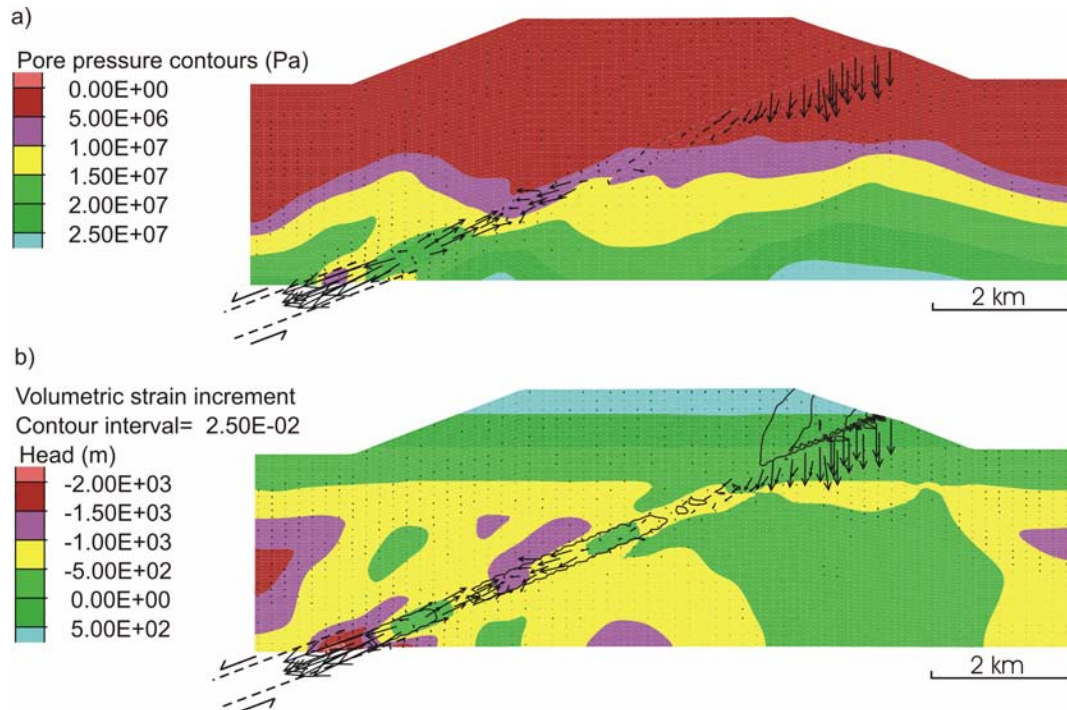


**Figure 3.11.** Model 3 at 3% deformation a) Pore pressure variations showing an overall pore pressure decay displayed within the model with areas of increased pore pressure evident within the fault zone, which is forcing fluids from these areas, and b) volumetric strain increment contours and hydraulic head showing low values within contractional areas of the fault zone corresponding to fluid expulsion. Arrows indicate Darcy flow vectors, maximum vector is  $7.6 \times 10^{-1} \text{ myr}^{-1}$ .

### 3.5.4 Low Permeability Basement (Model 4)

Granite blocks were introduced into the model to simulate both basement and overthrust basement blocks. We assume that the granite has a low permeability and that pore pressure near the bottom of sedimentary basins increases due to porosity reduction with depth. The elevated pore pressure and low permeability

has the effect of driving fluid from the basement rocks, and these fluids are focused within the more permeable fault zone (Fig. 3.12a). The effect of an overpressurised basement forces fluids upwards within the fault, which provides a greater resistance to downward migrating fluids than seen in previous models. As observed in Model 3, there is strong competition between upward and downward migration of fluids within the fault zone. As extension continues, pore pressure within the model begins to decrease and this allows surficial fluids to penetrate deeper into the model. Even with the added basement blocks and initially elevated pore pressures in the initial stages of these models, surficial penetrating fluids overcome this and dominate the overall direction of fluid flow within the model as deformation continues and pore pressures decrease (Fig. 3.12b).

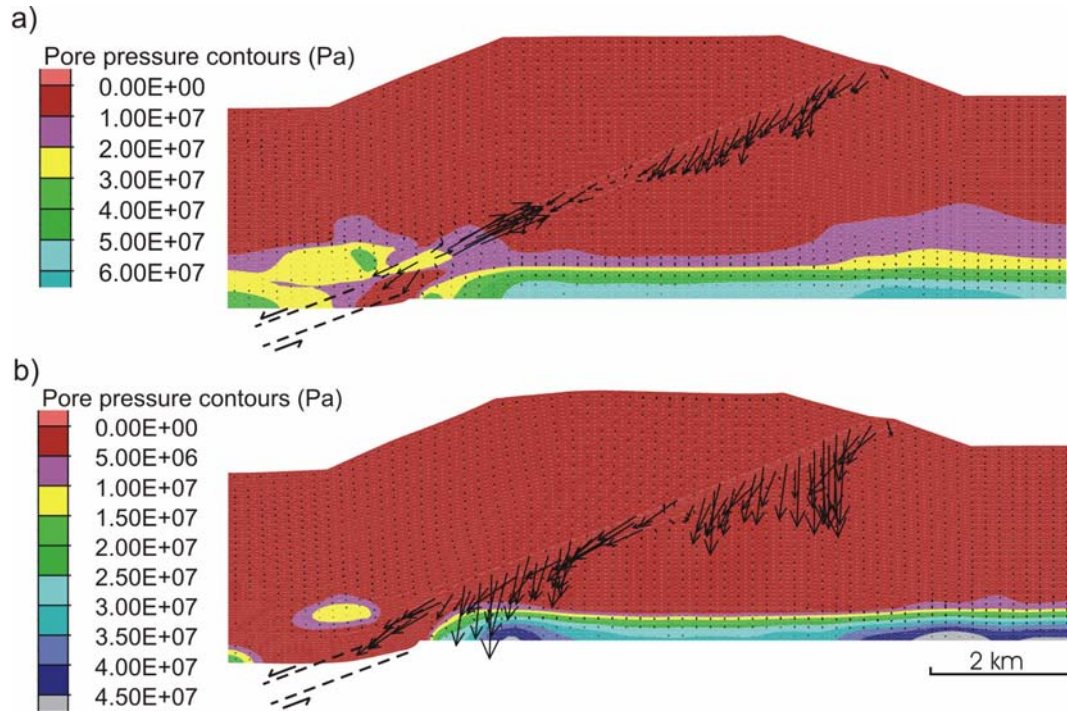


**Figure 3.12.** Model 4 a) at 3% deformation, displaying reducing pore pressures within the model as extension progresses, and showing upward and downward fluid flow within the fault zone. Arrows indicate Darcy flow vectors, maximum vector is  $3.9 \times 10^{-1} \text{ myr}^{-1}$  and b) at 7% deformation, displaying further pore pressure reduction and downward prominent flow, as surficial fluids compete with deep seated fluids. Arrows indicate Darcy flow vectors, maximum vector is  $4.01 \times 10^{-1} \text{ myr}^{-1}$ .

### 3.5.5 Application to the Hamersley Province (Model 5)

One of the most important results from these numerical models is the simulation of upward and downward migration of fluids during extension. At early stages of deformation, upward flow from the base of the model is apparent (Fig. 3.13a) and this can be attributed to variations in pore pressure, hydraulic head and volumetric changes due to deformation as discussed for previous models. The introduction of stratigraphic layering allows lateral fluid flow within the model and fluids enter the BIF units from the more permeable fault where areas of potential fluid mixing are noted at the fault and BIF boundaries (Fig. 3.13b).

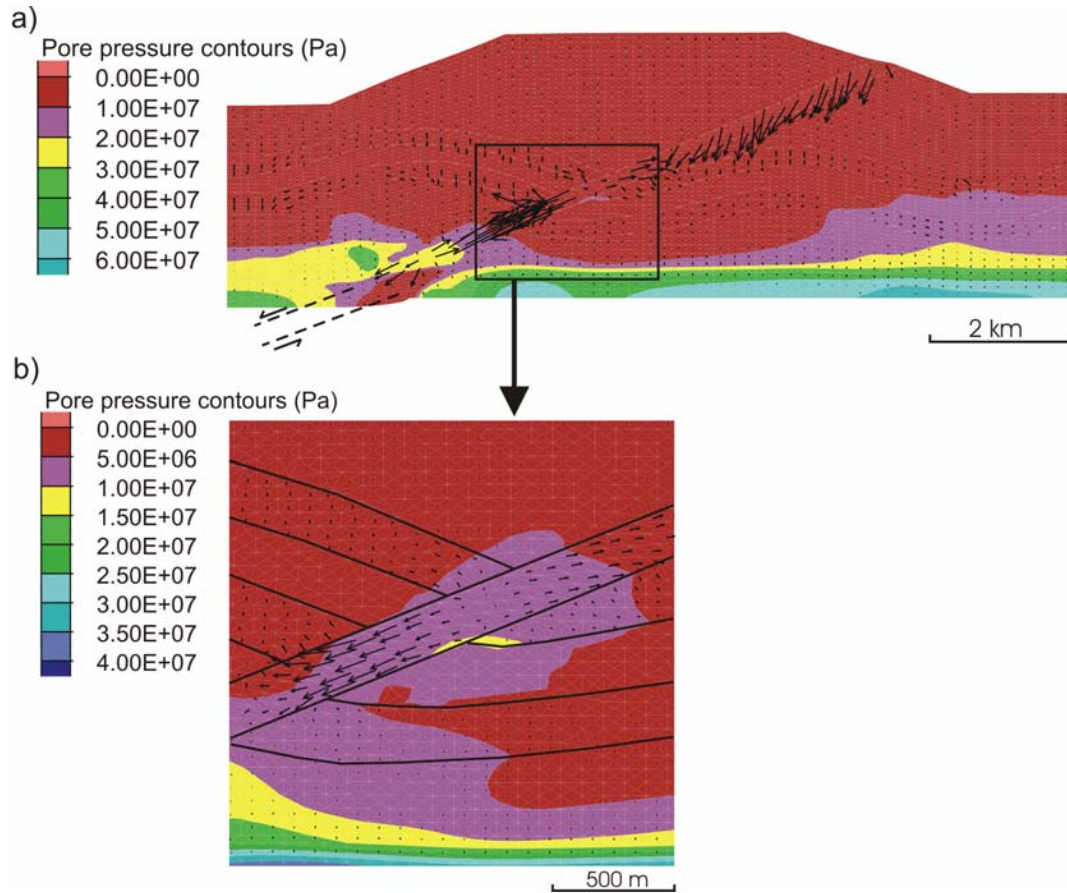


**Figure 3.13.** Model 5 at 3% deformation a) displaying pore pressure reduction with upward and downward migration of fluids and lateral flow within the BIF layers. Areas of high pore pressure within the fault expel fluids, arrows indicate Darcy flow vectors, maximum vector is  $4.97 \times 10^{-1} \text{ myr}^{-1}$ . and b) pore pressure values and highlighting areas of fluid mixing within the BIF layers.

Displacement within the model shows normal sense movement around the fault consistent with extensional deformation and reactivation of previous thrust faults. As extension progresses, upward flow becomes less prominent, and downward migration of fluids is attributed to deformation induced flow and decrease in pore pressure (Fig. 3.14a). Failure modes within the model (Fig. 3.14b) demonstrate that tensile yield is predominantly seen at shallow depths, shear failure is prominent at depth and along the fault zones. Zones indicated as 'elastic, at yield in past' represent areas where pore pressure has dropped such that the rocks have moved off the tensile or shear failure conditions. These

areas sweep through the model as fluid is channelled towards the fault, and are most prominent in the fault hangingwall.

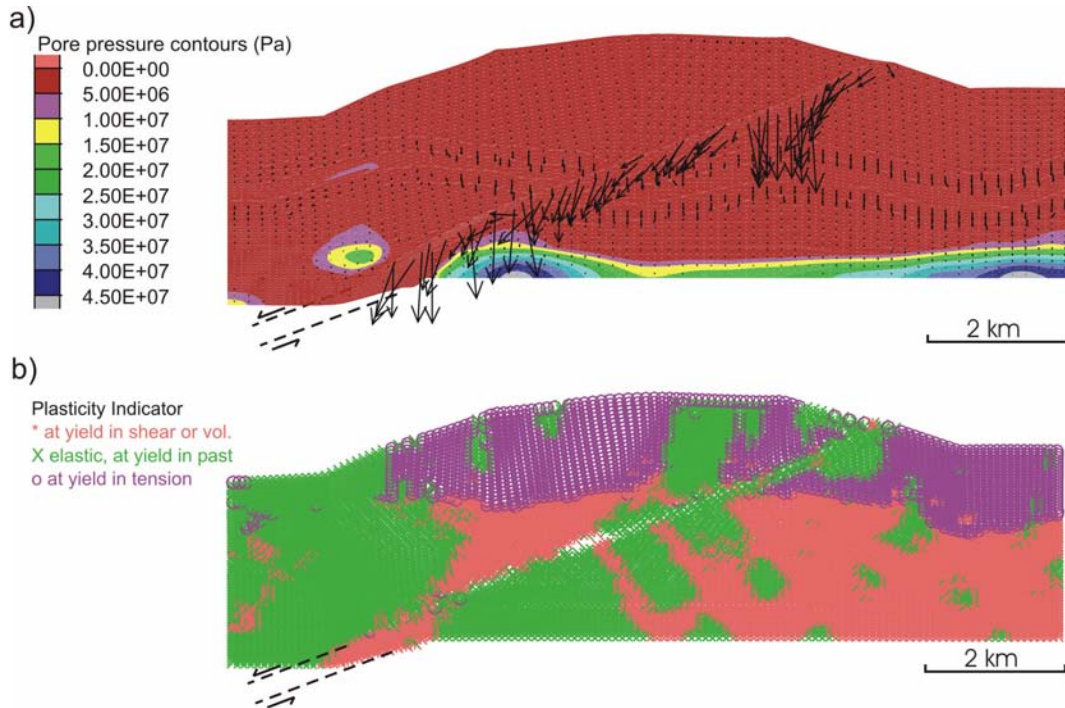


**Figure 3.14.** Model 5 at 10% deformation a) displaying reduced pore pressure within the model due to failure and extension. Downward fluid flow prominent, with lateral flow within the BIF layers. Arrows indicate Darcy flow vectors, maximum vector is  $4.97 \times 10^{-1} \text{ myr}^{-1}$ . b) Plasticity indicator or state of failure of the model, indicating different types of failure within the model. Tensile failure is predominantly shown in the upper half of the model.

### 3.5.6 Silica Dissolution of BIF's (Model 6)

When the reaction enhanced permeability function is applied to the BIF layering in the model, lateral fluid flow is increased along the BIF layers (Fig. 3.15a). Fluid migrates from within the fault zone and enters the BIF layers indicating a high potential for fluid mixing close to the fault and BIF interface (Fig. 3.15b). Fluid flow within the BIF units approaches and exceeds that of the faults due to the dissolution of silica and changes in porosity (up to 50%). As the model

progresses again downward fluid flow becomes more prominent within the fault zone (Fig. 3.16).

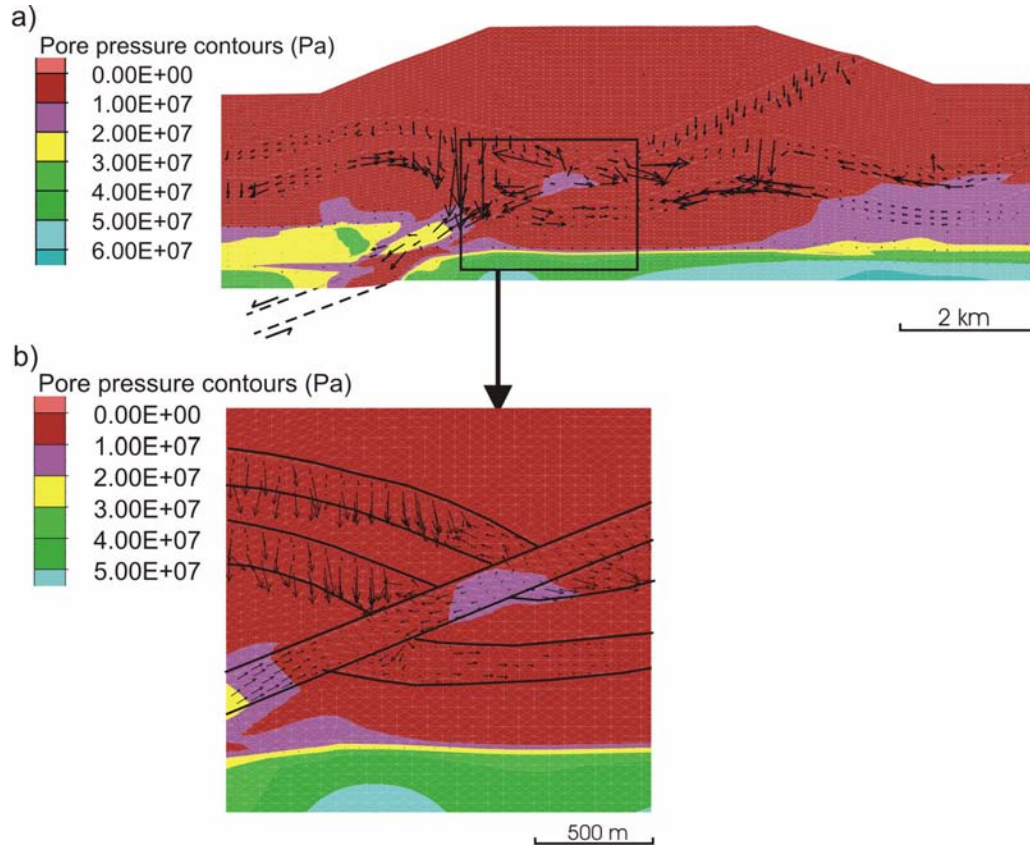


**Figure 3.15.** Model 6 at 3% deformation using (rep\_02) permeability function a) displaying pore pressure values with upward and downward flow within the fault. Notable expulsion of fluid within areas of high pore pressure due to deformation. Lateral flow within the BIF layers is much increased from previous models. Arrows indicate Darcy flow vectors, maximum vector is  $2.44 \text{ myr}^{-1}$ , and b) displaying pore pressure values with fluid migrating from the fault zone into the BIF layers, highlighting potential fluid mixing areas.

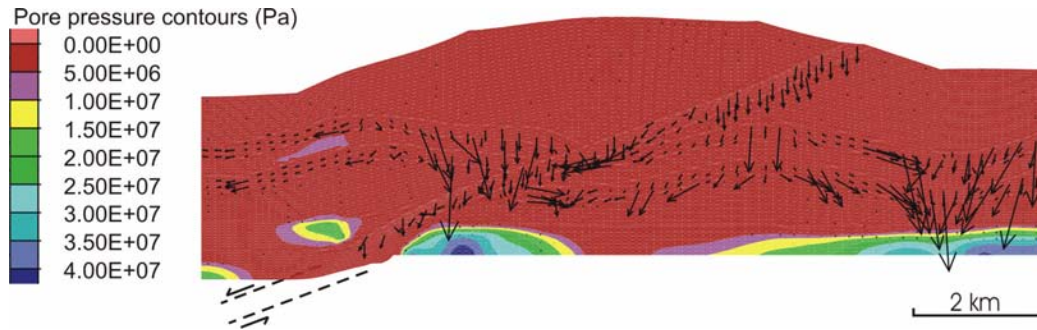


**Figure 3.16.** Model 6 at 10% deformation. Pore pressure values indicating a decrease throughout the model relative to figure 15 and downward fluid flow within the fault is dominant. Strong lateral flow is evident within the BIF layers, arrows indicate Darcy flow vectors, maximum vector is  $2.43 \text{ myr}^{-1}$ .

### 3.6. Discussion and Conclusions

Mechanical and geological conditions appropriate to both upward and downward migration of fluids within a mountain range have been explored within these models. The presence of topography in a basic model demonstrates the strong influence of hydraulic head and topographic driven flow in any homogenous package of rock. However, the effect of extension drives fluid flow into the centre of the model, and even for low strain rates this strongly modifies the flow pattern away from the simple curved topography-only pattern. This effect on fluid flow is due to the focusing of fluid to areas of predicted shear and extensional failure and driven by pore pressure gradients within the model. This competes with the strong effect of topographic driven flow during the early stages of mountain collapse. The addition of a permeable normal fault, (Model 3), causes perturbations to this downward focusing, as the permeability contrasts between the fault and the surrounding rock enables focusing of fluids within the more highly permeable fault. The more permeable fault represents the least restrictive fluid pathway and fluids are drawn from the surrounding package of porous rock into the fault and result in a focused

downward migration of surficial fluids. This flow competes with the upward migration of fluids seen at the base of the models due to deformation and overpressurisation.

During extension there is failure and dilation of the rocks, which focuses flow, and a gradual reduction in pore pressure and hydraulic head gradients as the mountain collapses. As pore pressures drop within the mountain range upward migration of fluids becomes less prominent and downward flow more prominent. The introduction of a granitic basement promotes upward flow due to simulated overpressure commensurate with low basement permeability and compaction related overpressure at the base of the sedimentary sequence. At early stages of extension, deformation-induced flow is evident in the lower parts of the fault, where contraction within the fault zone expels fluid, which coincides with areas of low hydraulic head and negative dilation. However, as the deformation continues and pore pressure decreases overall there is prominent downward penetration of surficial fluids within the fault.

This competing process of upward and downward migration of fluids has major implications for the genesis of the Hamersley iron ores. Ore genesis models of Taylor *et al.* (2001); Hagemann *et al.* (1999); Oliver & Dickens (1999), and Powell *et al.* (1999) are broadly similar in that they have proposed the involvement of both deep seated and surficial (meteoric) fluids. Upward migration of reducing alkaline fluids may have been responsible for the first stage of ore genesis by removing silica, and increasing porosity without altering the oxidation state of the iron rich minerals. This stage has been proposed for

the Tom Price deposit (Taylor *et al.* 2001), with a reduction of silica volume and no oxidation of magnetite to hematite. The second stage of ore genesis involved downward migration of surficial fluids that have converted magnetite-siderite to hematite-ankerite assemblages, developing the characteristic microplaty hematite and martite. Taylor *et al.*, (2001) have proposed a third stage following oxidation, which removed all carbonate from hematite and magnetite rich zones and a final deep supergene stage that converted magnesium silicates to a kaolinitic residue. These last two stages would require prominent downward migration of oxidising fluids during the later stages of extension, which is supported by this modelling. At Mt Whaleback, where Webb *et al.* (2003) have not been able to distinguish separate silica loss and oxidation events, the process of downward flow of oxidised fluids may have been more complete than at Tom Price. In relation to our models, the difference could be due to position of these deposits relative to upward and downward flow paths.

Stratigraphic layering within the mountain range allows lateral fluid migration towards the more permeable fault. Our models predict locations within BIF layers where actual mixing would occur, but also the gradual change from deeper seated fluid moving upwards to surface fluid moving downwards. In these models fluid mixing occurs at the stratigraphic and fault boundaries, and zones of fluid mixing penetrate into the BIF layers. In relation to iron ore genesis, this may represent mixing of deep basinal derived fluids and heated meteoric fluids in accordance with models of Oliver & Dickens (1999) and Powell *et al.* (1999). Fluid flow rates within these models are comparable to many other studies (Dipple & Ferry, 1992; Upton *et al.*, 1995; 1998; Ord &

Oliver, 1997; Upton, 1998; Oliver *et al*, 1999), and the introduction of the reaction enhanced permeability allows flux rates to increase by one order of magnitude.

Allowing the permeability of BIF layers to increase as reducing fluids strip silica allows the model system to maintain lateral fluid migration, and is a key aspect of mineralisation. This dissolution of silica provided secondary fluid pathways along stratigraphic layering, which then allowed layer-parallel movement of heated meteoric oxidising fluids culminating in ore genesis. The potential fluid mixing areas within the BIF and close to the fault boundary are the basis for iron ore genesis within these models as they provide conditions that are conducive for dissolution of silica and oxidation of magnetite to hematite in a two stage process. Basement penetrating faults provide highly permeable fluid pathways to draw deep-seated fluids into the system to accommodate dissolution of silica, and connectivity of these pathways to the surface allows passage of surficial fluids to depths of 3 km or greater. Permeable faults, reaction enhanced permeability and lateral fluid migration has played a vital role in the genesis of giant Hamersley iron ores.

## **Chapter 4**

# **Testing the structural and geomechanical processes in the formation of the Century**

## **Zn-Pb-Ag Deposit**

## Acknowledgement of Contributions

**This chapter is intended for future publication (abstract submitted)**

McLellan, J.G., Feltrin, L., Oliver, N.H.S., 2004. Testing the Structural and Geomechanical Processes in the Formation of the Century Zn-Pb-Ag Deposit. *Computers and Geosciences*, xxxx.

Contributions made to this chapter involved:

J. G. McLellan – Geomechanical Modelling

L.Feltrin – 3D Structural Modelling

J. G. McLellan – 50% (p. 87-126), 80% (p. 126-155), 50% (p. 155-159)

L. Feltrin – 50% (p. 87-126), 20% (p.126-155), 50% (p. 155-159)

N.H.S. Oliver – normal supervisory contributions

**Abstract**

*The Century zinc deposit is one of the giant Mesoproterozoic Zn-Pb-Ag deposits of the Northern Australian Zinc Belt. There is substantial controversy regarding the genesis of this deposit. Previous workers proposed a timing for the emplacement of the Century mineralisation as early diagenetic to syn-tectonic. In this work we present one of the first applications of 3D structural modelling combined with coupled mechanical and fluid flow modelling which aims to address ore genesis using computer simulation techniques. This approach has revealed the benefit of using software such as GoCad as a data integration platform and FLAC as a process modelling tool. We have characterised the structural controls, ore distribution and thickness variations across the half-graben, which hosts the mineralisation. From this analysis we have been able to predict the location of damage zones resulting from syn- to post-Isan Orogeny wrench style deformation, allowing also the distinction of early syn-sedimentary growth faults. 3D modelling has established overprinting relationships between temporally distinct hydrothermal events, and suggests a multistage evolution for this system. Fluid flow modelling using FLAC, was aimed to test the control of permeability and deformation on subsurface fluid flow, i.e. a diagenetic or epigenetic model for fluid migration leading to mineralisation. However, this modelling shows that subsurface fluid flow through the mineralised shales was very unlikely to have occurred in preference to flow through faults and sandstones. Accordingly, both the spatial GoCad and FLAC modelling suggests that a subsurface replacive origin for the mineralisation is less likely than a syngenetic model.*

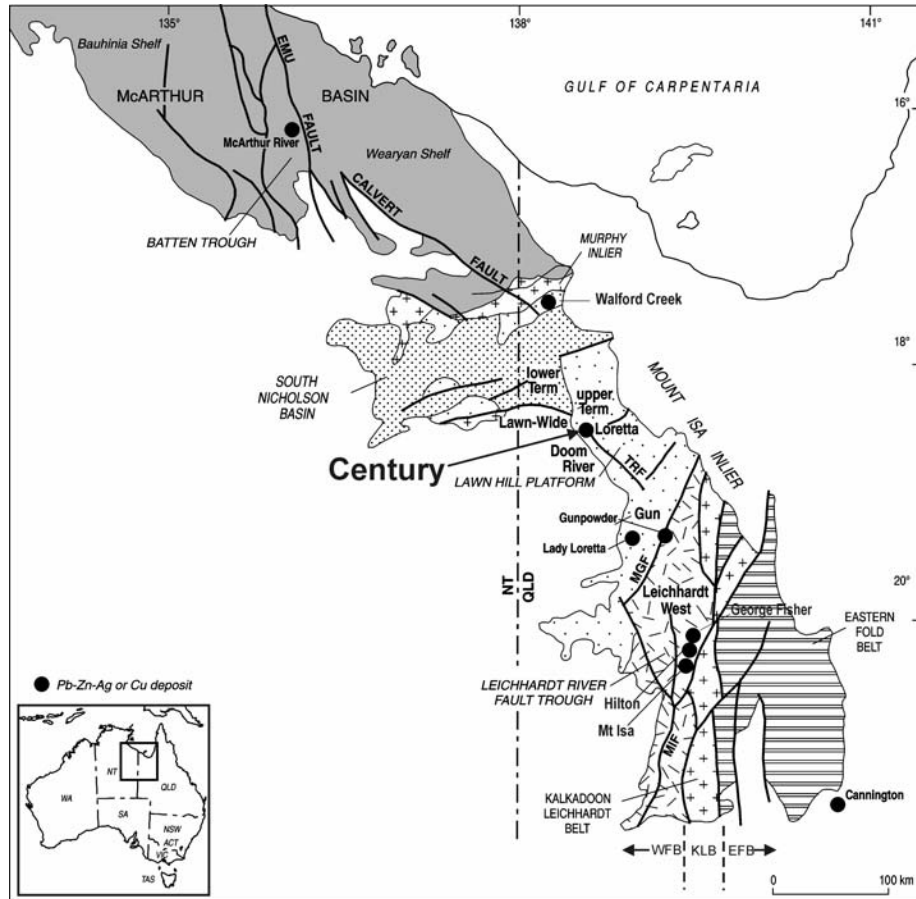
## 4.1 Introduction

Plate tectonics has been recognised as a primary control on the nature and location of mineral deposits in the earth's crust. For example, Sawkins (1990) describes how different classes of metal deposits occur at specific locations of continental and oceanic margins. The relative abundance of metals and size of these occurrences depend on the tectonic context in which a mineral deposit forms as a direct function of the structural architecture, chemical composition of the crust, and type of mechanisms that allow the transfer of mineralising brines to produce economic grade mineralisation.

If we focus on shale-hosted Zn-Pb sulphide deposits (definition from Large 1980; Sangster 1983), we note that favourable present day sites for sulphide deposition are divergent plate boundary environments (e.g. median valley of the Red Sea; Degens & Ross 1969; Hackett & Bischoff 1973). This is in agreement with ore genetic models that invoke anomalous geothermal gradients as a key driving force for focussing metal bearing fluids along crustal discontinuities, leading to ore deposition in rift dominated settings (Russell 1978; Goodfellow 1993). In contrast, Zn-Pb deposits in the broader sense are not exclusive of extensional settings, as several other varieties also occur during contraction (e.g., Garven 1985; Oliver 1986; Duane & de Wit, 1988; Bradley & Leach, 2003).

Moreover, when giant accumulations of Zn-Pb are found in complexly deformed terrains (which record both extensional and compressional tectonic regimes), identifying the most favourable scenario for ore deposition becomes

complicated. This issue is well known within the Northern Australian Zinc Belt (Fig. 4.1), where many Zn-Pb occurrences (e.g. McArthur River, Mount Isa, George Fisher, Lady Loretta, Walford Creek and Century) are notable for their contentious genetic models.



**Figure 4.1** Location map of the Century deposit and the major subdivisions of the Mount Isa Block and the Northern Australian Zinc Belt. The Mount Isa Block is subdivided into the main tectonic units of the Western Fold belt (WFB), Kalkadoon Liechhardt Belt (KLB) and the Eastern Fold Belt (EFB). Major deposits (principally Zn-Pb-Ag) are shown and the Century deposit is highlighted in the Lawn Hill Platform (modified from Southgate *et al.*, 2000).

A general method used to define the tectonic setting responsible for ore deposition, in the Mt Isa Block Zn-Pb deposits, has been to attempt to identify the relative timing of emplacement of massive sulphides with respect to the main stages of Mesoproterozoic rifting, and to the Isan Orogeny (Fig 4.2). Using paragenetic, structural, and geochemical constraints, previous authors

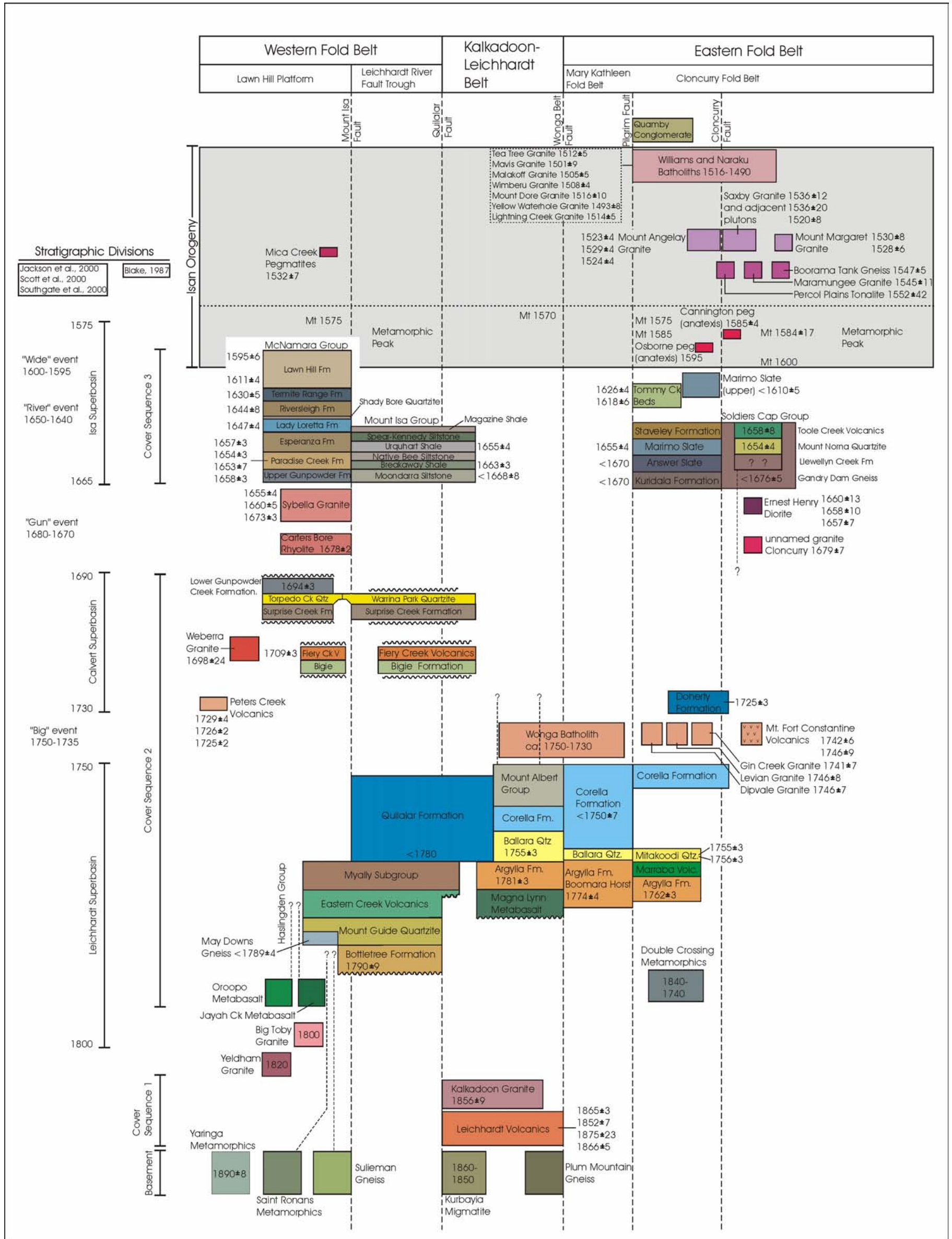


**Figure 4.2** Chronostratigraphy for the Mount Isa Block after Foster (2003). Modified from the compilations of Blake (1987), Blake and Stewart (1992), Page and Sun (1998), Page and Sweet (1998), and Page et al. (2000). Following Blake (1987), the stratigraphy is divided into 3 cover sequences, and divisions into the Leichhardt, Calvert and Isan supersequences and delineation of the "Big", "Gun", "River" and "Wide" events are after Jackson et al. (2000), Scott et al. (2000), and Southgate et al. (2000). Age determinations for the stratigraphic units or intrusions are U-Pb zircon (mostly via SHRIMP) determinations, with exception of the pegmatites at Osborne (U-Pb titanite) and anatexis at Cannington (SHRIMP U-Pb monazite). Metamorphic ages (Mt) include U-Pb zircon and monazite (SHRIMP), and Sm-Nd garnet determinations. Detrital ages obtained from zircon constrain only the maximum possible age for the unit and are indicated by '<' at the front of the age.

have recently proposed different ore genetic models with syn-diagenetic timing for the George Fisher deposit (Chapman, 2004), syn-tectonic timing for the Mount Isa deposit (Davis, 2004), and syn-genetic timing for the McArthur River deposit (Ireland *et al.*, 2004). It is clear that ore genetic controversies are still strong and may suggest:

- a) That all these genetic models depict viable ore forming processes as Garven *et al.* (2001) proposes, and that a protracted hydrothermal evolution may have progressively accounted for the present metallogenic scenario within the Western Fold Belt (Sun *et al.*, 1994), hence each deposit could have formed differently.
- b) Only one of the above models (syn-sedimentary, syn-diagenetic, syn-tectonic) is valid for all these deposits.
- c) Zn-Pb mineralisation is a result of a multi-stage hydrothermal evolution in which again all the models are viable scenarios, but all the deposits experienced a common hydrothermal history (i.e. remobilization).

Some of the issues affecting these types of studies based on relative timing are:

- 1) Poor available constraints on the age of the Isan Orogeny ( 1585 - 1500 Ma) leading in some cases to possible overlap between depositional ages of sediments hosting the mineralisation (Page *et al.* 2000), and deformation ages (Connors and Lister, 1995; Connors & Page 1995). The Isan Orogeny itself has seen different

deformational phases (e.g. Bell, 1983, Bell & Hickey, 1996) and there is some possibility that the metamorphic peak and structural evolution may have been diachronous across the district (compare Rubenach *et al.*, 2001 and Giles & Nutman, 2003 with Oliver, 1995 and Bell & Hickey, 1996).

- 2) Presently accepted models fail to apply exclusively to specific tectonic scenarios, leading to confusion regarding the real ore genetic mechanism. For example, if we clearly identify the evidence for Mississippi Valley Type (MVT) mineralisation, in some cases it is not enough to sustain a contractional scenario for ore deposition. There are examples in the literature of rift-related Mississippi Valley Type Deposits; minor lead deposits found along the Red Sea coast of Egypt (Dadet *et al.*, 1970; El Aref, 1984), and economic Pb-Zn MVT deposits that lie along the axis of the Benue Trough in Nigeria (Farrington 1952; Grant 1971; Akande *et al.*, 1988). After burial and subsequent metamorphism, it would be easy to interpret or mis-interpret these mainly vein-hosted MVT ores as a syn-tectonic product.

Knowing these limitations we have attempted to use newly available computational tools to explore the problem of ore genesis from two new perspectives involving initially, 3D spatial/structural analysis (GoCad), and subsequently, finite difference models of deformation and fluid flow (FLAC) that test one of the proposed ore genetic models for the Century Zn-Pb-Ag deposit.

Here, after a general introduction to the regional and local geology, we focus on the Century deposit considering the main features relevant to ore deposition. Revising and testing proposed ore genetic models, we re-interpret the genesis of Century based on the newly available data. However, the scope of this research also covers evaluation of the capacity of 3D modelling and FLAC modelling to answer ore genesis research questions.

## 4.2 Tectonic Evolution of the Isa Block and Stratigraphic Subdivisions

### 4.2.1 The Mount Isa Block

The Mount Isa Block comprises three broad tectonic units; the Western Fold Belt (WFB), the Kalkadoon Leichhardt Belt (KLB), and the Eastern Fold Belt (EFB) (Fig. 4.1), which are predominantly north-south trending and separated by transcurrent fault zones (O'Dea *et al.* 1997; Blake & Stewart, 1992). Much of northern Australia underwent several periods of extension, leading to the development of intraplate sedimentary basins in which bimodal volcanic rocks and rift-sag sequences accumulated (Etheridge *et al.*, 1987; Etheridge & Wall 1994; O'Dea *et al.*, 1997, Betts *et al.*, 2003). The chronostratigraphic framework of the Mt Isa Block is outlined in Figure 4.2, and within the Mt Isa Block four major Proterozoic sequences are present (Blake, 1987). The oldest rocks, or basement, were first deformed and metamorphosed during the Barramundi Orogeny at approximately 1870 Ma (Etheridge *et al.*, 1987; Etheridge & Wall 1994). Following this orogeny, the Mount Isa terrain underwent a long and complex history of intermittent rifting and deposition, and several Palaeoproterozoic basins evolved between ca. 1800 and 1590 Ma (Carter *et al.*, 1961; Smith 1969; Plumb *et al.*, 1980; Derrick 1982; Blake 1987; Page

1988; Etheridge & Wall 1994; Andrews, 1998; Page *et al.*, 2000; Scott *et al.*, 2000) in the North Australian Craton, which are best preserved and understood in the Mount Isa Block and McArthur Basin. Igneous and sedimentary rocks of this period were formed or deposited during several superimposed intracontinental rifting episodes and associated post-rift subsidence, and designated Cover Sequences 1 to 3 (Blake, 1987) (see Fig. 4.2). Cover Sequence 1 (ca. 1870 – 1840 Ma) is restricted to a narrow central strip (Kalkadoon Leichhardt Belt) and consists predominantly of felsic meta-volcanic rocks. This belt acted as a 'high' and Cover Sequences 2 and 3 subsequently formed on the Eastern and Western sides (Eastern and Western Fold Successions) during separate basin forming events.

Cover Sequence 2 was the result of a period of crustal extension from ca. 1790 – 1740 Ma, with early-syn-rift phase clastic sedimentary and bimodal volcanic rocks deposited in restricted fault controlled basins. These rocks were then overlain by clastic and carbonate sedimentation during a post-rift or sag phase, with termination of this cycle in the Eastern Fold Belt co-incident with the intrusion of the Wonga Batholith at around 1750 Ma (Stewart & Blake, 1992). Basement structures that developed during the deposition of Cover Sequence 2 appear to have had an influence on the depositional characteristics of Cover Sequence 3 (ca. 1670 -1595 Ma), which is best represented in the Western Fold Belt and unconformably overlies Cover Sequence 2. Cover Sequence 3 consists mainly of volcanoclastic rocks, conglomerates, sandstones, shales and carbonates, and is the host to Pb-Zn-Ag mineralisation in the Mount Isa Block.

For a comparison between the Western, Kalkadoon-Leichhardt and Eastern Fold Belts, see Fig. 4.2.

Several attempts have been made to constrain the timing of the main deformational events in the Mount Isa Block during the Isan Orogeny, which vary substantially in relation to spatial aspects, isotopic dating and interpretation (e.g. cf. Page & Bell, 1986; Page & Sun, 1998; Bell & Hickey, 1998) (see Table 4.1). More recently Giles & Nutman (2002) challenged the common perception of orogeny in the Mt Isa Block in which 'peak metamorphism', and the deformation events associated with it, can be correlated across the entire Mount Isa terrane.

Table 4.1. Correlation of deformational history in three locations of the Mount Isa Block, including a summary of age dates from several locations.

Deformation Event	Eastern Fold Belt Age	Western Fold Belt Age	Selwyn Region Adshead-Bell (1998)	Selwyn Region Jaques <i>et al.</i> (1982)	Selwyn Region Beardsmore (1992)
<b>D<sub>1</sub></b> N/S Compression		<b>D<sub>1</sub></b> - 1610 ± 13 Ma (Page & Bell, 1986)	<b>D<sub>1</sub></b>		<b>D<sub>1</sub></b>
<b>D<sub>2</sub></b> E/W Compression	<b>U/Pb</b> 1584 ± 17 Ma (Page & Sun, 1998) <b>Ar/Ar</b> 1590 Ma (Perkins & Wyborn, 1998) 1580 -1600 Ma (Giles & Nutman, 2002)	<b>D<sub>2</sub></b> - 1544 ± 12 Ma (Page & Bell, 1986) 1580 ± 5 Ma (Hand & Rubatto, 2002)	<b>D<sub>2</sub></b>	<b>D<sub>1</sub></b>	<b>D<sub>2</sub></b>
<b>D<sub>3</sub></b> E/W Compression		D <sub>2.5</sub> (Bell & Hickey, 1998)	<b>D<sub>3</sub></b>		
<b>D<sub>4</sub></b> E/W Compression	<b>U/Pb</b> 1493 – 1508 Ma (Page & Sun, 1998)	<b>D<sub>3</sub></b> - 1510 ± 13 Ma (Page & Bell, 1986)	<b>D<sub>4</sub></b>	<b>D<sub>2</sub></b>	<b>D<sub>3</sub></b>
<b>D<sub>5</sub></b> E/W Compression			<b>D<sub>5</sub></b>		
<b>D<sub>6</sub></b> E/W Compression		<b>D<sub>4</sub></b> (Bell & Hickey, 1986)	<b>D<sub>6</sub></b>		<b>D<sub>4</sub></b>

#### 4.2.2 The Western Fold Belt

In the Western Fold Belt three superbasins have been identified and delineated; the Leichhardt Superbasin (ca. 1800 -1740 Ma), Calvert Superbasin (ca. 1730 – 1690 Ma) and Isa Superbasin (ca. 1665 – 1575 Ma) (Fig. 4.3). Preceding the development of the Isa Superbasin, a complex history of extensional basin development, sedimentation and volcanism resulted in two superimposed and unconformity bounded basins; the Leichhardt Superbasin and the Calvert Superbasin. The Leichhardt Superbasin, which was controlled by half-graben bounding faults (O'Dea *et al.*, 1997), is essentially comprised of shallow marine and fluvial sediments and bimodal igneous rocks and formed during the Leichhardt Rift Event (Betts & Lister, 2002) (Fig. 4.3). Basin inversion then followed, with localised shortening evident in the Leichhardt Superbasin (Betts, 1999). Following basin inversion extension was accompanied by shallow marine and fluvial sedimentation and bimodal volcanism in developing half-grabens (Betts *et al.*, 1998; 1999; Southgate *et al.*, 2000) in association with the development of the Calvert Superbasin (Jackson *et al.*, 2000) and the Mount Isa Rift Event (O'Dea *et al.*, 1997).

Reactivation of N/S rift bounding faults and E/W cross-rift faults during the Mount Isa Rift Event to some extent controlled the architecture of the Calvert Superbasin and subsequent sedimentation. Half-graben bounding faults were active in the Lawn Hill Platform and transverse faults, such as the Termite Range Fault, were considered active during deposition of the Isa Superbasin (Scott *et al.*, 2000). The Isa Superbasin has been interpreted as the result of a sag phase or thermal subsidence (Betts *et al.*, 1998). This subsidence appears

to have been more extensive to the west/northwest of the Leichhardt River Fault Trough (Fig. 4.1), which resulted in extensive deposition of carbonaceous shale, sandstone and siltstone and formed the McNamara Group (ca. 1660 – 1595 Ma) which is the host to the major shale-hosted massive sulphide Pb-Zn-Ag deposits of the region (Fig. 4.4). Most deposit Pb-Pb or U-Pb ages correspond well with their host successions, Century being the main apparent exception which is dated at around  $1575 \pm 6$  Ma (Carr, 1996), 20 Ma younger than the  $1595 \pm 6$  Ma host sediments. However, the Pb isotopic ratios could have been potentially influenced by later more radiogenic fluids. Moreover, the  $1595 \pm 6$  Ma age for the H4s re-sedimented tuff-beds are maximum ages that do not necessarily coincide with the sedimentation age, and could be younger, overlapping with mineralisation timing in analogy to e.g. Mount Isa, McArthur River (HYC) and Broken Hill.

This extensional history and overall basin development was interrupted by compression, basin inversion and regional wrenching during the Isan Orogeny ca. 1585-1500 Ma (O'Dea *et al.*, 1997, Betts *et al.*, 1999). The subdivisions of the Mt Isa Block display contrasting responses to deformation in the region, with associated strain less intense in the Western Fold belt than that of the Eastern Fold Belt due to strain accommodation by underlying basin fault architecture (Betts, 2001). In the Eastern Fold Belt thin-skinned tectonics dominate with shallow dipping faults, whereas in the Western Fold Belt, brittle deformation affected much of the upper crust. The Kalkadoon-Leichhardt Belt consists of older, exposed basement rocks which accommodated the

deformation by working as a buttress during periods of crustal shortening (Drummond *et al.*, 1998).

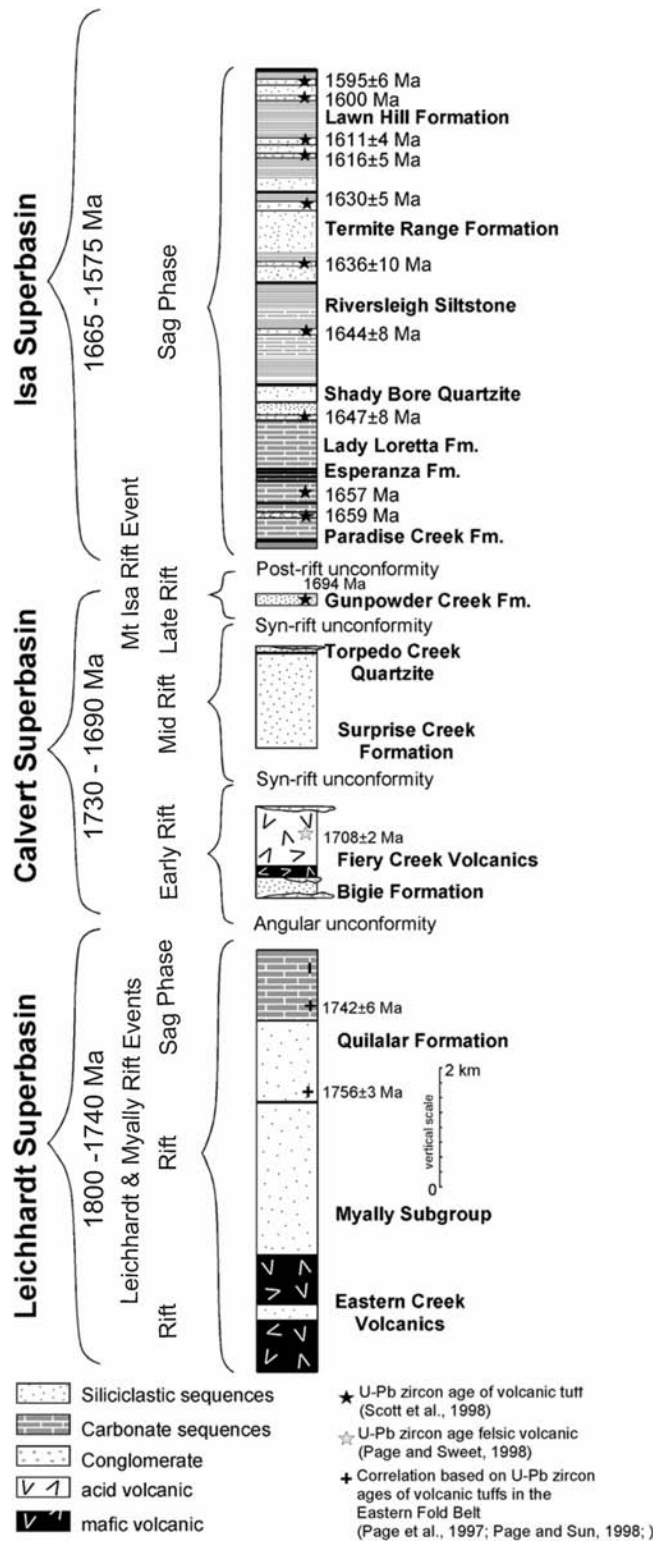


**Figure 4.3.** Simplified lithostratigraphic column of the Western Fold Belt displaying the three Superbasins and associated rifting sequences. Geochronological data after Scott *et al.* (1998), Page & Sun (1998), page & Sweet (1998) and Page *et al.* (1997), (modified from Betts *et al.*, 2004).

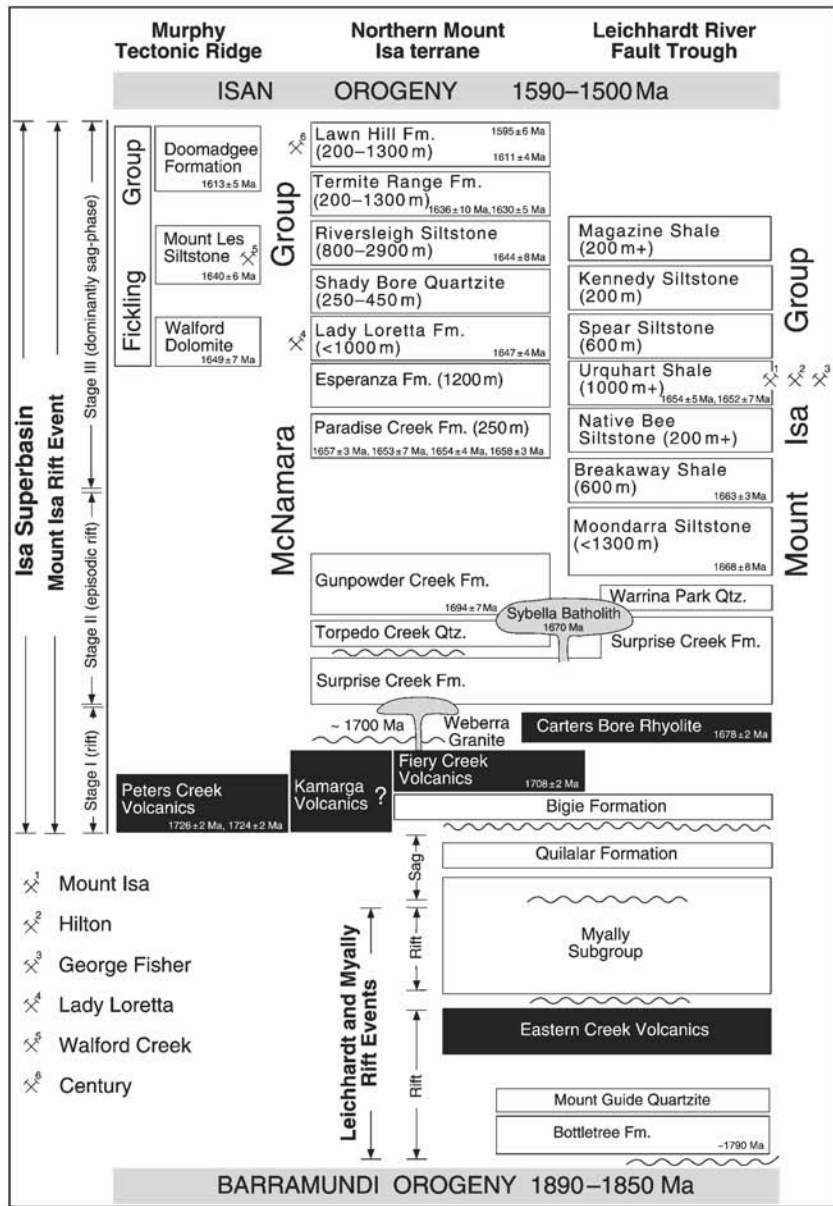


**Figure 4.4.** Stratigraphic correlations in the Western Fold Belt displaying the major ore deposits and the age of stratigraphic horizons within the McNamara Group, (after Betts & Lister (2002)).

### 4.2.3 Stratigraphy of the Lawn Hill Formation

The Lawn Hill Platform (Plumb & Derrick 1975) represents the northern part of the Western Fold Belt (Fig. 4.1). Here, Zn-Pb mineralisation (e.g. Century zinc deposit) occurs preferentially in a number of stratigraphic layers hosted in the

McNamara Group (Fig. 4.5). Previous interpretations of O'Dea *et al.* (1997) and O'Dea & Lister (1995) view this thick package of sediments as being deposited during alternative phases of rift and sag episodes, with no significant

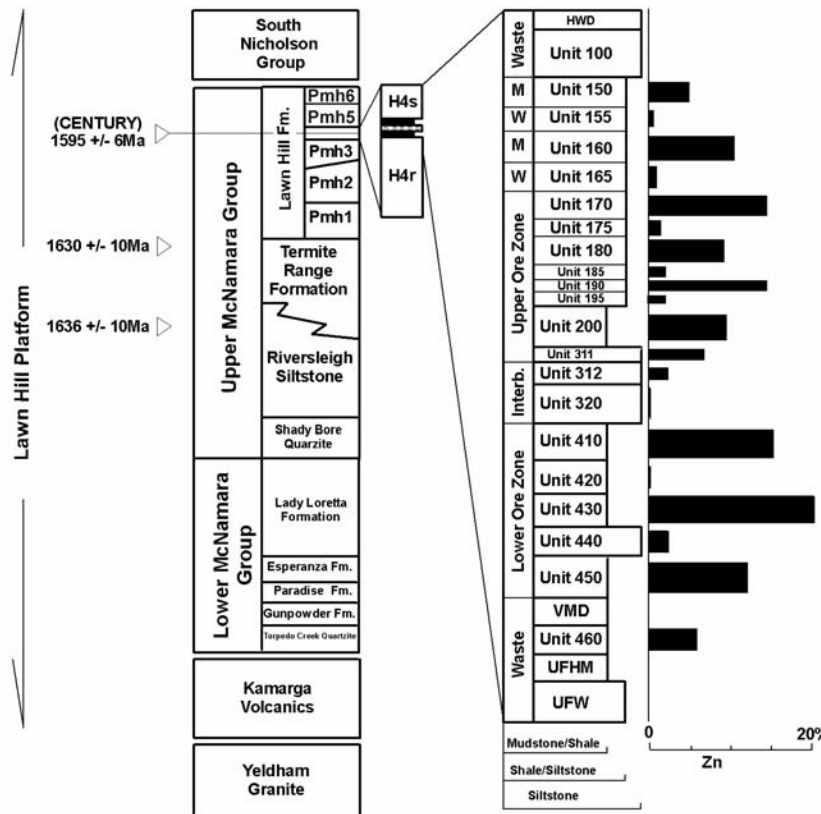


**Figure 4.5.** Stratigraphy of the Lawn Hill Platform indicating the relative location of the Century Deposit and stratigraphic ages. On the right, a detailed stratigraphy of Member Pmh<sub>4</sub> with the Century Ore Zone linked to grade distribution of %Zn.

tectonic activity (Betts, *et al.*, 1998). Scott (1998) and Krassay (2000a) reinterpreted the seismic stratigraphy of this package of sediments, suggesting that several tectonic events occurred during and after sedimentation. Syn-sedimentary deformation is documented by the identification of syn-sedimentary growth faults across the Elisabeth Creek zone. The most obvious structural feature in the region is the northwest striking Termite Range Fault (Andrews, 1998; Betts *et al.*, 1998; Broadbent, 1998) which has been

considered the major fluid pathway for mineralisation (Broadbent *et al.*, 1998). The Termite Range Fault (TRF) has been described as a long-lived transverse fault (Betts, *et al.*, 1999; Ord *et al.*, 2002) and was most likely active for > 140 million years. The TRF has had a major influence in the deposition of sediments throughout the upper McNamara Group and has localised sedimentary depocentres (Andrews, 1998). Lateral variations in sedimentation can be found in and around the Century deposit suggesting local thickening, which Broadbent *et al.* (1998) describes as a result of parasitic faults emanating from the TRF. However, other east-northeast and northeast striking, steep, reactivated faults represent an important characteristic of this region, and were probably also important in transferring brines and controlling deposit locations across the Lawn Hill Mineral Field (see below).

The McNamara Group rocks in the Lawn Hill Platform form the youngest cover successions of the Mount Isa Block, correlative with the Fickling Group (Sweet *et al.*, 1981; Blake, 1987; Blake & Stewart, 1992; Andrews, 1998; Krassay, 2000a) (see Figure 4.4). The upper McNamara Group comprises up to 7500 m of deep marine, paralic and terrestrial, siliciclastic-dominated facies of the Shady Bore Quartzite, Riversleigh Siltstone, Termite Range Formation, and Lawn Hill Formation. The Century orebody and surrounding vein-hosted mineralisation is stratigraphically constrained within the upper part of the McNamara Group in the Termite Range Formation and Lawn Hill Formation. This was subdivided by Sweet and Hutton (1982) into six members, Pmh<sub>1</sub>-Pmh<sub>6</sub> (Fig. 4.5). Andrews (1998) distinguished two additional members: H<sub>1s</sub> within Pmh<sub>1</sub> and H<sub>4s</sub> (host to Century Zn-Pb-Ag mineralisation) at the top of member

Pmh<sub>4</sub> (Fig. 4.5). Members Pmh<sub>1</sub>, Pmh<sub>2</sub>, Pmh<sub>4</sub> and Pmh<sub>6</sub> are dominantly fine grained and carbonaceous and represent a low energy, deep subaqueous environment. Pmh<sub>3</sub> is a sandy interval and represents a shallower, higher energy marine setting. Member Pmh<sub>5</sub> comprises thick lithic and feldspathic sandstone interpreted either as high-energy marine shelf deposits (Sweet & Hutton 1982) or sandy turbidites (Andrews 1998). More recently, after the accomplishment of the North Australian Basin Resource Evaluation (NABRE) project, the lithostratigraphy has been reorganised in light of new concepts of sequence stratigraphy (refer to Southgate *et al.*, 2000). Outcomes of the NABRE project resulted in an updated stratigraphy that is based on erosional and maximum flooding surface boundaries, new geochronology results (Page *et al.*, 2000), and also palaeomagnetic data sets to constrain the depositional conditions (Idnurm, 2000; Southgate *et al.*, 2000).

In sequence-stratigraphic terms the Lawn Hill Formation comprises the upper part of the Term Supersequence and the Lawn, Wide and Doom Supersequences (Krassay *et al.*, 2000b) (see Fig. 4.6). The Century zinc deposit is hosted in the Wide supersequence (Wide 1), representing a third order maximum flooding surface, suggesting low energy conditions. As relative sea level reached this maximum flooding surface, basins became starved of sediment deposition, resulting in a condensed section, which may have favoured the concentration of sulphides, particularly in shale units (Ruffell, *et al.*, 1998).

The Lawn Hill Formation contains tuffs and reworked tuffs at a number of stratigraphic levels. Page & Sweet (1998) dated a population of zircons ( $1595 \pm 6$  Ma) in the mineralised member Pmh<sub>4</sub> (from Century drill core). Page *et al.* (2000) also presents consistent results from four new samples, two from

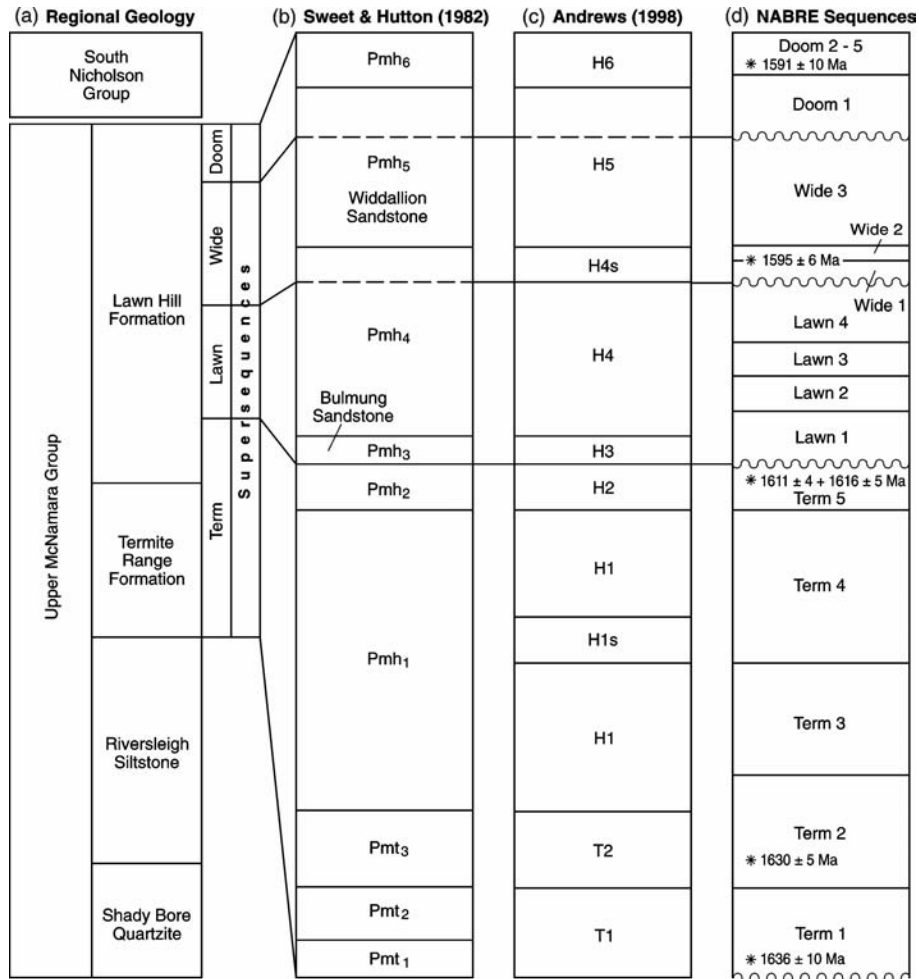


**Figure 4.6.** Stratigraphic columns comparing the various classification schemes for rocks of the upper McNamara Group. (a) Regional geology for entire McNamara Group after Hutton *et al.* (1981). (b) Upper McNamara Group formally defined lithostratigraphic units after Sweet and Hutton (1982). (c) Upper McNamara Group informal lithostratigraphic units by Andrews (1998). (d) North Australian Basin Resource Evaluation (NABRE) sequence-stratigraphic terminology and SHRIMP depositional zircon ages from the central Lawn Hill Platform. After Krassay *et al.* (2000).

member Pmh<sub>2</sub> (Lawn Supersequence,  $1616 \pm 5$  Ma;  $1611 \pm 4$  Ma) one from member Pmh<sub>4</sub> (Lawn Supersequence,  $1595 \pm 6$  Ma) and one most likely derived from member Pmh<sub>6</sub> (Doom supersequence,  $1591 \pm 10$ ). The ages

derived from Pmh<sub>2</sub> (1616 ± 5 Ma and 1611 ± 4 Ma) are stratigraphically in accordance with the age of 1595 ± 6 Ma for Pmh<sub>4</sub>. Well established geochronological constraints, coupled with sedimentary evidence presented by Krassay *et al.* (2000a), argue strongly for a tectonic control of the major (2<sup>nd</sup>-order) supersequences, and most 3<sup>rd</sup>-order accommodation cycles (sequences) across all of the Isa Superbasin. Evidence of a tectonic influence includes facies changes and thickness trends related directly to active faults, partitioning of depocentres by these faults, abrupt provenance switching, tilting and erosion of older sedimentary sequences. Furthermore, Krassay *et al.* (2000a) suggests that the Isan Orogeny may have commenced during deposition of Doom 4 and Doom 5. These final considerations suggest that the D<sub>1</sub> phase of the Isan Orogeny probably postdated the depositional age of sediments hosting the Century mineralisation.

### **4.3 Century Deposit**

The Century deposit is one of the largest Zn-Pb-Ag accumulations in the world with a mineral resource of 138 Mt at 8.23% Zn, 1.16% Pb, and 29 g/t Ag (Clifford and Kelso, 2003). This stratiform mineralisation has not been as extensively studied as other Zn-Pb metal occurrences in the Isa and McArthur Superbasins e.g., Mount Isa, McArthur River (HYC), Lady Loretta etc., as it is one of the more recent discoveries (1990 CRAE exploration Ltd.).

#### **4.3.1 Sulphide Textures**

The main stratiform mineralised units are a finely laminated shale unit consisting of essentially fine grained sphalerite and siderite with minor galena

and pyrite. The presence of hydrocarbons or pyrobitumen with porous sphalerite has been discussed in detail by Broadbent (1999). However, the non-porous sphalerite has no clear relationship to pyrobitumen; it also has the highest grade and volume within the mineralised sequence. The subdivision Pmh<sub>5</sub>, which is comprised of a thick (~150 m) cemented chlorite rich sandstone lies directly above the 'ore zone'. Broadbent (1999) and Ord *et al.* (2002) have interpreted this unit as a potential seal in the system due to its characteristics and early cementation (Andrews, 1998). Discordant mineralisation (at meso-scales) is relatively minor, and comprises veins and irregular patches, typically galena-dominant (Broadbent, 1998). Vein-style mineralisation which is completely discordant to bedding is common in an area of about a 30 km radius around Century (e.g. Silver King, Waltho and Andrews (1993)).

#### 4.3.2 Ore Zone Stratigraphy

The 'ore zone' is contained in the subdivision Pmh<sub>4</sub>, which is comprised of over 500 m of interbedded siltstone and shale units with minor mudstone is summarised in Figure 4.5. Logging of ore zone units has suffered from inconsistent unit definitions in the past. With the completion of re-logging in the Solid Geology project (King, 2002) the ore zone units are now much more consistently constrained (Fig. 4.7).

The upper ore zone generally consists of interbedded siltstone and shale bands (Fig. 4.7), and varies from very well laminated to stylolitic layers, with evidence of layer parallel shearing in several units. Unit 200 (3-5 m) is the first major ore unit but has quite a different appearance in Stages 1 and 2 (the southern part of

the mine) to the majority of the north block. In Stages 1 and 2 this unit was commonly a massive mudstone interval which was frequently brecciated and deformed by bedding parallel shear, coincident with high lead grades. In the north block the unit occasionally suffers bedding parallel shear but is a well-laminated shale (similar to Unit 160) with only rare mudstone intervals. Unit 310 is a transitional unit from the shales of Unit 200 to the siltstones of Unit 320. As the upper part of the unit can contain some very high-grade mineralisation it has been split into Units 311 and 312 on the basis of assay information (Unit 311 is > 6.5% Zn). The relative thickness of these units is variable and either can comprise the entire interval. If there is no assay information or the unit is affected by hematite alteration it is logged as Unit 310. Unit 311 is the lowest unit in the Upper Zone ore and Unit 312 is the first unit of Internal Waste. Interburden within the ore zone relates to Unit 320 (2.5-3.5 m) and was called the Cappuccino zone by CRA due to the sideritic buff coloured stylolitic siltstones, which comprise the entire interval and the majority of the Internal Waste. The lower ore zone generally consists of high-grade well-laminated black shale with interbedded mudstone.

Century Mine Stratigraphic Column															
Sequence <sup>2</sup>	Unit	Unit Code <sup>3</sup>	Domain/Lithology	Description - Lithology and alteration	average thickness (m)	%Zn	%Pb	g/kg	%Fe	%Mn	%S	%SiO <sub>2</sub>	%C	Density	Sequence <sup>2</sup>
waste	Cambrian Limestone	CLS	limestone	bedded limestone										2.69	
	Carbonate Breccia CBX	CBX	carbonate breccia	limestone breccia										2.67	
	Hanginwall Sandstone	HWS	sandstone	quartz sandstone	>150									2.54	
	Hanginwall Sandstone	HWS	sandstone	sandstone interbedded shale	25									2.62	
	Hanginwall Siltstone	HWD	siltstone/shale	interbedded siltstone and thin shale	85-100									2.72	
	siltstone		siltstone/shale	Thinly interbedded siltstone and shale with stylolitic alteration	3.3	1.8	0.2	13	9.1	1.0	2.0	62.5	2.6	2.72	
	Shale Band		shale	Interbedded shales and siltstones of variable thickness and usually poor mineralisation	0.9	4.2	0.3	27	9.4	1.0	5.8	45.6	3.4	2.83	
	siltstone		siltstone/shale	interbedded siltstone and thin pyritic / mineralised shale. Siderite /styolite alt'n.	4.6	1.0	0.1	5	10.8	1.3	1.1	63.1	2.4	2.74	
	Shale Band 1		shale	thinly bedded characterised by sphalerite and pyrite in thin bands.	1.4	5.0	0.7	45	9.0	0.9	5.7	53.3	2.8	2.84	
	siltstone		siltstone	Thinly interbedded SH & SLT. It can contain some mineralised shales. Sideritic	3.3	1.4	0.2	8	10.1	1.2	1.1	65.7	2.3	2.73	
Shale Band 2		shale	B2 is similar to B1, it can be Zn rich at the base grading up into pyrite SH	1.1	10.3	2.4	162	6.9	0.2	11.1	52.2	3.6	3.02		
siltstone		siltstone	thick beds and coffee-brown colour, similar to Unit 320. Strong siderite / styolite alt'n.	2.3	1.8	0.3	13	14.6	1.7	1.2	49.9	4.4	2.87		
Shale Band 3		shale	B3 has little or no pyrite, and is high Zn. Typically defines the top of the Upper Ore Zone.	0.9	15.2	2.9	282	6.5	0.2	13.3	41.1	4.3	3.13		
siltstone		siltstone	Usually grey in color	0.9	2.0	0.9	21	7.3	0.9	1.5	68.0	1.9	2.69		
Shale Band 4		shale	Usually high in Pb (the "Galena Band") may be boudinaged, resembling Unit 200.	0.7	8.7	7.0	131	4.7	0.2	9.0	58.4	2.3	3.11		
siltstone		siltstone	Usually thin bedded and coffee colored.	0.9	2.5	3.4	46	5.5	0.7	2.0	66.5	1.7	2.76		
Shale Band 5		shale	High grade Zn.	0.5	11.1	7.2	228	3.2	0.2	8.1	50.4	3.8	3.09		
siltstone		siltstone	Sometimes difficult to distinguish.	0.4	3.7	2.3	58	4.0	0.6	2.4	76.7	1.2	2.70		
Unit 200		unit 2	shale	Thick massive shale high grade Zn with galena-rich veins and boudinaged.	4.3	10.7	5.0	167	2.7	0.1	8.0	60.9	3.6	2.97	
Unit 311		311	shale/siltstone	thin bedded (fissile) SH/ST, minor mudstone marker.	0.6	12.1	0.6	71	8.1	1.2	7.4	45.1	3.1	2.95	
Unit 312		312	siltstone/shale	thin bedded (fissile) ST/SH.	2.0	4.1	0.7	16	8.3	0.9	4.8	59.8	2.8	2.80	
Unit 320		320	siltstone	Thick bedded barren sideritic siltstone known as the "Cappuccino Zone". Strong siderite/styolitic	3.0	1.2	0.3	3	10.1	1.4	0.9	61.5	2.9	2.73	
Unit 410		410	shale	High grade Zn. Thick bedded shale with strong laminations of sphalerite.	3.4	18.7	2.5	51	4.3	0.7	11.6	41.2	5.7	3.07	
Unit 420		420	mudstone	Carbonaceous sideritic mudstone band recognisable by lack of bedding and conchoidal fracture.	1.1	0.9	0.3	2	8.1	1.7	0.7	59.8	3.6	2.67	
Unit 430		430	shale	High grade Zn. Thick bedded shale with strong laminations of sphalerite.	2.3	23.4	1.2	22	4.8	0.6	14.1	36.9	4.8	3.13	
Unit 440		440	siltstone	Thin band similar to Unit 320, known as the "Baby Cappuccino Zone". Strong siderite/styolite alt'n.	0.5	2.4	0.1	3	16.9	2.9	1.4	38.0	5.5	2.97	
Unit 450		450	shale	Zn rich top grading down into a pyritic base. Assay based cutoff into footwall, marker bed for contact VMD	5.4	13.5	0.6	6	8.1	0.9	11.6	39.9	4.6	3.03	
VMD		VMD	mudstone	Sideritic mudstone, lacks bedding & conchoidal fracture - Vicki's mudstone	0.2										
Unit 460		460	shale	Pyritic rich shale with minor sphalerite	1.9	5.20	0.30	6	8.8	0.8	7.6	52.0	3.5		
UFHM		UFHM	mudstone	Sideritic mudstone, lacks bedding & conchoidal fracture - Homers mudstone	0.4										
Footwall Shale UFW		UFW	shale/siltstone	Thinly bedded siltstones and shales. Weak siderite. Characterised by lack of sulphides and stylolite texture.	80.0									2.62	

1. Ore type / grade control col.2, colours used in Vulcan  
 Thickness, SiO<sub>2</sub> & C from PTD channel sampls - Other grades from STM020404  
 updated by M Clifford 17/06/02

Figure 4.7. Stratigraphic summary and description of the Century Deposit (courtesy of Century mine & I. Kelso).

#### **4.4 Introduction to 3D Structural Modelling**

The primary objective of almost every geological characterisation is concerned with predicting the spatial variation of one or more geological variables (Houlding, 1994). A conventional approach that is commonly used to define a geological entity is a 2D representation of the geology using a map or a cross-section, as our ability to deal with geometrical problems in 3D is limited and it is difficult to represent it visually. However, since the advent of computerised methods, defined as CAD (computer aided design), most of these difficulties have been overcome, enhancing our understanding and providing new ways of dealing with complex geometrical problems in 3D space. In computer aided design, a geological scenario requires a mathematical description of the components. This process happens when we adopt algorithms that use discretization and qualification of irregular geological space into irregular volumes, with similar distinguishing characteristics. Some of the most common characters used to define geological space are lithological subdivisions or physical properties such as density, permeability and mineralisation content, amongst others.

Several types of investigative sources are available and are commonly used to gather the information necessary to construct a generic model, which comprises a set of well constrained geological spaces. The implemented data, when we consider the representation of a mineral deposit, are generally of two types a) a direct sampling of a discrete and representative quantity of rock, soil or unconsolidated sediment; or b) an indirect quantification of a property of the geological space using i.e. topographical, geochemical, or geophysical

investigations. This information is made up of a range of observations that must be weighted. For example, we might have data that is collected in outcrops with 99% confidence on its location and geological characteristics, or a geophysical survey that can be regarded as fuzzy in terms of location and geological characterisation. Thus, there is a need to quantify the quality of the information available considering its source, before we integrate it within a generic 3D model. Creating geologically relevant 3D models from low relief, poorly exposed and geologically complex regions is a daunting if not impossible task (de Kemp, 2000). As a consequence, it is also important to have a clear understanding of the spatial density distribution of data used during the interpretative construction of the geology.

Once the representative geometries are defined, the evaluation of the results of a geological characterisation typically involves spatial analysis of the variation of one or more variables. This can be done using modern visualisation tools that allow not only a rapid correlation analysis, but also an interactive query of the database that creates the 3D model. This consents to quantifying the information displayed, facilitating its understanding.

#### 4.4.1 GoCad, a 3D Geologically Optimised CAD Package

To construct a 3D structural model of the Century deposit we chose to use a software package that differs from conventional CAD modelling packages. GoCad (Earth Decision Sciences, 1998) has been used recently as a modelling package designed to model natural objects, in contrast with traditional CAD platforms, which are based on mathematical formulations and polynomial

algorithms (e.g. Barnhill, 1985; Bézier, 1974; de Boor, 1972; Farin, 1988), and mostly developed to meet the needs of industries that make manufactured objects. These two approaches are different in the sense that modelling geological objects has to respect the data imported during the preliminary phase of model construction, unlike many CAD applications that have a primary aim of creating models with smooth and consistent curves, surfaces and volumes. Consequently, GoCad has developed new standards in dealing with complex geological problems. The software has been developed, and continues to be developed within a consortium, which is widely open both to the industry and universities around the world. These organisations (e.g. pmd\*<sup>2</sup>CRC - Predictive Mineral Discovery Cooperative Research Centre) are interested in the new approach to geomodelling proposed by GoCad, and want to use and/or contribute to the development of this new technology.

Mallet (2002) presents a comprehensive description of the mathematical algorithms behind GoCad, in particular discussing the DSI (discrete smooth interpolation algorithm) that represents the core of this application. The GoCad technology prefers to adopt a discrete method that is close to a “finite element” approach, rather than use a parametric approach based on continuing polynomial functions. Discrete modelling methods are well known (e.g. Briggs, 1974; Akima, 1978; Sibson, 1981; Mallet, 2002; Overveld, 1995) and represent an easier way to mathematically deal with complex geological problems.

GoCad allows the definition of several types of constraints, and some of these constraints may be imposed to respect the data inserted within the model,

others can be used to constrain the structural interpretation when the data is limited. In particular, these constraints are useful for modelling stratigraphic layers and faults. The final model obtained represents a combination of data interpolation and geological interpretation imposed by the user during the modelling process.

#### 4.4.2 Initial Steps to Construct a 3D model

The basic requirements and procedures adopted to construct the 3D model of the Century Zn-Pb-Ag deposit can be summarised as a sequence of clearly defined steps:

- *Management, Correlation and Integration* of the various information sources available from site investigation. The most important, and potentially most time consuming, aspect of this step is spatial correlation of the available data sources.
- *Review and Analysis* of the information sources in terms of their quality, sufficiency, scale and spatial variability. This provides an initial appreciation of the complexity and magnitude of the conditions we have to deal with. It also allows us to identify the geological characters that influence the spatial variation of the variables of interest.
- *Interpretation* of geological stratigraphy, structure and other relevant factors, based largely on observation of characteristics. The result is a discretization of the subsurface continuum by controlling geological characteristics. The operative term here is *interpretation*, because we are commonly forced to apply our geological intuition and experience to compensate for limited primary data.

- *Prediction* of the spatial variation of relevant variables, based on sample information, geological interpretation and appropriate prediction techniques. The operative term in this case is *prediction*, the true conditions are seldom determinate from limited information and our predictions are always subject to some degree of uncertainty.
- *Spatial Analysis* of the interpreted and predicted information, generally in terms of volumetrics and visualisation procedures, and/or transfer of the characterisation results to the relevant end process, such as mine planning or fluid flow modelling.

#### 4.4.3 Data Acquired to Construct the 3D Model

To construct the 3D model of Century and the Lawn Hill mine lease area we have initially developed a mine scale model that uses most of the data collected during exploration and resource evaluation carried out initially by Rio Tinto and subsequently by Pasminco Ltd., and also a range of data gathered during recent exploitation activities, which involved the design and development of several open-cut stages. In a second, more advanced phase of this project, we have integrated the deposit model with selected data at regional scale. The main sources of data were a) the Pasminco Century mine database b) Solid Geology reports and c) aerial photography.

#### 4.4.4 3D Model Components

The Century model in its final stage includes a highly detailed 3D reconstruction of the faults at the deposit and regional scale, a set of horizons representing the topology of some of the highly mineralised intervals, and a Digital Terrain Model

(DTM) representing a 3D reconstruction of the mine lease. Interesting results were obtained when comparing the data at different scales, and projecting some of the drilling database information over the mineralised Unit 200 (see Fig. 4.7) with the intent of visually evaluating the relationship between fault distribution versus thickness and grade variation across the Century deposit.

#### 4.4.5 3D Modelling Results

As we mentioned in the initial introduction of this chapter we have attempted to use the 3D model to gain insights into ore genetic processes. After this initial consideration we have defined three research questions as follows:

- 1) What was the link between the fault architecture and the mineralisation within the Lawn Hill Mineral Field?
- 2) What were the faults that may have contributed to ore transport and deposition other than the Termite Range Fault?
- 3) Which structures were the primary growth faults within the Century system, and did they play an important role for mineralisation?

To answer these questions we have tried to identify if regional scale faults mapped in 3D using the DTM (Fig. 4.8a) (in combination with aerial photography), intersect the mineralisation at depth. We also used the model to define what the important faults for mineralisation were, and we attempted to evaluate the relative timing of faulting events.

The rapid visualisation of all the structural data using GoCad, reveals continuity between NE trending regional scale structures and faults within the Century deposit (Fig. 4.8ab). We recognise that the regional Silver King Fault (SKF) most likely intersects Century. This link is supported further by a range of data that includes thickness variations and grade distributions at the Century scale (see below), and the topology of the Hangingwall Sandstone (see Fig. 4.7) surface in the hangingwall of the ore zones. Within the deposit we also recognise that the evolved geometry of the Termite Range Fault (TRF) is surely the result of significant reactivation. Moreover, it is important to remark that NE striking faults were coevally active with the Termite Range Fault from early stages of sedimentary deposition. Evidence of NE structures, intersecting older sediments of the Termite Range Formation, indicates a similar history of reactivation. However, several faults mapped in the pit area are relatively young parasitic branches (e.g. Gecko and Prosperity system faults) of TRF, and most likely developed during the later phase of wrench style deformation (Fig. 4.9). These faults seem to have only partially influenced the present distribution of ore. Superimposed on these events is a final extensional stage that has contributed to the present half graben structures and has subdivided the Century deposit in three independent fault blocks separated by E-W striking structures (e.g. Pandora's Fault). The NE structures can be interpreted as reactivated as some of them displace the E-W faults.

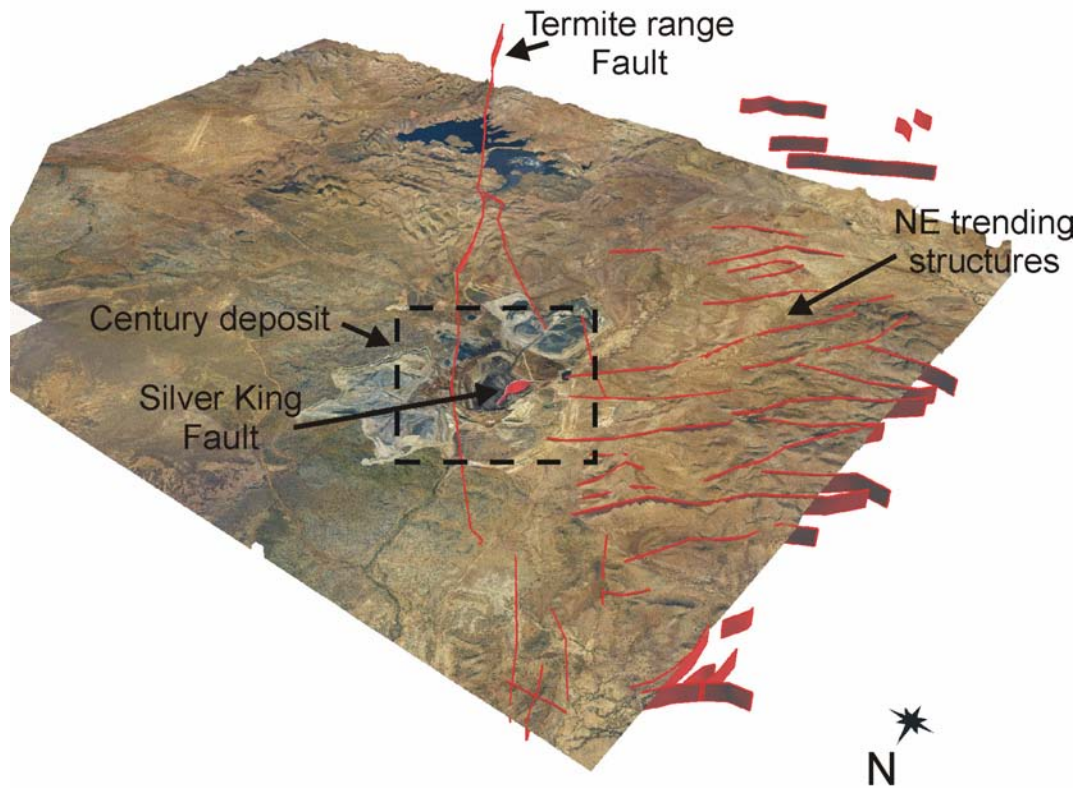


**Figure 4.8a.** Digital Terrain Model (DTM) of the Century deposit and surrounding region, displaying the Century deposit and NE trending structures.

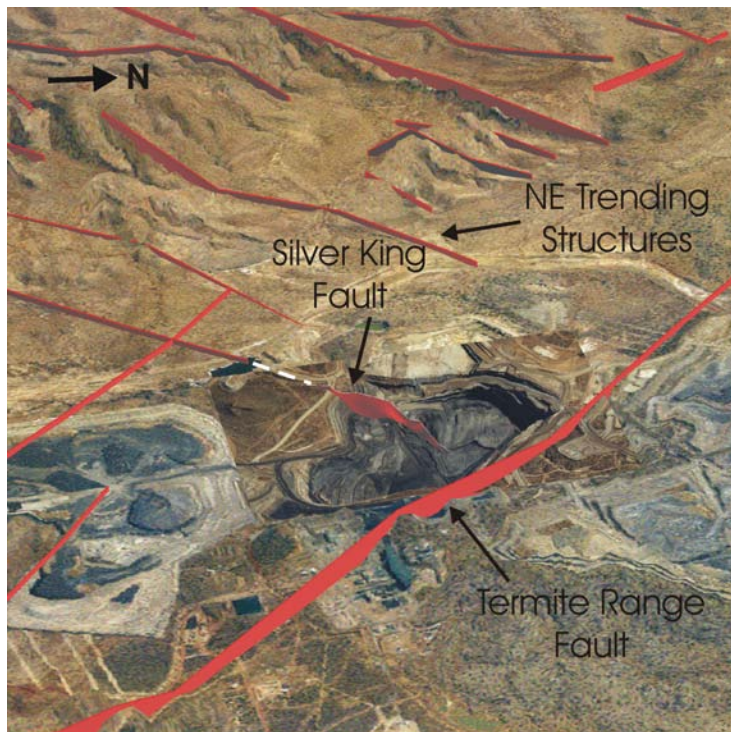


**Figure 4.8b.** Digital terrain Model (DTM) of the Termite Range fault intersecting the Century deposit, and highlighting the potential link between NE trending regional structures and the Silver King Fault

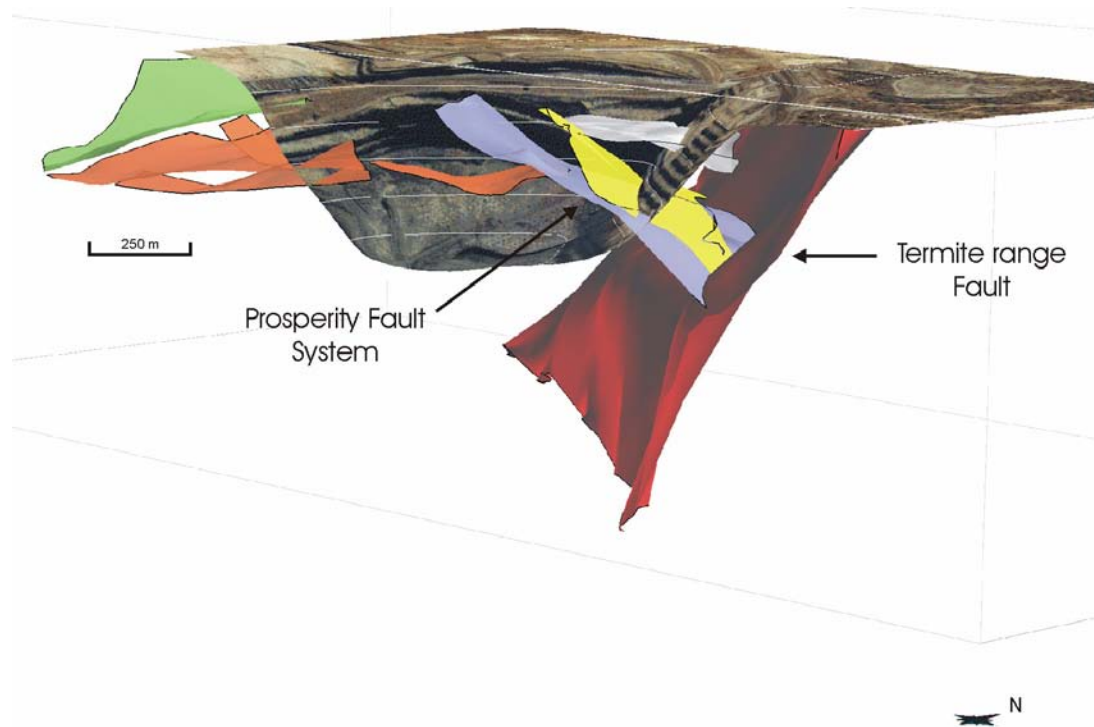


**Figure 4.9.** Digital Terrain Model (DTM) integrated with 3D structural data, highlighting the Termite Range Fault and the parasitic Prosperity Fault system.

The trace of the SKF corresponds well to a significant zone of thickness variations observed within the deposit, (Fig. 4.10ab) and most likely represents a reactivated growth fault; however some of the thickening could be due to later localised thrusting, especially within the shale 200 interval. The topology of Unit 200 is not influenced by significant deformation along the SKF, possibly supporting the growth fault model. However this might be due to a different response of the shales (less competent units) to subsequent deformation. In addition, the shales show some evidence of parallel bedding shear.

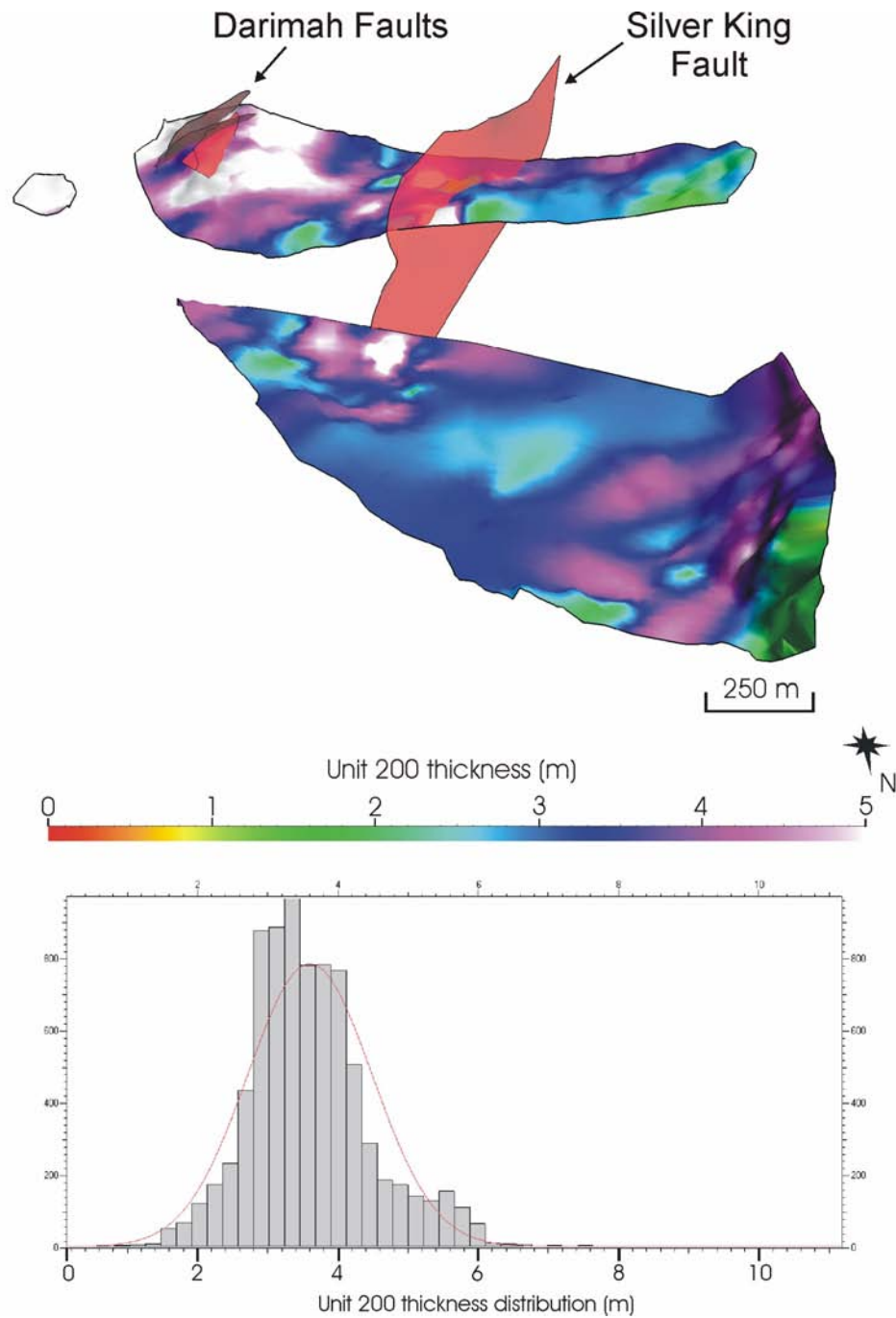


**Figure 4.10a.** 3D representation of the thickness variation in Unit 200 of the Century deposit looking south. Note the correlation of thickness increase with NE trending faults. Below: Histogram displaying the thickness distribution of Unit 200.

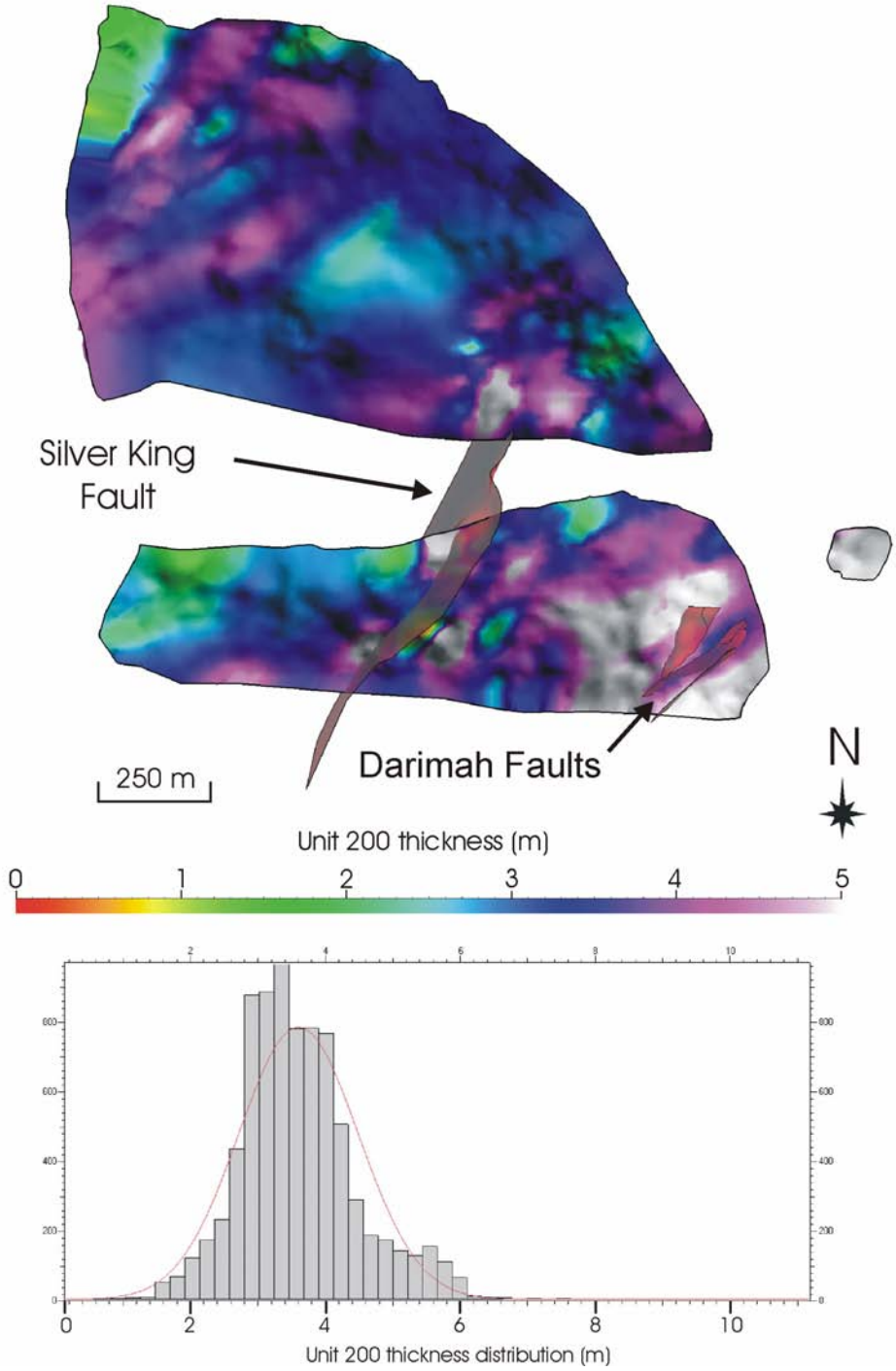


**Figure 4.10b.** 3D representation of the thickness variation in Unit 200 of the Century deposit looking north. Note the correlation of thickness increase with NE trending faults. Below: Histogram displaying the thickness distribution of Unit 200.

Grade distributions of both Zn and Pb correlate well with NE trending structures and Pb distribution in Unit 200 displays higher grades closer to the TRF (Fig. 4.11ab) also associated with NE trends. The distribution of Zn in Unit 200 displays isolines with similar NE trends; and the high grade Zn zone overall is distal relative to the TRF (Fig. 4.12ab). The isopach map of Unit 200 indicates that major sedimentary thickening occurs in the south eastern corner of the deposit and also within channelled domains in the northern block. In both cases the thickening seems to be associated with NE trending structures if we consider the distribution of isolines. These NE trends of thickness are parallel to trends observed in the Pb and Zn grades.

In summary the main conclusions made in relation to this study are:

- 1) The 3D model shows that not only the TRF was active, and played a significant role in ore deposition processes, but other active faults in the system display correlations with thickness and mineralisation. The intersection of NW and NE structures could have been particularly important in focussing fluids
- 2) The geometry of the TRF is the result of significant reactivation; however, several faults that have similar strike to the TRF, but dip towards NE, were interpreted to be relatively young parasitic branches of the TRF and were developed more likely during wrench style deformation occurring post-basin inversion, during the later stages of the Isan Orogeny.

- 3) Bedding parallel shear is a characteristic of the shale's response to the brittle deformation. Much of this deformation may be younger than the main movement on the TRF as it does not seem to have a major influence on the mineralisation. Some localised redistribution of galena, that we interpret as a product of internal remobilisation of laminated ore, occurs exclusively in bands included within specific mine stratigraphic units (e.g. Unit 180) with higher Pb weight % contents.
  
- 4) Metal distributions for Zn and Pb within Unit 200, which is one of the better constrained units in the upper ore zone, have pointed out the importance of NE trending structures as active faults that controlled ore emplacement.

#### **4.5 Century Ore Genesis**

Two ore genesis models have been proposed for Century, based largely on paragenetic and geochemical work. The first model proposes an early-diagenetic timing of mineralisation (Waltho and Andrews, 1993). Following this work, Broadbent *et al.* (1998) has reinterpreted some of the textural arguments proposed as evidence of syngensis to early-diagenesis and using new available lead, sulphur and carbon-oxygen data constrained using his detailed paragenesis, argues that a late-diagenetic to syn-tectonic timing for the mineralisation was more likely at Century. The main geological constraints and evidence for the Century late-diagenetic ore genesis following Broadbent *et al.*, (1998) are:

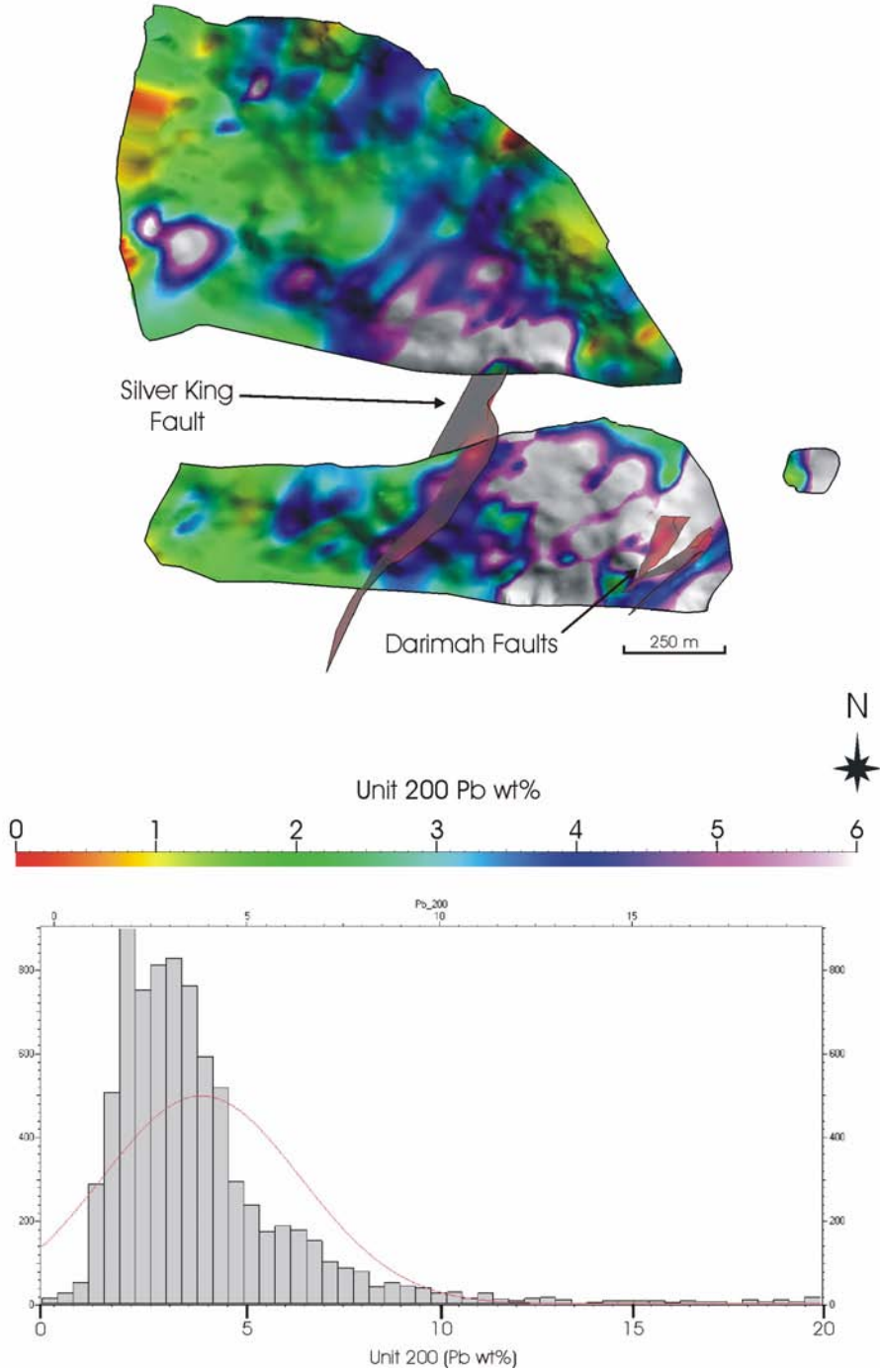


**Figure 4.11a.** 3D representation of the Pb distribution in Unit 200 of the Century deposit looking north. Note the correlation of higher grades with NE trending faults, and the spatial association of higher grade in the east (closer proximity to the Termite Range Fault). Below: Histogram displaying the Pb grade distribution of Unit 200.

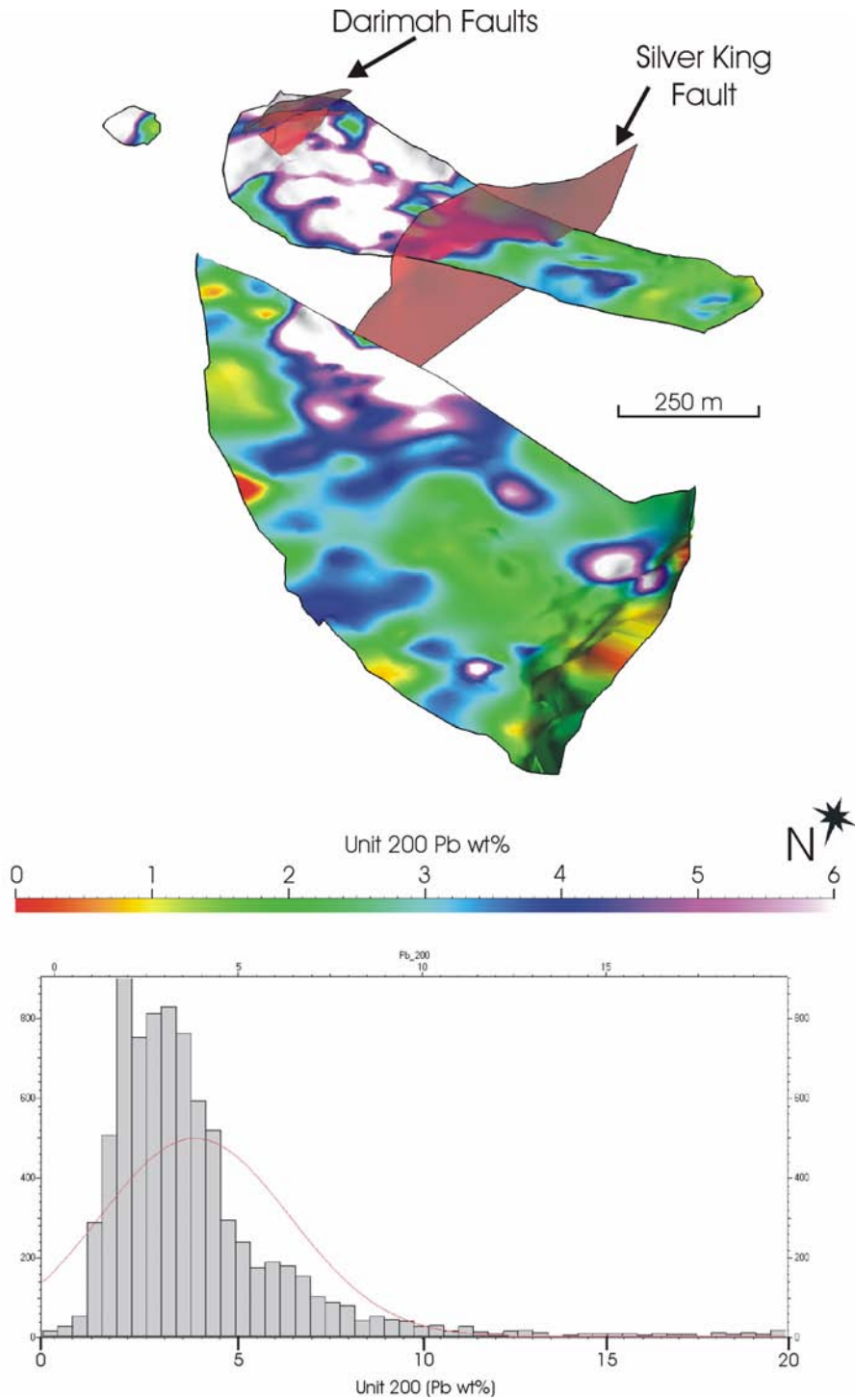


**Figure 4.11b.** 3D representation of the Pb distribution in Unit 200 of the Century deposit looking south. Note the correlation of higher grades with NE trending faults, and the spatial association of higher grade in the east (closer proximity to the Termite Range Fault). Below: Histogram displaying the Pb grade distribution of Unit 200.

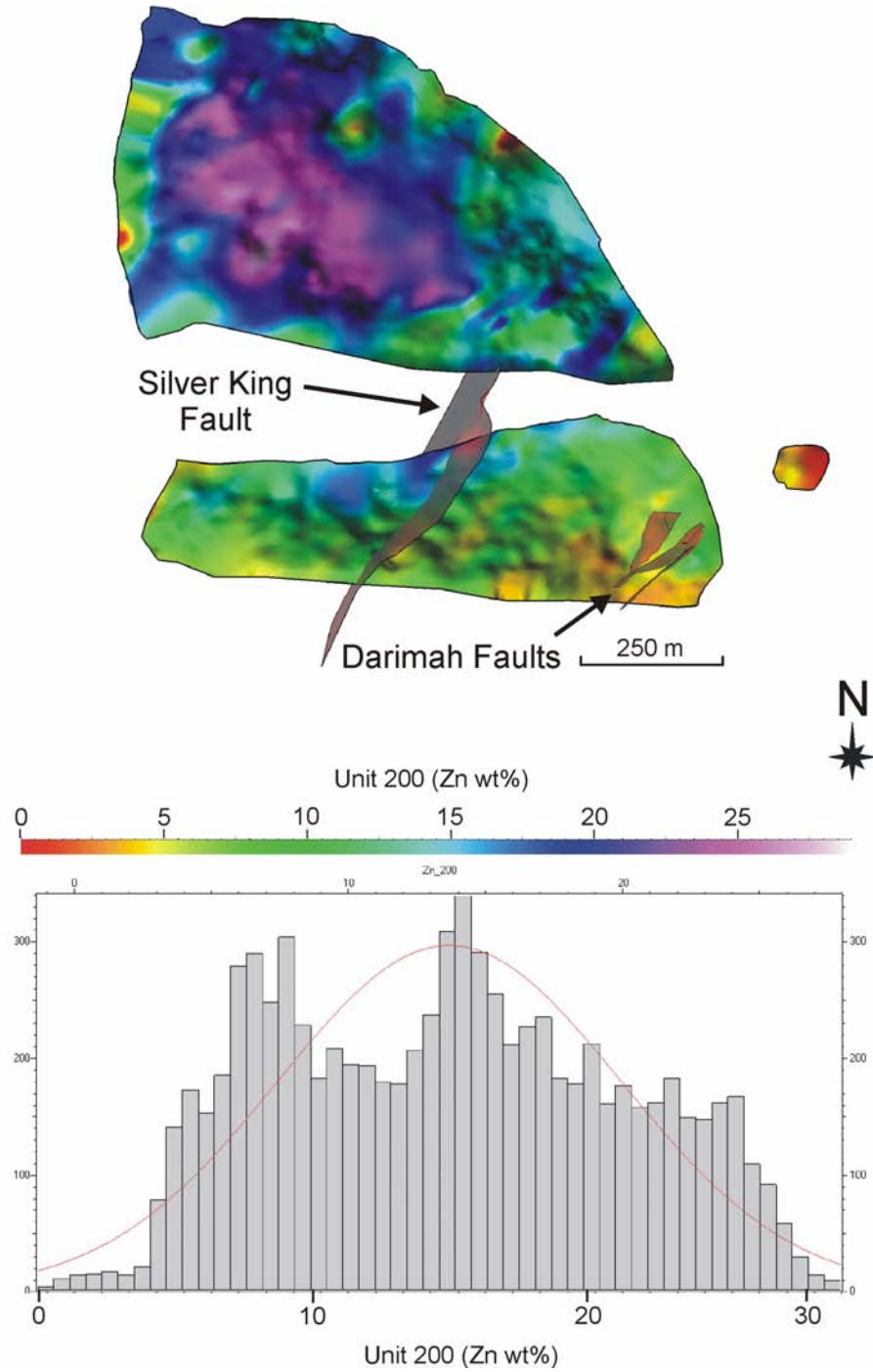


**Figure 4.12a.** 3D representation of the Zn distribution in Unit 200 of the Century deposit looking north. Note the correlation of higher grades of Zn projecting a NE trend, and the spatial association of higher grade in the west (distal to the Termite Range Fault). Below: Histogram displaying the Zn grade distribution of Unit 200.

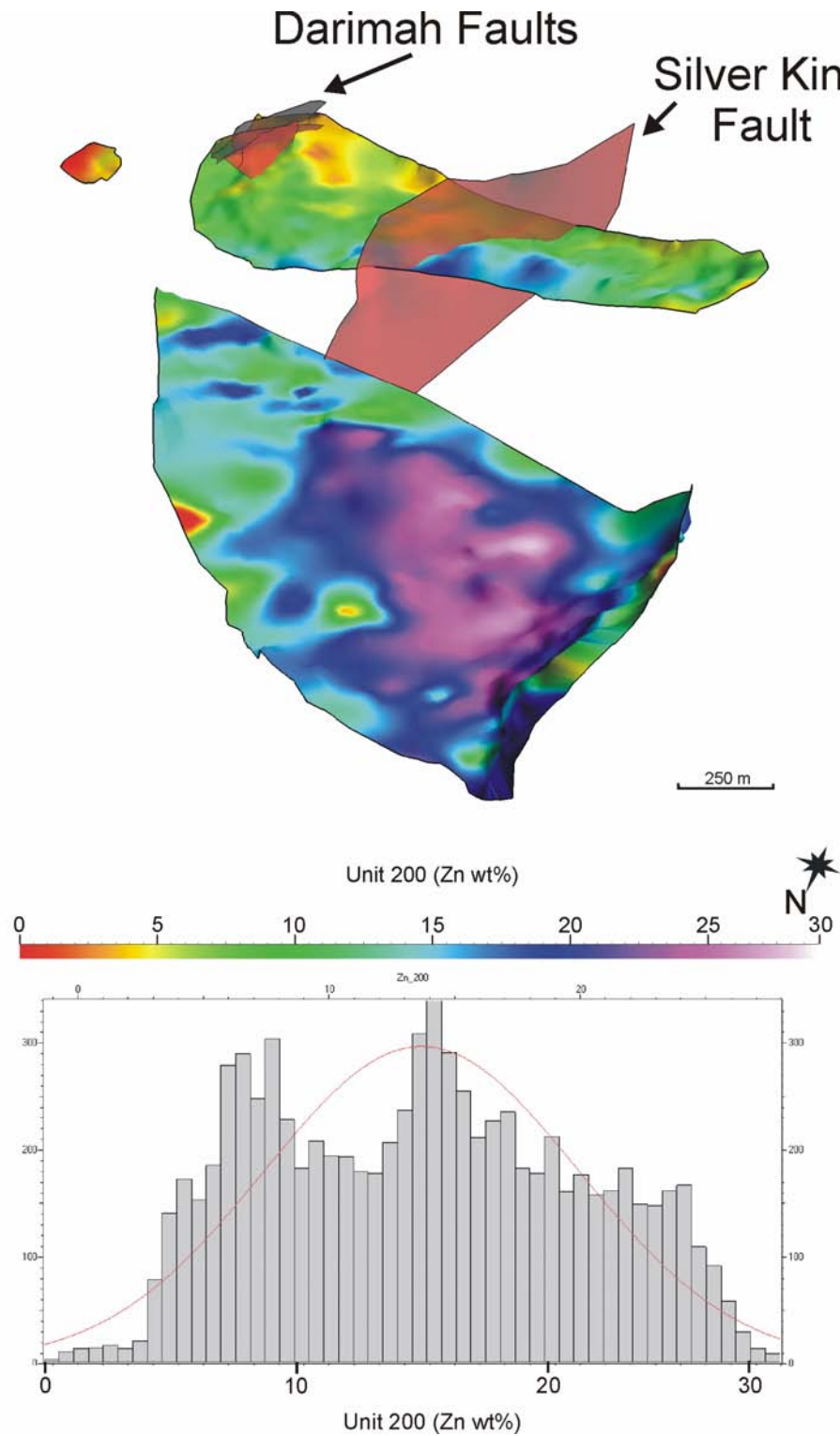


**Figure 4.12b.** 3D representation of the Zn distribution in Unit 200 of the Century deposit looking south. Note the correlation of higher grades of Zn projecting a NE trend, and the spatial association of higher grade in the west (distal to the Termite Range Fault). Below: Histogram displaying the Zn grade distribution of Unit 200.

1. Overall zoning of ore and gangue mineral assemblages
2. The lack of any complex silicate- or barite-bearing assemblage indicative of exhalite facies anywhere within the (preserved) deposit stratigraphy.
3. The consistent stratigraphic thickness of shale horizons which host ore, regardless of total sulphide content or grade of mineralisation.
4. The transgressive nature of mineralisation at the overall scale of the deposit.
5. The intimate associations of siderite, sulphides, and pyrobitumen at microscopic scale.
6. Progressive timing relationships of silica mobility, siderite deposition, and sulphide deposition relative to compaction and dissolution fabrics of the host sequence.

To support his interpretation Broadbent (1999) describes a distinct relationship of sphalerite with pyrobitumen and further divides this relationship into upper and lower units within the mineralisation to underline the influence of the hydrocarbon reservoir phases on textural aspects of mineralisation. The lower part of the mineralised sequence contains 'porous sphalerite' (see Broadbent 1999 for definition) which has a fine grained steel-grey appearance and a close association with pyrobitumen. In contrast, the upper part of the mineralised sequence is predominantly non-porous sphalerite consisting of almost pure

sphalerite bands ranging from 0.2 to 5 mm in thickness. He concluded that a hydrocarbon source/reservoir represented a chemical trap for the mineralisation and contained an oil/gas interface that produced the different sphalerite textures. Cooke *et al.*, (2003) noted, however, that both porous and non-porous sphalerite were interbanded throughout the deposit, although the proportions changed according to Broadbent's (1999) gross zonation. Broadbent *et al.* (1996 ;1998), Broadbent, (1999) and Ord *et al.* (2002) also suggest that the hydrocarbon reservoir was overpressurised at the time of mineralisation with consequent hydrofracturing and brecciation considered as main processes involved in fluid migration, metal leaching and deposition. Suggested metal sourcing for the Century system was related to clay transformation reactions from deeper units in the Lawn Hill Formation, and the conversion of sulphate to sulphide for metal precipitation as a result of thermochemical sulphate reduction (TSR) as the units passed through the 'oil window'.

#### **4.6 Deformation and Fluid Flow**

Relationships between tectonic or geological settings and fluid flow are important in understanding potential sources and fluid pathways responsible for the formation of ore deposits. Common drivers for fluid migration include 1) topographic relief 2) 'squeegee' effects during thrusting and 3) deformation induced flow. The important effect of topographic relief and hydraulic head gradients has been well documented (e.g. Toth, 1962, 1963; Garven and Freeze, 1984a, Nesbitt and Muehlenbachs, 1989) and has been proposed as a significant hydrodynamic process with implications for long distance lateral fluid flow (e.g. Garven, 1985 – Mississippi Valley Type (MVT) deposits). Oliver

(1986) described the role of thrusting and as a significant process in driving fluid flow in continental margins (the “squeegee” model), and in particular enabling lateral flow and the potential mixing of deep seated and surficial fluids in a contractional setting. Several authors have discussed at length the importance of deformation induced fluid flow (e.g. Etheridge *et al.*, 1983, 1984; Cox, 1999; Ord and Oliver, 1997), which has a major influence over direction and rates of flow.

Compressional environments and inversion of compacted sedimentary basins typically lead to overpressurisation of pore fluids and upward fluid flow (e.g. Bethke, 1985; Upton, 1998) and Sibson (1987) has also linked upward flow and overpressurisation to fault valve activity. In extensional environments however, downward migration of fluids has been linked to the development of underpressure or where interconnectivity of fractures allows deep penetration of surface derived fluids (e.g. Nesbitt and Muehlenbachs, 1989; McLellan *et al.*, 2004), and also in convection cells (Simms & Garven, 2004). Broadbent (1999) considers overpressurisation as a primary mechanism for layer parallel fracturing, which allowed fluids to infiltrate the shale units and hence resulting in mineralisation. The majority of petroleum literature considers shale units to act as seals or caps, thus trapping fluids in aquifers such as sandstone. Broadbent (1999), however, concludes that the chlorite rich sandstone unit has acted as a seal and enabled overpressure in the shale unit below. He suggested that mechanically induced permeability of an otherwise low permeability unit, enabled lateral infiltration of metal rich fluids, which may have been transported up fault structures such as the TRF. Ord *et al.* (2002) presented coupled

mechanical fluid flow and chemical models for formation of the Century deposit, based primarily on Broadbent's (1999) interpretation. The main argument for these models, in a mechanical sense, is the preferential permeability assigned to the shale units, which reach a higher permeability than the faults transporting the mineralising fluids. In the context of the Century deposit, this leads to two potential scenarios for migration of fluids in relation to the genetic models presented previously, a syn-sedimentary/early diagenetic model and a syn-tectonic model; however lateral flow from major fluid pathways remains an issue. Here we aim to test possible scenarios for infiltration of fluids responsible for mineralisation by coupled deformation and fluid flow numerical simulations, by examining the potential types of faulting (growth faults and fault reactivation) present during the two most likely periods for mineralisation of the Century Zn-Pb-Ag deposit. The models within this study examine the potential for lateral flow within the shale units during extension and compression, and also the permeability contrasts required to achieve this. The relationship between upward or downward migrating fluids and lateral fluid migration is also tested.

#### **4.7 Numerical Modelling**

The numerical models presented here are based on a coupled deformation and fluid flow approach, where mechanical deformation is the main driving force for fluid migration. To gain a better understanding and useful results, questions regarding the system under investigation must be posed. The main questions asked in this study are:

1. What were the pathways that controlled the location of favourable sites for mineralisation?
2. What geological conditions were favourable for lateral fluid flow?
3. What tectonic regimes were active and suitable for lateral flow?
4. What role does overpressurisation have in controlling fluid flow and mineralisation?

#### 4.7.1 FLAC (Fast Lagrangian Analysis of Continua)

FLAC is a two-dimensional explicit finite difference modelling program, suitable for simulating the behaviour of geological materials that undergo plastic flow during yield (see Chapter 2). FLAC has been applied to many geological problems in Australia (e.g. Ord, 1990,1991a,b; Ord & Oliver, 1997; Oliver *et al.*, 2001; Upton *et al.*, 1995, 1998; Upton, 1998; Zhang *et al.*, 1996a,b, 2003; McLellan, 2001; McLellan *et al.*, 2004; Schaub & Zhao, 2002). Materials are represented by zones that form a grid, which can be adjusted by the user to fit the geometry of the problem to be solved. Each zone within the grid can be prescribed properties (both elastic and plastic) and the zones behave according to a prescribed linear or non-linear stress/strain law as a response to applied forces. The material is allowed to yield and flow and deform whilst run in large-strain mode, and when in a coupled scenario, fluid allows interaction with and influence over this deformation. For a full description of FLAC see Chapter 2.

#### 4.7.2 Sensitivity of Strain Rates

As a result of rigorous sensitivity testing, strain rates within the FLAC models were found to be a critical parameter in determining not only pore pressure and

hydraulic head distribution but also plasticity failure and ultimately fluid flow. Simulating deformation in FLAC can be done by either applying a boundary stress or a boundary velocity. In a Mohr-Coulomb constitutive relationship in FLAC there is no inherent time dependence associated with the mechanical steps, hence velocity boundary conditions are prescribed as a length per time step relationship, with real time only being associated with fluid steps in a coupled model. The unbalanced force in FLAC is a measure of equilibrium within the model grid and can represent a condition where we have steady state plastic flow. If the ratio of unbalanced force to internal forces within the model is large e.g. >1% then the boundary velocities are considered to be too great. In extensional deformation for example, we can check the effects of boundary velocities by examining the bulk extension rates of the model. This is done by extracting information at specific grid points within the mesh and calculating the distance of movement and dividing this by the constitutive time of the model at this point. Typical values for geologically acceptable strain rates range from  $1.00\text{e-}13$  to  $1.00\text{e-}17 \text{ sec}^{-1}$  (e.g. Tadakazu, 2001; Pietrantonio & Riguzzi, 2004) and laboratory studies have shown strain rates as high as  $1.00\text{e-}9 \text{ sec}^{-1}$  (Turcotte & Schubert, 2002). If strain rates are too slow then we have no plastic flow within the model, and if they are too great we have inertia effects and increased rates of deformation and fluctuating velocity histories. All models presented here have been tested for acceptable limits of bulk extension/shortening rates where applicable.

### 4.7.3 Conceptual Models

Prior to any numerical modelling, an important step is to define the conceptual models and address the main questions posed in relation to the system under investigation. In this study two conceptual models are introduced in relation to the two possible fluid flow scenarios previously discussed, and linked to the tectonic setting that controls them. The conceptual models (Fig. 4.13ab) consist of a 400 m by 400 m cross section representing a simplification of the mine stratigraphic intervals and the main geological components comprising the Century system (Fig. 4.14). The main aim of the constructed conceptual models is to explore the difference between a) extension and compression b) poorly consolidated materials and lithified materials (i.e. at depth) and c) permeability contrasts and hydrofracturing that may provide the potential for fluid to infiltrate the shale units in the Century system. Both models (extension and contraction) are fully saturated with fluids, and pore pressure is initialised in Model 1 at hydrostatic, which represents conditions commensurate with early basin formation, and an overpressured zone is initialised in Model 2, which represents conditions commensurate with a later stage contraction. All physical properties are given in Table. 4.2.

Attempts were made to numerically model a syngenetic scenario, by prescribing all materials low values of elastic properties and in particular low cohesion values. However, unconsolidated sediments may not behave in a Mohr-Coulomb sense in reality (i.e. they may be poro-elastic, not elastic-plastic or poro-plastic). Not only might the constitutive properties be inappropriate, FLAC cannot simulate the effect of ongoing sedimentation. Finally, lowering the

cohesion values produced extreme grid failure at low strains, confirming that FLAC was inappropriate for modelling this scenario. Thus, we consider only two subsurface genetic models, extension during basin evolution (diagenesis) and contraction during orogeny (epigenesis).

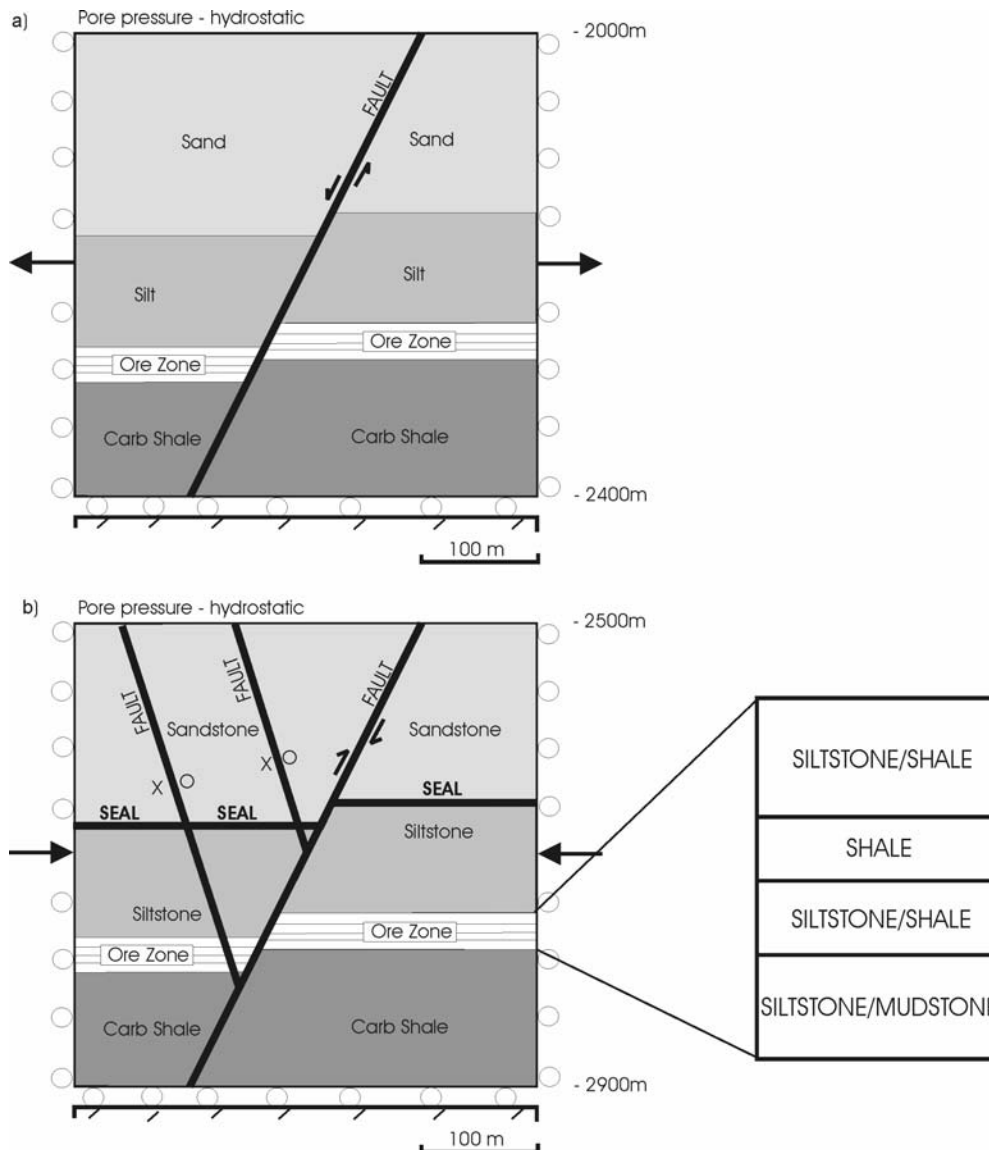


**Figure 4.13.** Conceptual models for, **a)** Model 1 representing soft sediments and extensional deformation and **b)** Model 2 representing lithified sediments and later stage basin evolution. Ore Zone stratigraphy indicated. Model 2 has an overpressured zone applied in models 2b-d below the sandstone-siltstone interface at lithostatic pressures with the sandstone unit acting as a seal.

**Table 4.2.** Physical properties for materials for Models 1 and 2.

Model	Density (kg/m <sup>3</sup> )	Bulk modulus (Pa)	Shear modulus (Pa)	Cohesion (Pa)	Friction angle (°)	Dilation angle (°)	Permeability (m <sup>2</sup> )
<b>Model 1a</b>							
Sand	1600	8.33e6	1.88e7	3.0e3	30	5	1.00e-12
Silt	1700	3.0e6	7.5e6	3.0e3	25	5	1.00e-13
All Shale	1800	3.33e5	5.01e6	1.0e3	20	2	1.00e-14
Silt / Shale	1750	8.0e5	7.0e6	2.0e3	22	3	5.00e-13
Silt / Mud	1750	8.0e5	9.5e5	2.0e3	22	3	2.00e-14
Fault	1600	3.33e5	7.0e4	1.0e3	20	5	1.00e-12

Model	Density (kg/m <sup>3</sup> )	Bulk modulus (Pa)	Shear modulus (Pa)	Cohesion (Pa)	Friction angle (°)	Dilation angle (°)	Permeability (m <sup>2</sup> )
<b>Model 1b</b>							
Sand	1600	8.33e6	1.88e7	3.0e3	30	5	1.00e-12
Silt	1700	3.0e6	7.5e6	3.0e3	25	5	1.00e-13
Carbonaceous Shale	1800	3.33e5	5.01e6	1.0e3	20	2	1.00e-14
Ore Shale	1800	3.33e5	5.01e6	1.0e3	20	2	1.00e-12
Silt / Shale	1750	8.0e5	7.0e6	2.0e3	22	3	5.00e-13
Silt / Mud	1750	8.0e5	9.5e5	2.0e3	22	3	2.00e-14
Fault	1600	3.33e5	7.0e4	1.0e3	20	5	1.00e-12

Model	Density (kg/m <sup>3</sup> )	Bulk modulus (Pa)	Shear modulus (Pa)	Cohesion (Pa)	Friction angle (°)	Dilation angle (°)	Permeability (m <sup>2</sup> )
<b>Models 2a-b</b>							
Sandstone	2400	2.68e10	7.0e9	2.7e7	27	4	1e-15 to 1e-19
Siltstone	2450	1.56e10	1.08e10	3.47e7	25	4	1.00e-16
Ore Shale	2500	8.8e9	4.3e9	3.84e7	14	2	1.00e-19
Carbonaceous Shale	2500	8.8e9	4.3e9	3.84e7	14	1	1.00e-19
Siltstone / Shale	2500	1.0e10	7.5e9	3.6e7	23	2	5.00e-16
Siltstone / Mudstone	2600	1.0e10	7.5e9	3.6e7	23	2	1.00e-18
Fault	2300	4.70e9	4.30e9	8.00e5	30	5	1.00e-14

note: Model 2b decreases permeability of Sandstone to 1.00e-19 and overpressure is applied

Model	Density (kg/m <sup>3</sup> )	Bulk modulus (Pa)	Shear modulus (Pa)	Cohesion (Pa)	Friction angle (°)	Dilation angle (°)	Permeability (m <sup>2</sup> )
<b>Models 2c-d</b>							
Sandstone	2400	2.68e10	7.0e9	2.7e7	27	4	1e-15 to 1e-19
Siltstone	2450	1.56e10	1.08e10	3.47e7	25	4	1.00e-16
Ore Shale	2500	8.8e9	4.3e9	3.84e7	14	2	1.00e-15
Carbonaceous Shale	2500	8.8e9	4.3e9	3.84e7	14	1	1.00e-19
Siltstone / Shale	2500	1.0e10	7.5e9	3.6e7	23	2	5.00e-16
Siltstone / Mudstone	2600	1.0e10	7.5e9	3.6e7	23	2	1.00e-18
Fault	2300	4.70e9	4.30e9	8.00e5	30	5	1.00e-14

note: Model 2b has an additional yield function applied

#### 4.7.4 Conceptual Model 1

Conceptual model 1 (Fig. 4.13a) displays a simplified version of the mine stratigraphic units subdivision adopted after Kelso & Edge (unpublished report) (see Fig 4.7), and is cut by a normal fault, which represents the Termite Range

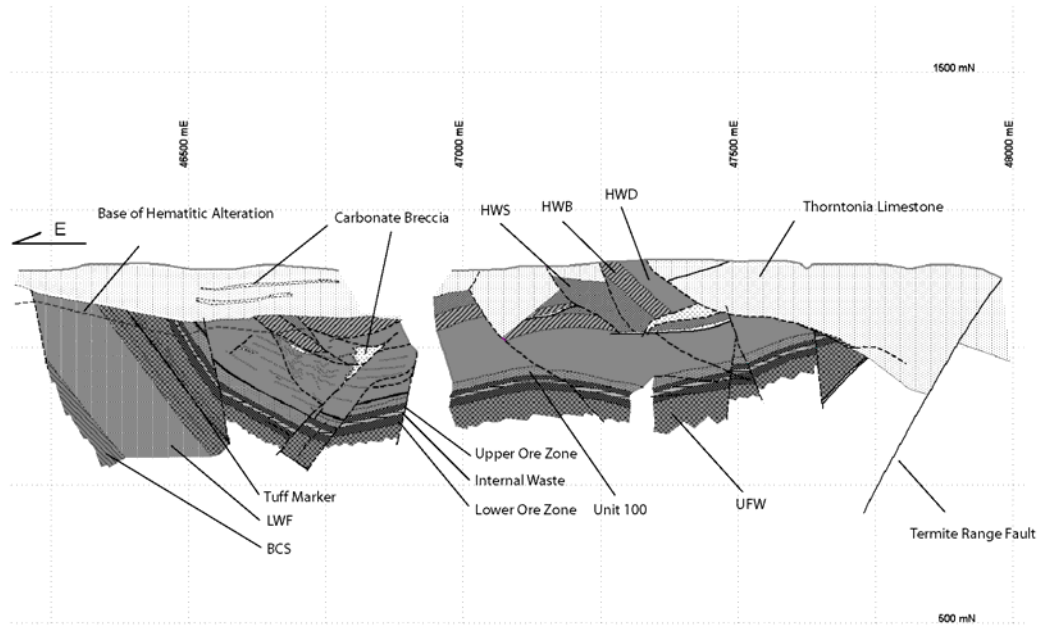


**Figure 4.14.** Cross section of the Century deposit looking south, displaying the main structural features and stratigraphic elements. Note the Termité range Fault and its spatial relationship to parasitic faults to the east.

Fault during and soon after sedimentation. Extensional deformation is applied to the model. The conceptual model represents an early diagenetic scenario in which sediments are considered to be semi-lithified, and here we are testing the effects of deformation and permeability contrasts on fluid flow.

To understand what permeability conditions are required to allow fluids to migrate through rock hosting the mineralisation, we tested two extensional models:

- **Model 1a** represents semi-lithified sediments and shale units (the most favourable host rock for Zn-Pb ore) with a low permeability value.
- **Model 1b** represents the same stratigraphy but the shales have higher permeability values to evaluate the permeability contrasts

required to obtain significant fluid flow through them, and hence potential mineralisation.

#### 4.7.5 Conceptual Model 2

The second conceptual model (Fig. 4.13b) is similar to Model 1; however two additional parasitic faults have been added to reflect the evolution of the Termite Range Fault, which appears to have been reactivated during syn- to post-tectonic deformation. The stress applied to this second conceptual model is consistent with compression. In this case it is intended to represent a later stage of evolution of the Century system in which fluids are more tectonically driven with major topographic and deformation induced flow. Within this compressional model we test four alternative scenarios:

- **Model 2a** has regular rheological properties assigned for the appropriate rock types;
- **Model 2b** then assigns a low permeability to the sandstone unit (as described earlier) with a decrease in permeability from  $1\text{e-}15$  to  $1\text{e-}19\text{ m}^2$ , and the role of overpressure is investigated following the hypothesis proposed by Broadbent *et al* (1998);
- **Model 2c** is also initialised with an overpressured area at the siltstone/sandstone boundary in correspondence with the interpretation of Broadbent (1999), and has an increase in permeability of the shale units from  $1\text{e-}19$  to  $1\text{e-}15\text{ m}^2$ ; and
- **Model 2d** introduces an additional function that increases permeability by 10% within the model when materials are at yield

and returning to or retaining their original permeability when not at yield. This function allows deformation induced permeability to be investigated in the shale units and other rocks and faults.

## 4.8 Results

Initial models (Model 1a and 1b) were constructed with assigned material properties conducive to semi-lithified sediments (i.e. relatively low cohesion), and as a consequence, the model grid fails shortly following 2% extension. However, initial results during early periods of extension in these models are presented. Models 2a-d represent lithified rocks (higher cohesion) and are deformed to around 12% shortening. The results of all models are presented below.

### 4.8.1 Model 1a (extension, semi-lithified sediments, low permeability shale)

At very early stages of extension (1%) fluid flow is primarily focussed within the fault, sandstone and silt layers, due to higher permeability of these units (Fig. 4.15a). Local pore pressure gradients intensify fluid flow with maximum flow velocities of  $1.44\text{e-}8 \text{ m/s}^{-1}$  ( $0.45 \text{ m/yr}^{-1}$ ). On closer inspection fluid can be seen to be drawn from the fault into the siltstone layers with an overall flow direction from left to right, however little to no flow is evident within the shale as a result of the low permeability values assigned to these units (Fig. 4.15b). At around 2% extension pore pressure has decayed slightly, displaying supra-hydrostatic pore pressures and a sub-hydrostatic gradient (Fig. 4.16a). Fluid flow is more evident within the more permeable units of sandstone, siltstone and within the fault, with increased flow velocities of  $1.704\text{e-}8 \text{ m/s}^{-1}$  ( $0.54 \text{ m/yr}^{-1}$ ) (Fig. 4.16b).

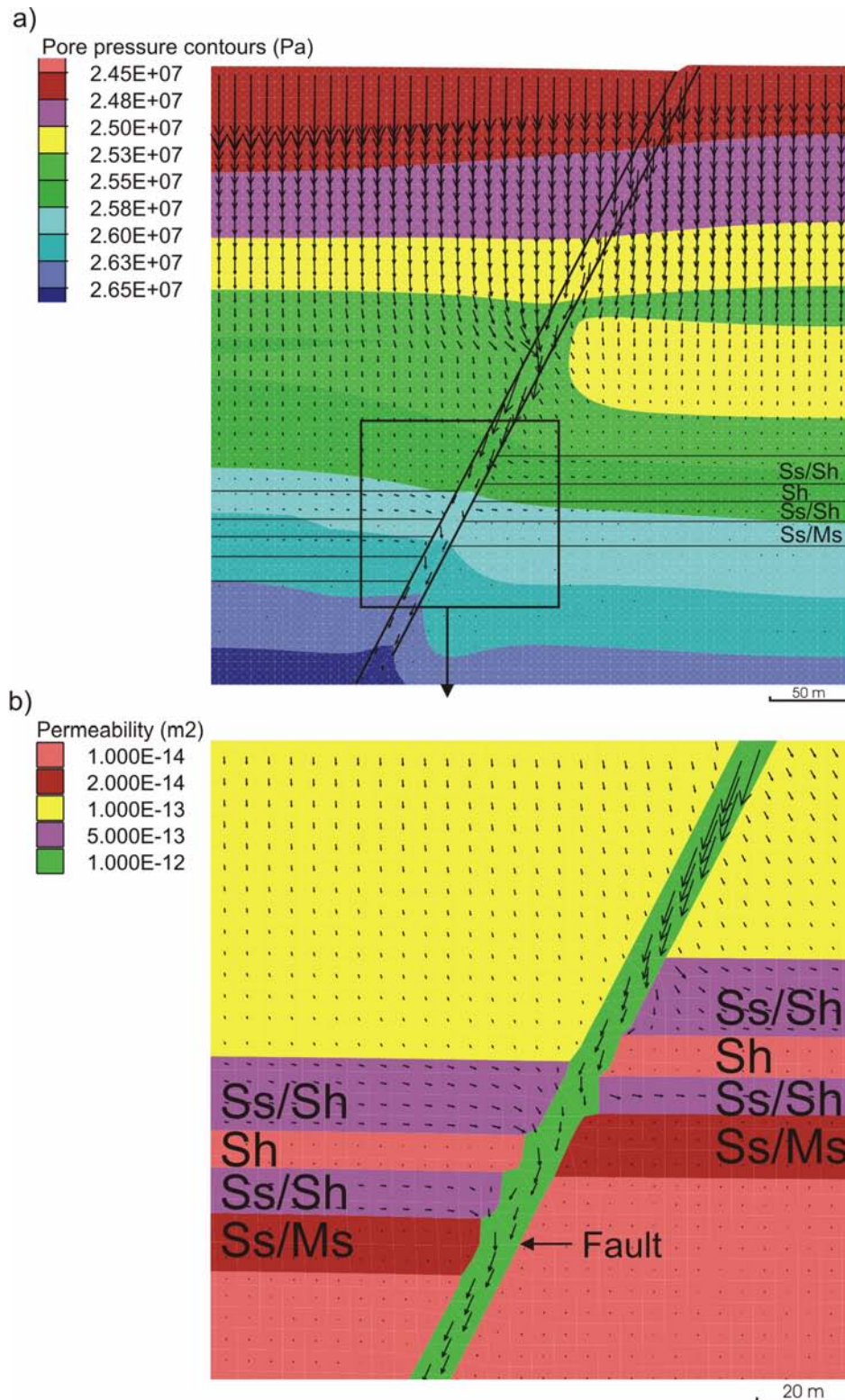


**Figure 4.15.** Model 1a showing plots of **a)** pore pressure contours and Darcy fluid flow vectors for Model 1a at 1% extension, displaying predominant downward migration of fluids within the more permeable fault and sediments, **b)** magnified plot of the ore zone displaying permeability values and flow vectors. Note the lack of fluid flow within the shale units.

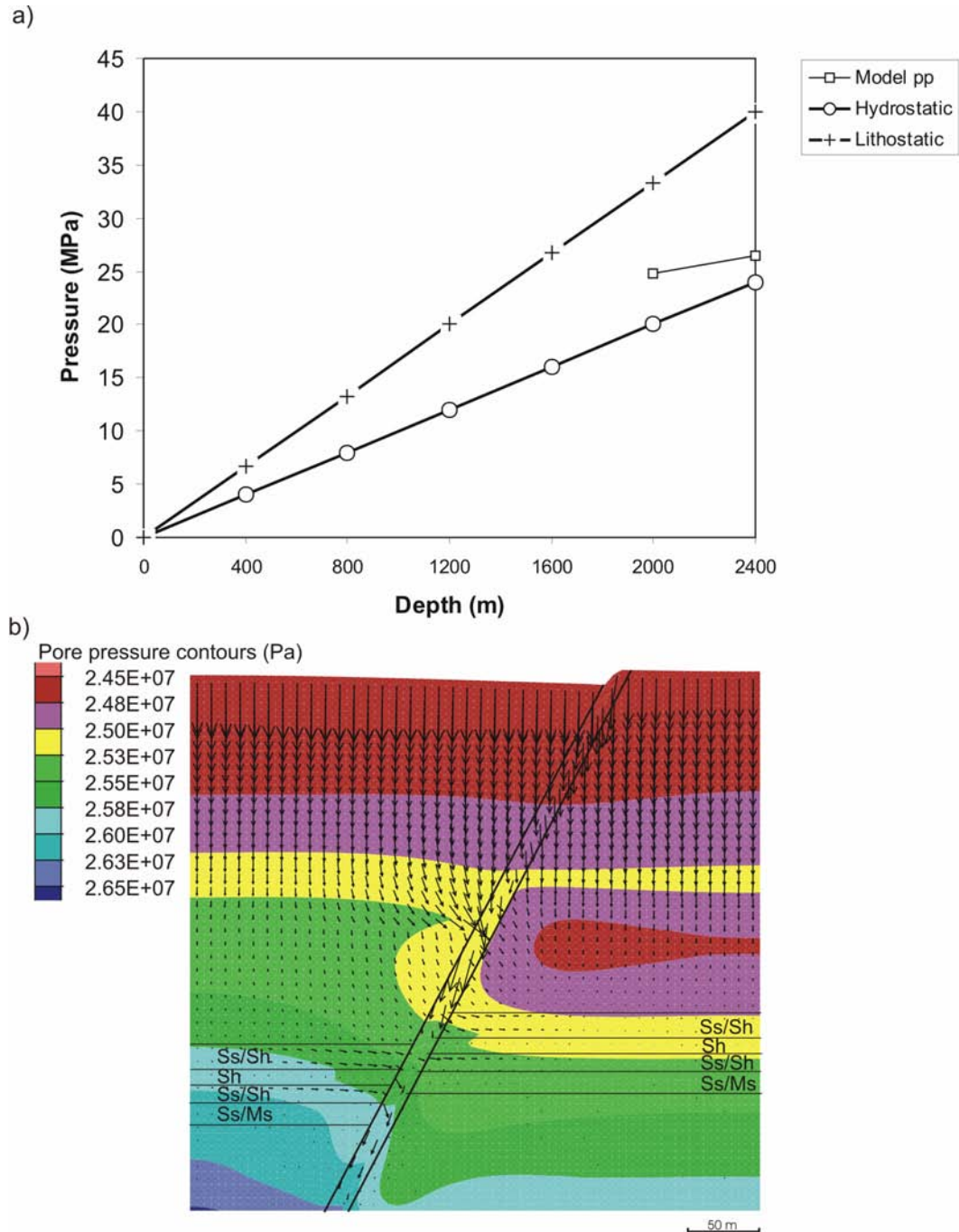


**Figure 4.16.** Model 1a at around 2% extension, **a)** depth v pressure graph illustrating pore pressure decay due to extension, displaying supra-hydrostatic pore pressures and a sub-hydrostatic gradient, **b)** plot of pore pressure and Darcy fluid flow vectors indicating an overall downward trend of fluid flow within the fault and lateral flow in the more permeable siltstone layers.

As a result of the low values in elastic properties of the sediments, the model grid fails soon after 2% deformation. If ore deposition occurred in zones of high fluid flux, it would have been most concentrated in the faults and coarser grained sediments, according to this model.

#### 4.8.2 Model 1b (extension, semi-lithified sediments, high permeability shale)

As with Model 1a, initial extension causes perturbations in fluid flow which is primarily driven by pore pressure gradients (Fig. 4.17a). Unlike Model 1a however, strong lateral flow can be seen in the shale units due to the assigned permeability being similar to the fault and greater than the surrounding sediments (Fig. 4.17b). As pore pressure decays as a result of extension similar patterns to Model 1a are evident, with downward migrating fluid primarily within the more permeable fault and lateral flow within the stratigraphic units (Fig. 4.18). Comparative increases in fluid flow velocities to Model 1a are seen as a result of continuing deformation from 1 to 2% extension ( $1.475 \times 10^{-8} \text{ m/s}^{-1}$  to  $1.788 \times 10^{-8} \text{ m/s}^{-1} - 0.47 \text{ m/yr}^{-1}$  to  $0.56 \text{ m/yr}^{-1}$ ). According to this model, substantial fluid flow may have caused mineralisation in shales and faults. Inflow towards the fault or outflow away, along the shale layers, is dependent on detail of the geometry chosen.

In summary, the results from the simulation of semi-lithified sediments and poorly consolidated material indicate that FLAC has difficulty in modelling material of this type, due to inadequate constitutive models and grid failure. However, useful results for some models are indicated in very early stages of extension, where fluid flow is focussed within more permeable material and

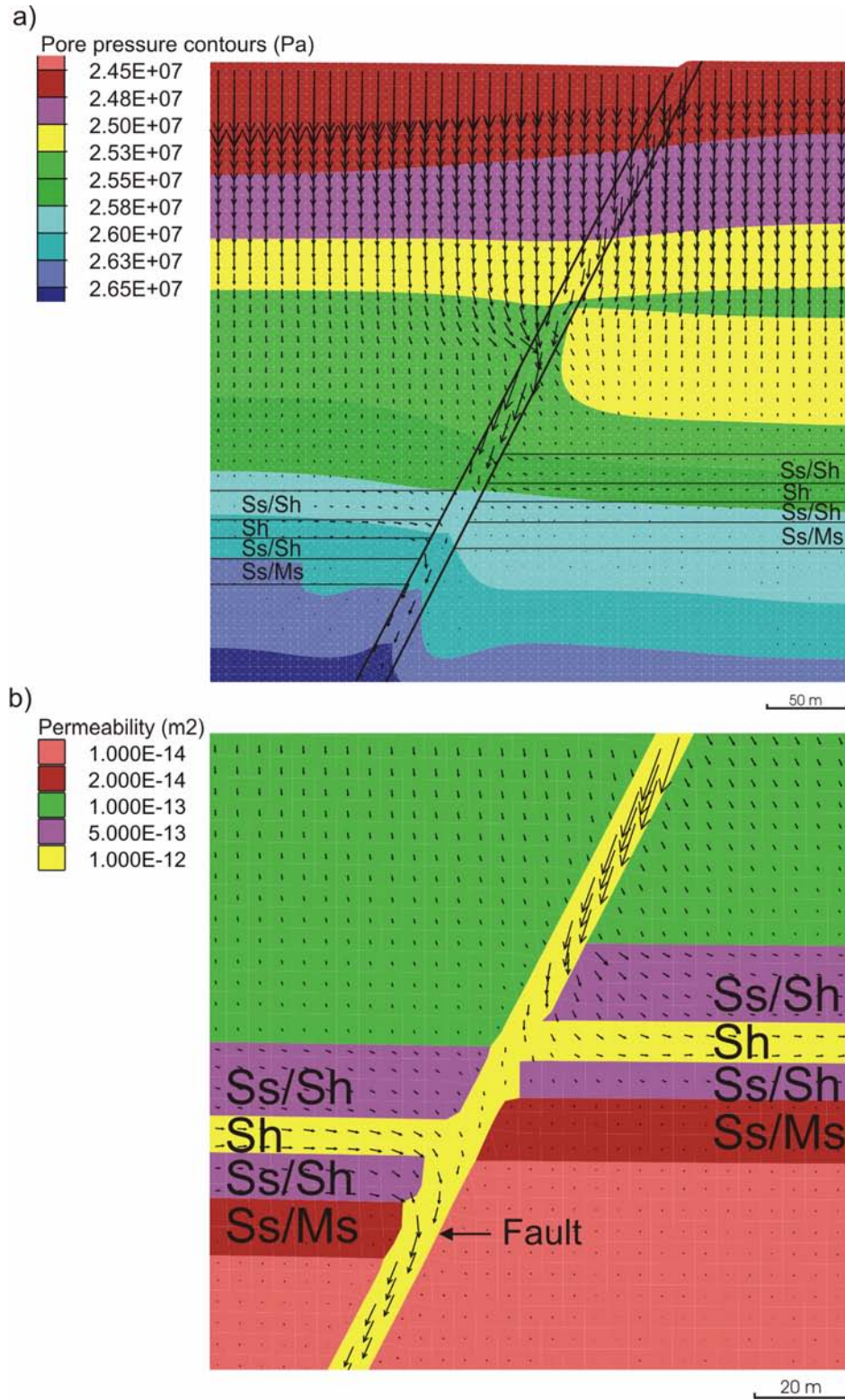


**Figure 4.17.** Plot of a) pore pressure contours and Darcy fluid flow vectors for Model 1b at 1% extension, displaying predominant downward migration of fluids within the more permeable fault and sediments, b) magnified plot of the ore zone displaying permeability values and flow vectors. Note the strong fluid flow within the shale units (yellow).

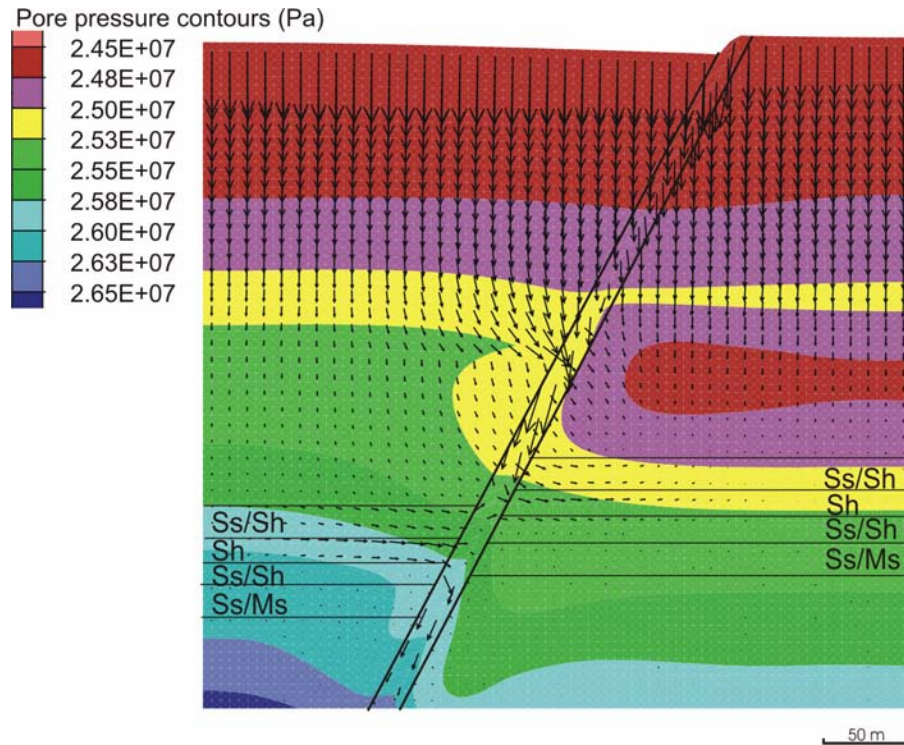


**Figure 4.18.** Plot of pore pressure contours and Darcy fluid flow vectors for Model 1b at 2% extension, displaying predominant downward migration of fluids within the more permeable fault and sediments, and strong lateral fluid flow within the shale units.

driven by initial changes in pore pressure gradients and permeability contrasts.

When the shale unit within the 'ore zone' has permeability values as high as to less than one order of magnitude lower than that of the fault, notable fluid flow is evident in shales, which may indicate the potential for a diagenetic replacement in a subsurface condition. The permeability is one of the primary factors that control fluid flow, during early stages of diagenesis.

#### 4.8.3 Model 2a (contraction, low permeability shale)

A significant difference from the previous models discussed is that within this model fluid is focussed within the fault in an overall upward migration path (Fig. 4.19a). Initial compression results in an increase in pore pressure (up to 75 MPa) within the model that forces fluid up the more permeable fault. Pore

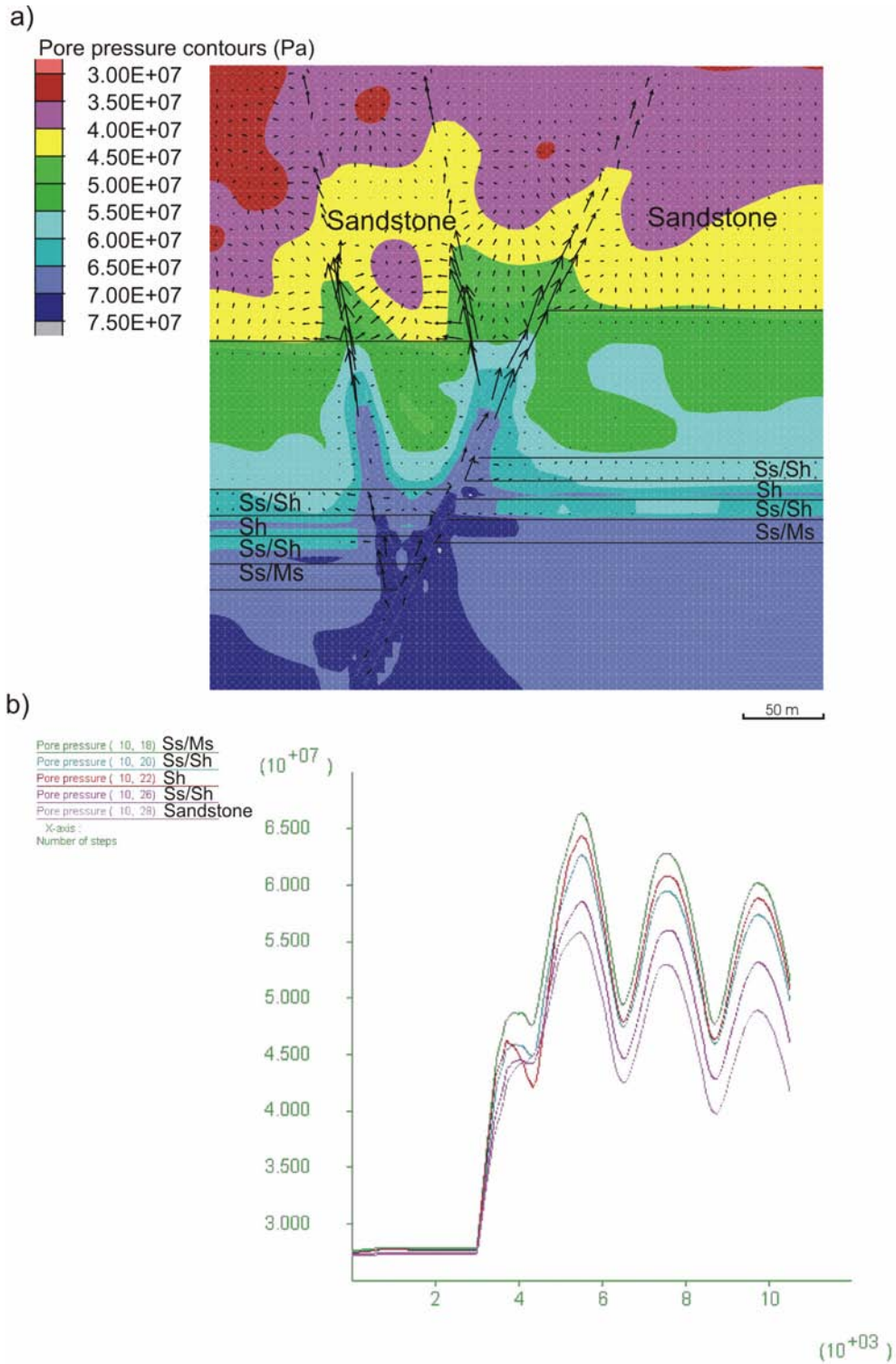


**Figure 4.19.** Early stages of compression for Model 2a, **a)** plot of pore pressure and Darcy fluid flow vectors indicating an overall upward trend of fluid flow within the fault and very limited lateral flow in the permeable siltstone layers **b)** graph of pore pressure v time, illustrating pore pressures in all units from the over zone to the sandstone. Note the cyclic behaviour of pore pressure due to deformation.

pressure histories were monitored throughout the model simulation, which displays cyclic variations due to deformation and the system response (Fig. 4.19b). The shale unit contains isolated areas of high pore pressure in comparison to other units as a result of the shale's low permeability and low dilation angle (Fig. 4.20a). Areas of dilation are observed within the model as deformation progresses (10% shortening), in particular to the left of the main fault, although focussing of fluids remains concentrated within the more permeable faults (Fig. 4.20b). The faults, however, show local contractional behaviour and limit fluid flow nearer the top of the model. Due to the limited permeability and lack of dilation in the shale units, no significant fluid flow is noted within them (Fig. 4.21).

#### 4.8.4 Model 2b (contraction, low permeability shale and sandstone, with overpressure)

In simulating the sandstone unit at the top of the model as a 'cap' or 'seal' to the system, the permeability of this unit is reduced. An overpressure is applied at the base of the sandstone unit and over the ore zone in agreement with the model proposed by Broadbent (1998) and Ord *et al.* (2002), as the chlorite rich sandstone has been interpreted as a seal in the system. As deformation commences, fluid is forced through the seal and into the faults penetrating above the sandstone (Fig. 4.22a-d). As compression progresses (3% shortening) strong upward flow driven by pore pressure gradients is seen within the fault structures (Fig. 4.23a). At around 5% shortening, dilational zones are prominent within the middle regions of the model and appear to be closely related to areas bounding faults (Fig. 4.23b). As deformation continues fluid

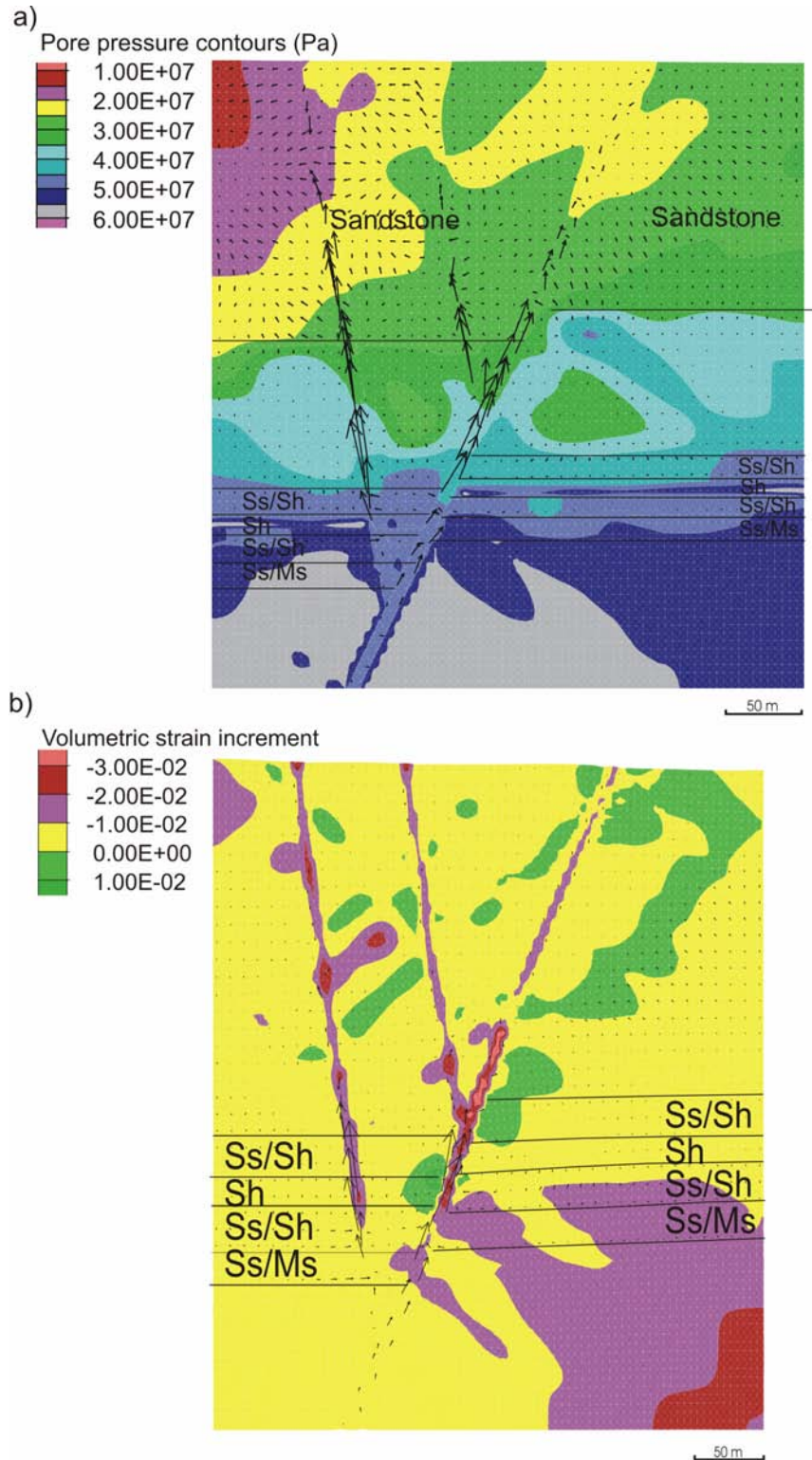


**Figure 4.20.** Early to late stages of compression for Model 2a, **a)** 3% compression, plot of pore pressure and Darcy fluid flow vectors indicating an overall upward trend of fluid flow within the fault and very limited lateral flow in the permeable siltstone layers **b)** 9% compression, plot of volumetric strain (dilation) and Darcy fluid flow vectors indicating an overall upward trend of fluid flow within the fault and limited lateral flow in the permeable siltstone layers. Most dilation is occurring close to the fault structures.

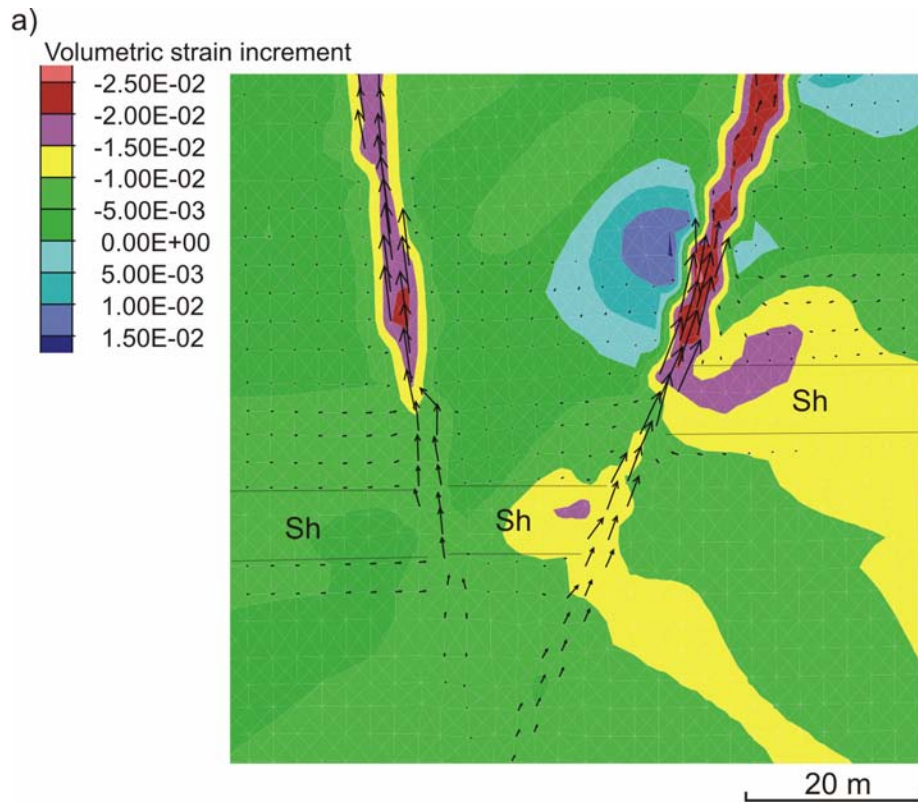


**Figure 4.21.** Late stage of compression (9%) for Model 2a, plot of volumetric strain (dilation) and Darcy fluid flow vectors indicating an overall upward trend of fluid flow within the fault and insignificant flow within the shale layers.

flow continues upwards within the more permeable faults, with lesser flow noted within the siltstone layers and no flow in the shale layers (Fig. 4.24). Dilation is prominent as a band within the centre of the model; however this has no major influence on focussed fluid flow.

#### 4.8.5 Model 2c (contraction, high permeability shale, low permeability sandstone, with overpressure)

Increasing the permeability of the shale units within the 'ore zone' has a major effect on fluid flow within this unit. At early stages of deformation (1% shortening) fluid flow is focussed in an upward direction within the more permeable faults, and lateral flow is evident from the fault into the shale units

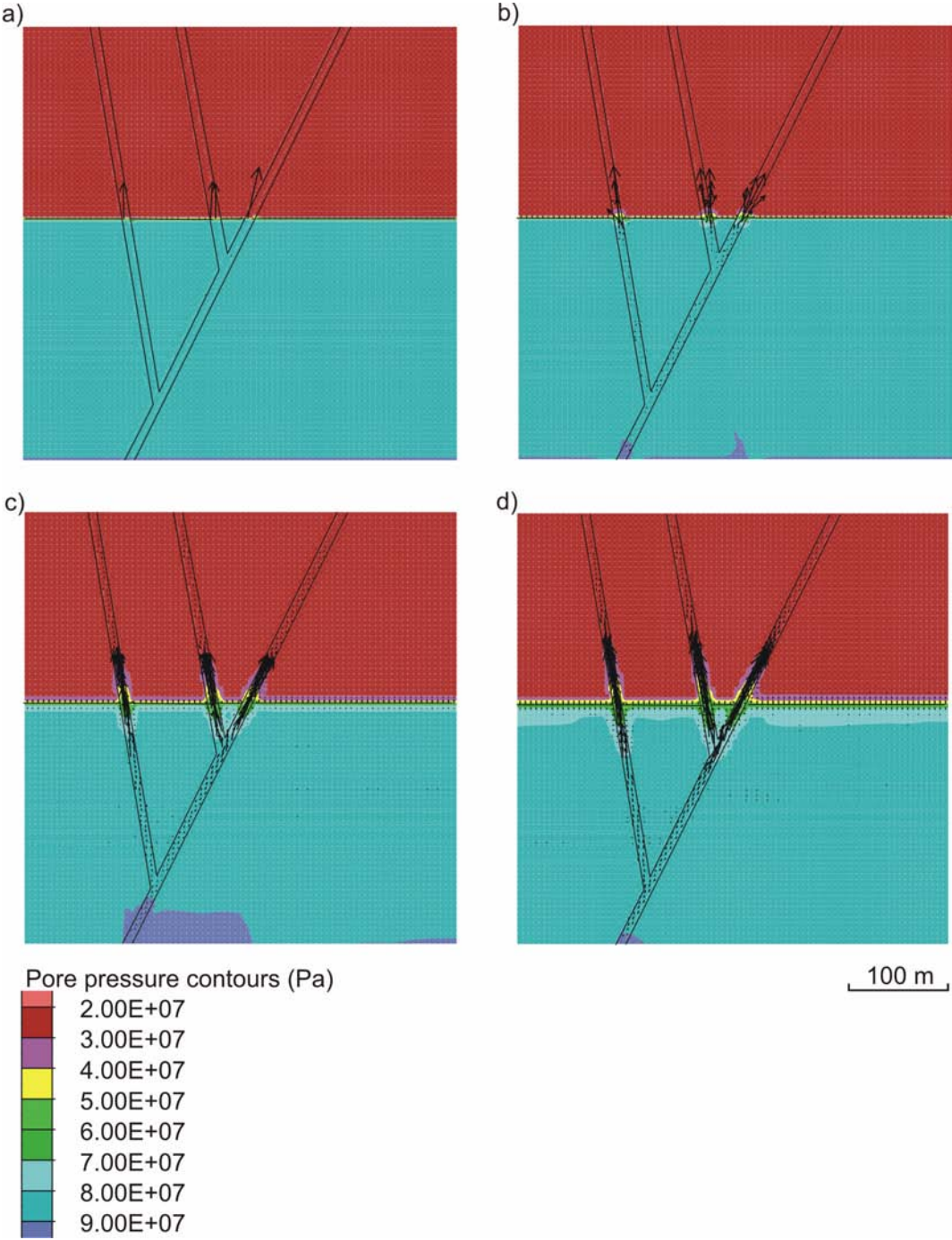


**Figure 4.22.** Model 2b at commencement of deformation and release of overpressure, a) to d) representing stages of this process showing pore pressure contours forcing fluid upwards through the fault system with no lateral fluid flow evident.

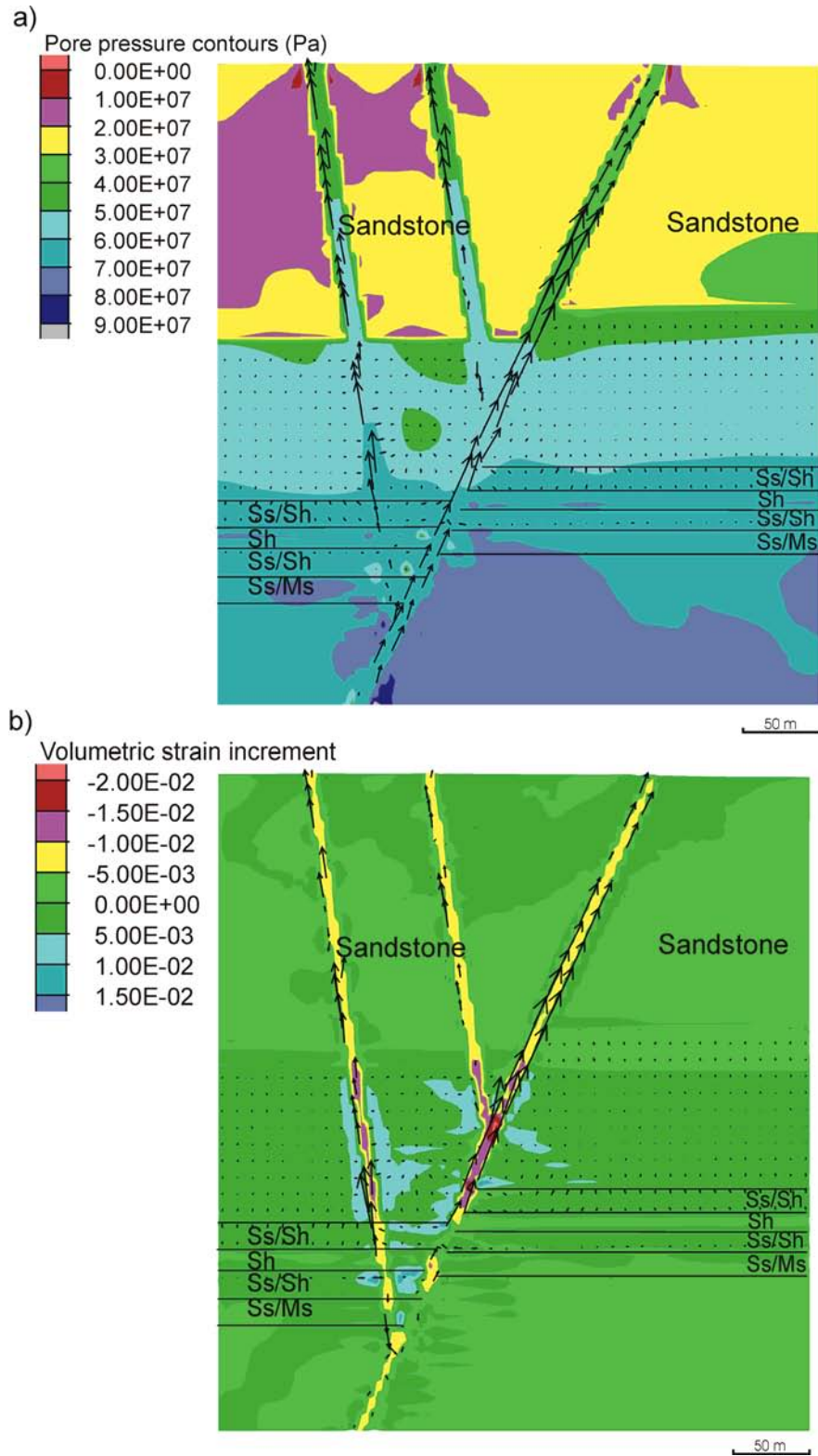


**Figure 4.23.** Model 2b at **a)** 3% deformation, displaying pore pressure contours and a strong Darcy fluid flow focussing within the fault zones and **b)** 5% deformation, plot of volumetric strain (dilation) and Darcy fluid flow vectors, displaying strong flow within the faults and minor lateral flow in the siltstone layers.

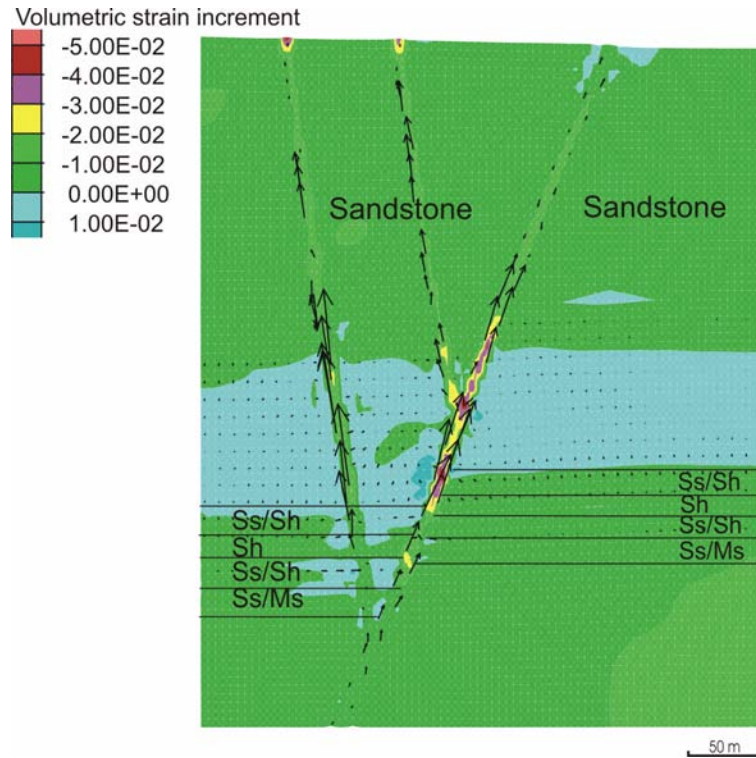


**Figure 4.24.** Model 2b at 9% compression displaying volumetric strain (dilation) and Darcy fluid flow vectors. Dilation is primarily associated with a band in the centre region of the model and around fault structures.

(Fig. 4.25a). Areas of high pore pressures are apparent from the base of the main fault (Fig. 4.25b) which is forcing fluid up the fault structures. Corresponding dilational zones are evident in close proximity to fault structures below the sandstone and siltstone interface, and in particular are found between the lower branching fault and the main fault (Fig. 4.26a). As deformation progresses, focussed flow within the shale unit is more apparent, with fluid being drawn from the shale units towards the faults. As deformation continues (5% shortening), fluid flow is preferentially focussed along the shale units and is also driven upwards through the permeable faults (Fig. 4.26b). Very limited fluid flow or dilation is seen within the sandstone, and it maintains overpressure in the units below, allowing only the fault structures to dissipate pressure up the faults. Within this model overall, pore pressure decays towards

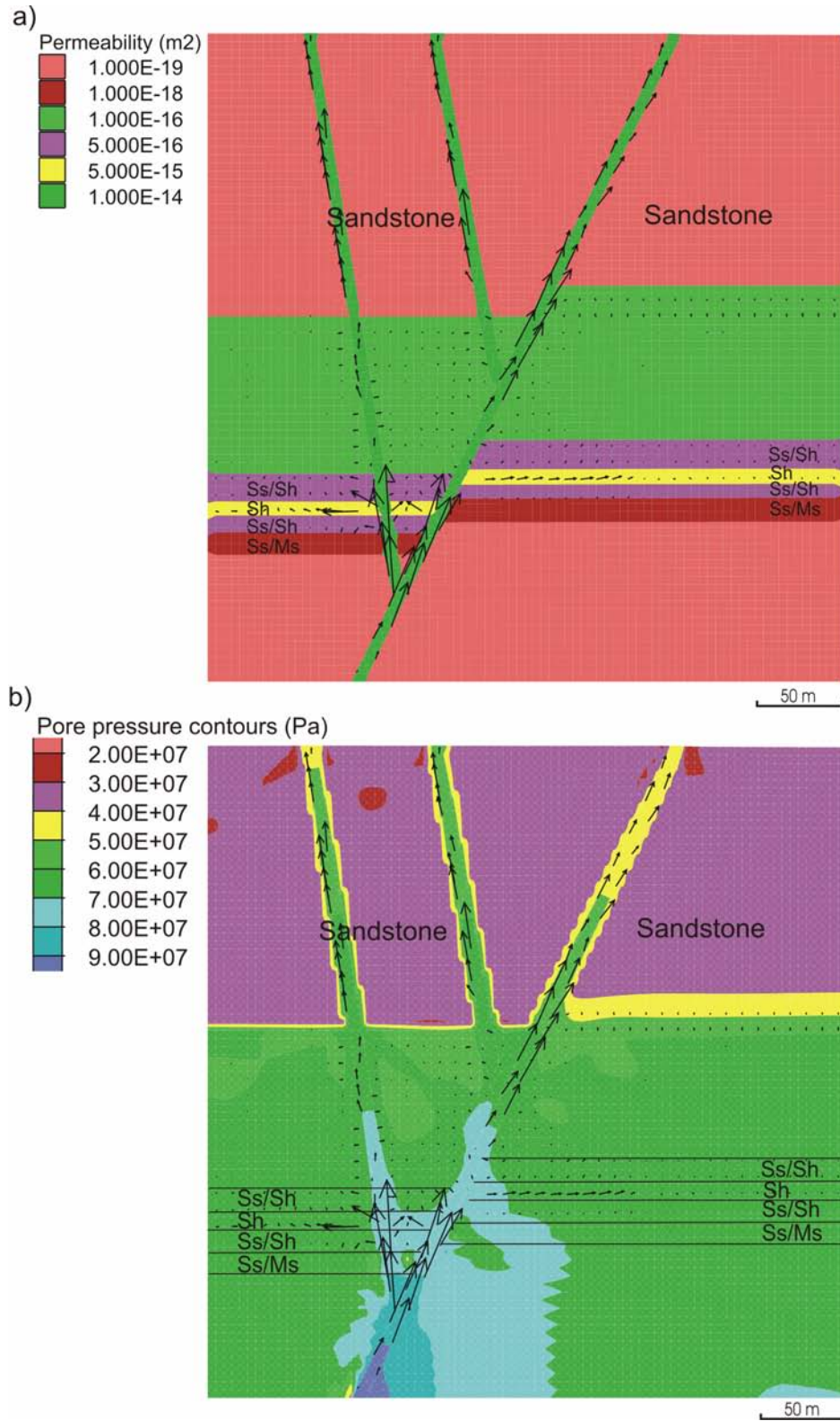


**Figure 4.25.** Model 2c at 1% deformation **a)** displaying permeability values and a strong Darcy fluid flow focussing within the fault zones. Lateral flow is evident within the shale layers, and **b)** plot of pore pressure contours and Darcy fluid flow vectors, displaying strong flow within the faults and minor lateral flow in the shale layers.

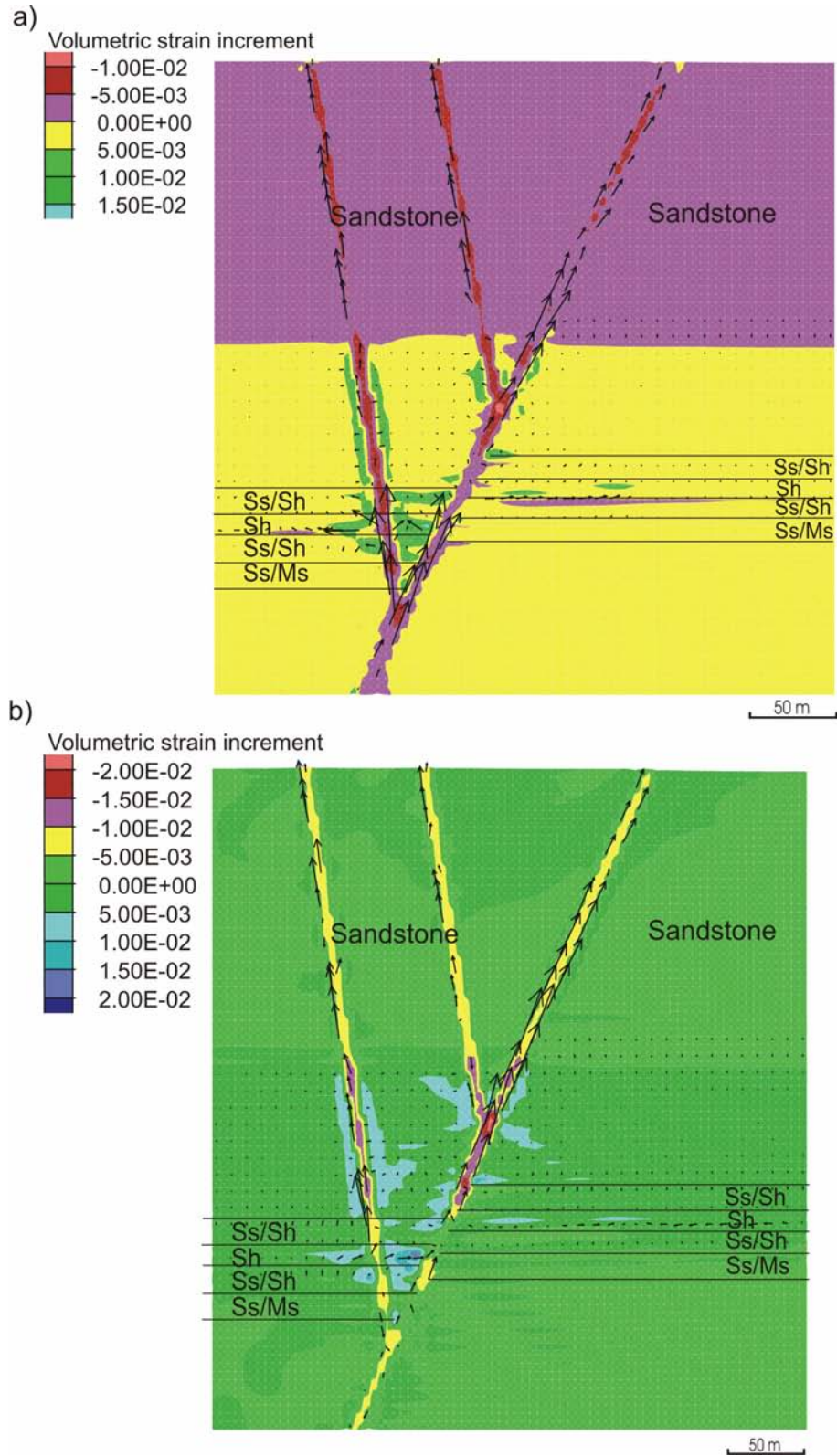


**Figure 4.26.** Model 2c at **a)** 1% deformation, displaying volumetric strain (dilation) and a strong Darcy fluid flow focussing within the fault zones and towards dilatant areas in particular near fault intersections **b)** 5% deformation, plot of volumetric strain (dilation) and Darcy fluid flow vectors, displaying strong flow within the faults and lateral flow into the shale layers.

an equilibrium state following the release of the overpressure, and it is primarily driven by deformation and dilatancy. According to this model, if ore grades were related primarily to large fluid fluxes, shale units between the feeder faults would show high grades.

#### 4.8.6 Model 2d (contraction, high permeability shale, low permeability sandstone, with overpressure and yield permeability)

In an attempt to simulate hydrofracturing and resultant permeability increase in the shale units, an additional function was applied to this model which increased the permeability as a function of the plastic state of the material (i.e. as material reaches a yield state, shear or tensile failure, the permeability of the material at that point is increased by 10% from its original value, and returning or retaining its original value when not at yield). This function was to simulate the process of failure and increased permeability due to hydrofracturing, as proposed by Broadbent (1999). In early stages of compression (3% shortening) fluid flow is mainly driven upwards from the base of the more permeable fault structures, however downward migration of fluids is noted around the mid region of the model and within the faults (Fig. 4.27a), and this appears to be primarily driven by a localised decrease in pore pressure and dilatant effects (Fig. 4.27b). Fluid flow is focussed towards areas of dilation in the shale unit near the intersection of the main fault and the left branching fault, and these areas correspond to an increase in permeability due to failure (Fig. 4.28a). These areas display tensile failure, and due to the increase in permeability have focused much of the fluid flow within the model. As deformation progresses (5% shortening) fluid flow intensifies in this region as a result of pore pressure

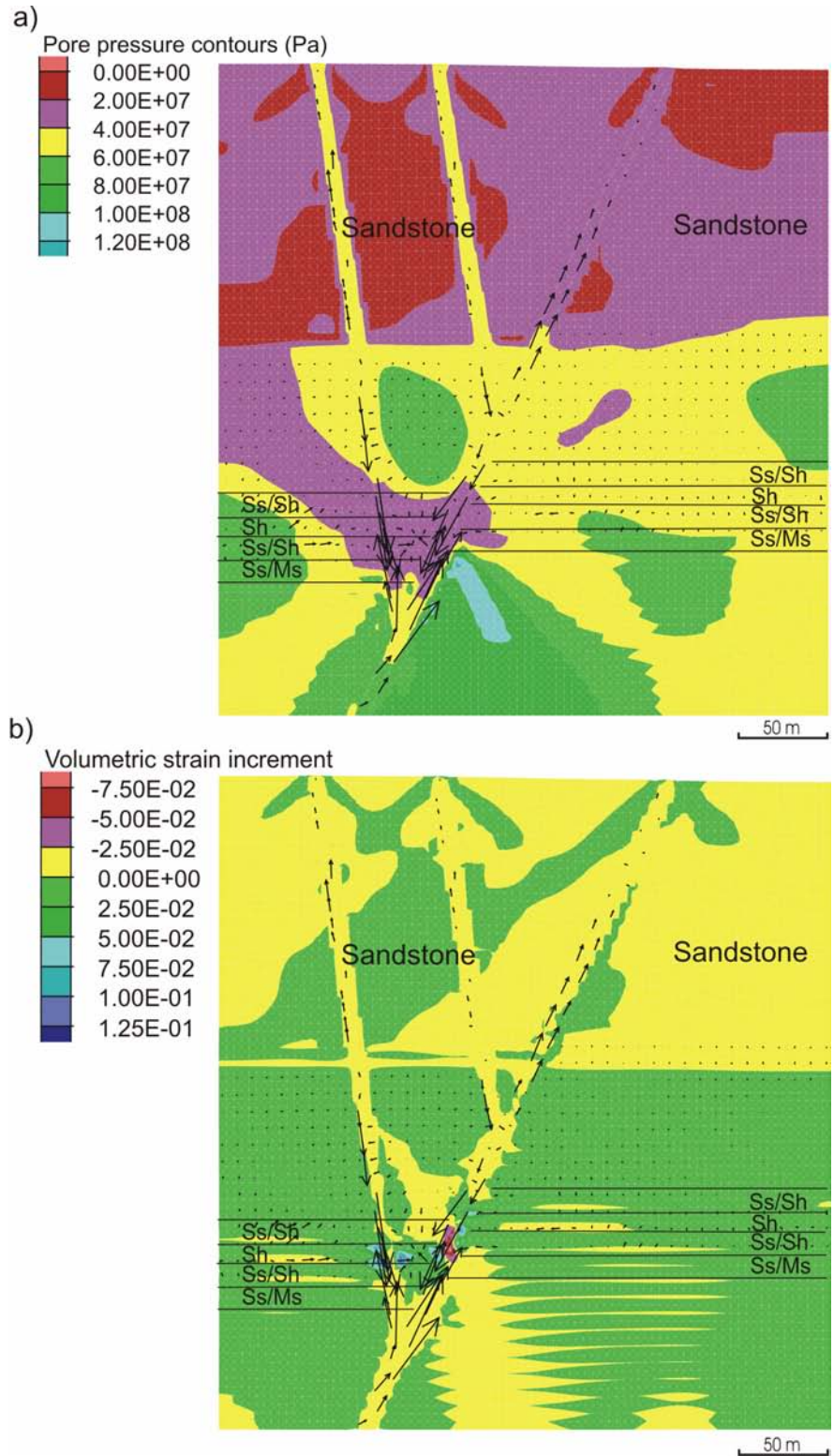


**Figure 4.27.** Model 2d at 3% deformation **a)** displaying pore pressure contours and a strong Darcy fluid flow focussing within the fault zones and towards localised areas of pore pressure decrease **b)** plot of volumetric strain (dilation) and Darcy fluid flow vectors, displaying strong flow within the faults and focussing towards dilatant areas near fault and stratigraphic intersections of the ore zone.

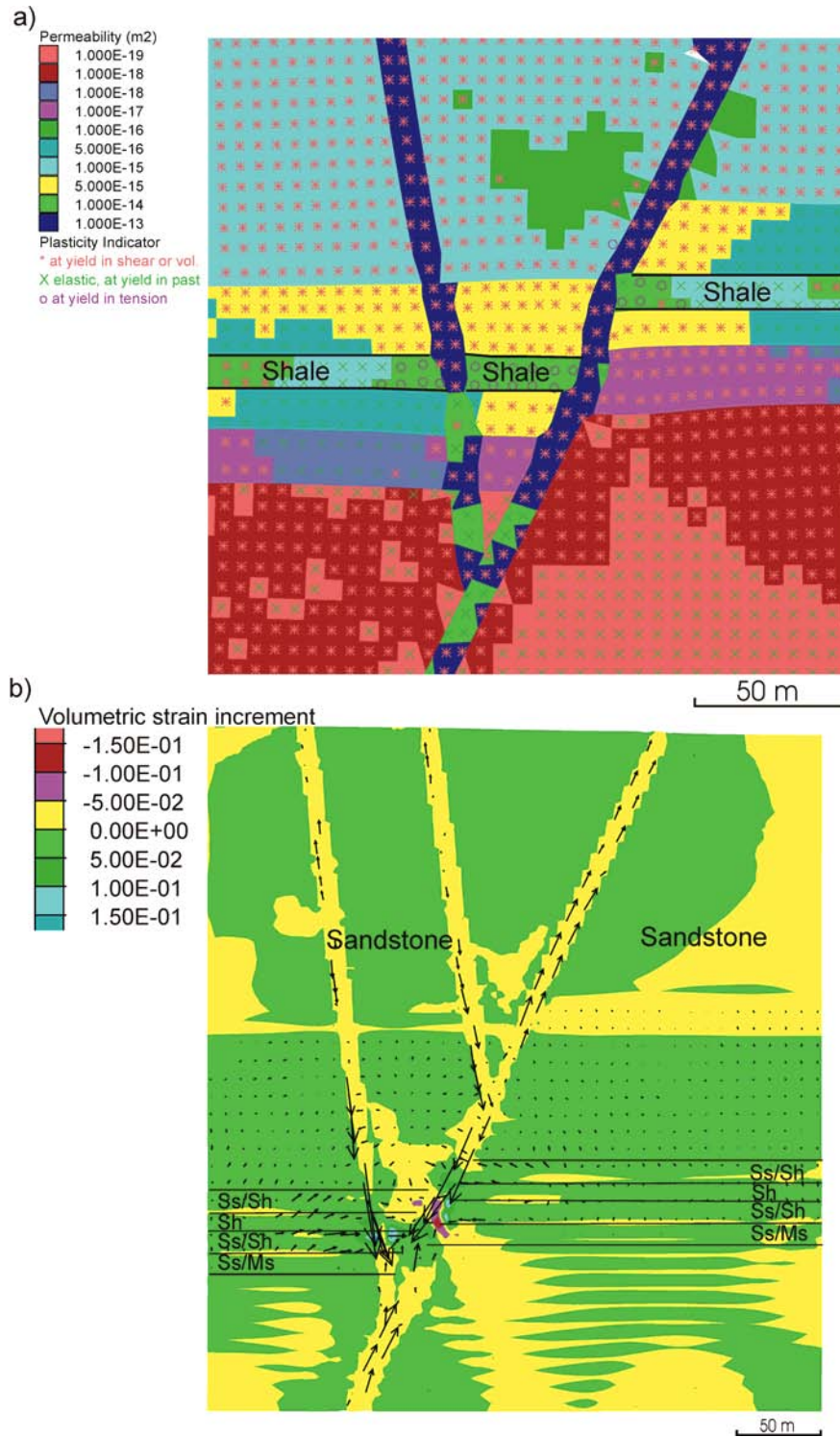


**Figure 4.28.** Model 2d at **a)** 3% deformation, displaying permeability values and yield status or plasticity indicators. As a result of the applied yield function tensile failure is predominantly found in the shale layers (indicated by purple circles) and displaying high permeability values **b)** 5% deformation, plot of volumetric strain (dilation) and Darcy fluid flow vectors, displaying strong flow within the faults and focussing towards dilatant areas near fault and stratigraphic intersections of the ore zone, with strong fluid flow towards the fault notable within the shale layers.

decreases and dilatant effects (Fig. 4.28b). Fluid flow within the shale layer is limited outside this region, and as a result of the yield function applied, the permeability of the shale unit remains one order of magnitude less than that of the fault, hence, fluid remains focussed mainly within the fault zones. At later stages of contraction (7% shortening) similar results are apparent, with further dilatant effects driving fluid towards areas of failure and some localised contraction due to increasing shear strain (Fig. 4.29). Similar to Model 2c, the results of this model permit interpretations of focussed mineralisation in the shale units close to the faults.

In summary, results from Model 2 indicate that overpressure aids in upward migration of fluids within the more permeable faults, and potentially stimulates hydrofracturing within the shale units. To have any significant fluid flow within the shales, they must have permeabilities close to or the same as the faults. Addition of a 'yield function' to increase permeability within the model allows tensile failure and increased permeability within the shale unit, however, fluid is primarily drawn from the shale units towards the faults in most cases. This scenario also limits upward migrating fluids from deeper basinal horizons or basement material from entering the shale units, so ore genesis models using this scenario would have to source metals and sulphur from above. However, local areas between branching faults that display strong dilational characteristics may provide limited access to shales for deep seated mineralising fluids.

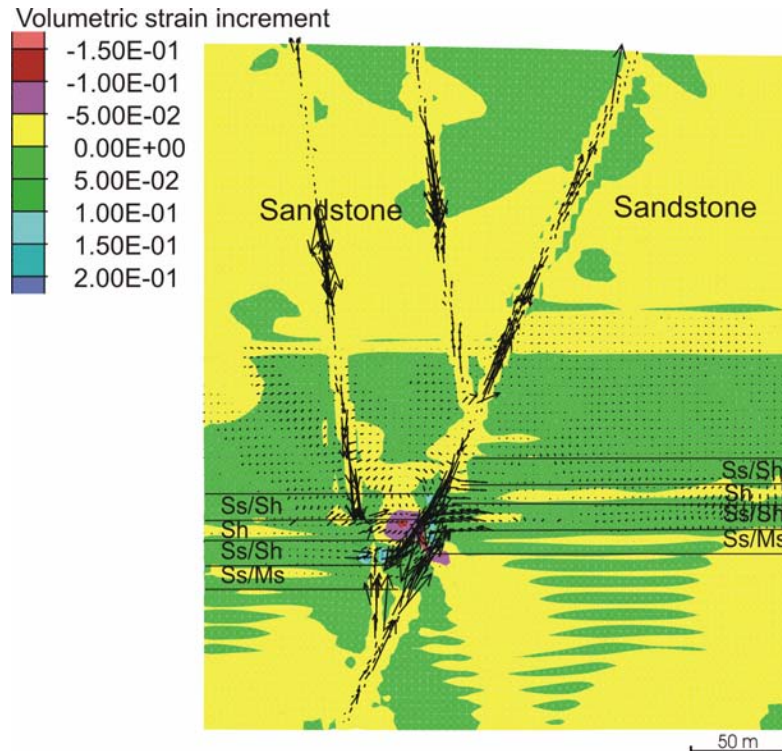


**Figure 4.29.** Model 2d at 7% deformation displaying volumetric strain (dilation) and Darcy fluid flow vectors. Strong flow is evident within the faults and focussing towards dilatant areas near fault and stratigraphic intersections of the ore zone.

#### 4.9 Discussion and Conclusions

Interpretation of the 3D structural model for Century suggests that there is a link between the regional and local scale NE trending structures, which relates to mineralisation. In particular, the regional faults contain vein type deposits (e.g. Silver King deposit) that preserve syn-tectonic breccia hosted mineralisation. Hence, proving that some of these structures intersect the Century deposit supports models for syn-tectonic mineralisation or models of remobilisation of earlier ores during the Isan Orogeny. However, these faults also show relationships to both sedimentary thickness variations and ore grades in Century, raising the possibility that they were active early and contributed to syn-sedimentary mineralisation. Interpretation of the TRF as a conduit for

mineralisation (Broadbent, *et al.*, 1998), was largely based on grade distribution data. We cannot discount the contribution of TRF fault to the ore system; however, this structure may have been more significant after basin inversion at Century, and as a consequence the general trends of Pb and Zn might be the final product of a more complex hydrothermal history in which the reactivation of faults within the deposit may have changed the original configuration of metal distributions. Zn grades and also thickness variation within Unit 200 have not been influenced by NW faults. Thus, NW faults branching from the TRF may have played only a minor role in ore genetic processes and more likely, if they contributed to the metal budget, they did so during later stages of Isan deformation as Broadbent (1999) suggests. This would explain why within Unit 200 the Zn grades do not seem to be influenced by these potentially later structures. Pb grades seem to be correlated with NE structures, but overall the distribution is pointing to at least some influence of later NW structures. The consequence of these findings enhances our understanding of possible genetic relationships of the Century deposit and the Lawn Hill mineral field. We favour a model that envisages the emplacement of Zn and Pb early (syngenetic) as NE structures have been demonstrated to control thickness variation and grade distributions across the deposit, in agreement with the structural interpretation and available seismic profiles drawn in the northern part of the Lawn Hill Platform, which demonstrates that NE growth faults are regionally distributed. A model that additional syntectonic Pb or/and remobilisation of early Zn-Pb is also feasible. Late diagenetic to syntectonic emplacement models do not represent a single solution that fully explains our interpretation the results of the 3D model.

To test our remaining uncertainties, numerical simulations of the subsurface models (diagenetic, syntectonic) were undertaken. In normal circumstances sedimentary sequences have a reasonably well-defined variation in permeability, and shale is considered one of the least permeable units (e.g. Dullien, 1979). Our model results indicate that for fluid to permeate into shale sequences we require permeability values of the shale unit to be close to that of in-situ faults and much greater than surrounding sedimentary packages. Therefore, permeability is the primary factor controlling fluid flow and potential sites of ore deposition. The main observation from the extension models is that during extension, fluid from the surrounding sediments and the fault display extensive lateral migration into the shale units if the shale units are assigned high permeabilities. It is thus possible that migration of fluids along subsurface shale units is mechanically feasible during extensional deformation and may provide the fluid pathways for stratiform diagenetic mineralisation.

Results from the models using fully compacted sediments indicate that overpressure is an additional process that aids in upward migration of fluids within the more permeable faults, and acts as a precursor to hydrofracturing within the shale units. However, the permeability of the shale must be at least  $1/10^{\text{th}}$  that of the faults to provide any significant fluid flow through shale. Addition of a 'yield function' to increase permeability within the model allows tensile failure and increased permeability within the shale unit; however, fluid is primarily drawn from the shale units towards the fault in most cases. Overpressurisation may provide a process that induces hydrofracturing within the shale units; hence increasing permeability. This deformation induced

permeability has the potential to focus fluids into these units; however, as shown by the modelling results these areas would be preferentially located close to the faults, therefore limiting any significant lateral fluid flow. Most of the fluids will then be preferentially driven in and through the fault domain. Thus, even with shale permeability set at unrealistically high values, this scenario works best for mineralisation proximal to faults, and might not be so useful to explain the lateral extent of primary Century mineralisation.

Revisiting the four modelling questions posed earlier, the pathways that controlled the location of favourable sites for mineralisation appear to be two-fold. In an extensional regime, normal reactivation of faults may provide localisation of fluids that have the potential to migrate laterally along more permeable sedimentary units, and during a compressional regime faults appear to be the main fluid conduits, with less lateral migration of mineralising brines. It appears that both tectonic regimes are suitable for forms of mineralisation styles, however lateral flow is primarily favoured by extension. During compression, overpressurisation appears to have a strong influence over upward fluid flow and particularly tensile failure within the shale units, although this is spatially associated with faults, hence limiting lateral flow.

To conclude, it is apparent that we require either extremely permeable shale units in comparison to sandstones during early sedimentation, to contribute towards a subsurface replacive origin for mineralisation. More likely is the potential for significant failure within the shale units as a driving force for dilation and fluid flow focussing, as secondary porosity has less of an influence on

transferring fluids laterally within the mineralised units of the Century deposit. We therefore conclude that a subsurface replacive origin for all the mineralisation is less likely than a syngenetic model with subsequent syntectonic remobilisation.